T.R.
GEBZE TECHNICAL UNIVERSITY
GRADUATE SCHOOL OF NATURAL AND APPLIED SCIENCES

ACTIVE VIBRATION CONTROL OF A BLADE CONTAINING MAGNETORHEOLOGICAL FLUID

FEVZİ ÇAKMAK BOLAT
A THESIS SUBMITTED FOR THE DEGREE OF
DOCTOR OF PHILOSOPHY
DEPARTMENT OF MECHANICAL ENGINEERING

GEBZE
2018

T.R.

GEBZE TECHNICAL UNIVERSITY

GRADUATE SCHOOL OF NATURAL AND APPLIED SCIENCES

ACTIVE VIBRATION CONTROL OF A BLADE CONTAINING MAGNETORHEOLOGICAL FLUID

FEVZİ ÇAKMAK BOLAT

A THESIS SUBMITTED FOR THE DEGREE OF DOCTOR OF PHILOSOPHY

DEPARTMENT OF MECHANICAL ENGINEERING

THESIS SUPERVISOR

PROF. DR. SELİM SİVRİOĞLU

GEBZE

2018

T.C.
GEBZE TEKNİK ÜNİVERSİTESİ
FEN BİLİMLERİ ENSTİTÜSÜ

MANYETORELOJİK SIVI IÇEREN BİR KANAT ELEMANININ AKTİF TİTREŞİM KONTROLÜ

FEVZİ ÇAKMAK BOLAT
DOKTORA TEZİ
MAKİNE MÜHENDİSLİĞİ ANABİLİM DALI

DANIŞMANI
PROF. DR. SELİM SİVRİOĞLU

GEBZE
2018

GEBZE TEKNİK ÜNİVERSİTESİ	**DOKTORA JÜRİ ONAY FORMU**

GTÜ Fen Enstitüsü Yönetim Kurulu'nun 21/11/2018 tarih ve 2018/57 sayılı kararıyla oluşturulan jüri tarafından 13/12/2018 tarihinde tez savunma sınavı yapılan Fevzi Çakmak BOLAT'ın tez çalışması Makine Mühendisliği Anabilim Dalında DOKTORA tezi olarak kabul edilmiştir.

JÜRİ

ÜYE (TEZ DANIŞMANI)	: Prof. Dr. Selim SİVRİOĞLU	
ÜYE	: Prof. Dr. Ercan ERTÜRK	
ÜYE	: Prof. Dr. Hasan KURTARAN	
ÜYE	: Prof. Dr. Erkan ZERGEROĞLU	
ÜYE	: Doç. Dr. Ahmet Sinan ÖKTEM	

ONAY

Gebze Teknik Üniversitesi Fen Enstitüsü Yönetim Kurulu'nun

.../.../... tarih ve ..../..... sayılı kararı.

SUMMARY

In this thesis, a magnetorheological fluid-based control method has been proposed to suppress the vibrations of a small-scale wind turbine blade element. In this scope, two cases are respectively investigated. In the first case, the magnetorheological fluid is filled into the blade element and in the second case, this fluid is adhered as a patch layer on the blade element. In both cases, an electromagnet actuator is used to generate force by using the magnetic property of the magnetorheological fluid. Considering both the filled blade element and the laminated patch, a model that describes the force relationship between the electromagnet and the magnetorheological fluid is obtained. Force characterization studies have been carried out to reveal the response of the magnetorheological fluid to the pulling force generated by the electromagnet.

The equation of motion of the blade element containing magnetorheological fluid is obtained by two different methods and its natural frequencies are compared with the experimental results. The effect of magnetorheological fluid on natural frequencies is investigated. State space equations are obtained based on both equations of motion. Norm based multi-objective H_2 / H_∞ controller design has been realized for active vibration control of the blade element.

In order to perform the active vibration control experimentally, experimental systems have been constituted for two different cases that the magnetorheological fluid has been filled into the blade element and has been adhered as a layer on the blade element. To create a continuous vibration on the blade element, an aerodynamic load is created experimentally and the controllers designed for different conditions under this load are tested. Experimental results were evaluated over frequency and time responses. The results obtained in the case of the magnetorheological patch are compared with the results of active vibration control using a piezoelectric (PZT) patch of almost the same size.

Key Words: Wind Turbine Blade, Magnetorheological Fluids, Piezoelectric Materials, Robust Control, Active Vibration Control.

ÖZET

Bu tez çalışmasında küçük ölçekli bir rüzgâr türbini kanat elemanının titreşimlerini bastırmak için manyetoreolojik sıvı esaslı bir kontrol yöntemi önerilmiştir. Bu kapsamda manyetoreolojik sıvının kanat elemanı içerisine tamamen doldurulması ve kanat elamanı üzerine bir tabaka halinde yama olarak yapıştırılması gibi iki durum ele alınmıştır. Her iki durumda da manyetoreolojik sıvının manyetik özelliğini kullanarak kuvvet oluşturmak için bir elektromıknatıs eyleyici kullanılmıştır. Gerek tam dolu kanat elemanı gerekse tabaka halindeki yama için elektromıknatıs ile manyetoreolojik sıvı arasında kuvvet ilişkisini veren bir model elde edilmiştir. Manyetoreolojik sıvının elektromıknatısın oluşturduğu çekme kuvvetine olan cevabını ortaya koymak için kuvvet karakterizasyonu çalışmaları gerçekleştirilmiştir.

Manyetoreolojik sıvı içeren kanat elemanının hareket denklemi iki farklı yöntemle elde edilerek doğal frekansları bulunmuş deneysel olarak elde edilen sonuçlarla karşılaştırılmıştır. Doğal frekanslar üzerinde manyetoreolojik sıvının etkisi incelenmiştir. Durum uzayı denklemleri her iki hareket denklemi esas alınarak elde edilmiştir. Kanat elemanının aktif titreşim kontrolü için norm esaslı çok amaçlı H_2 / H_∞ kontrolcü tasarımı gerçekleştirilmiştir.

Aktif titreşim kontrolünü deneysel olarak gerçekleştirmek amacıyla manyetoreolojik sıvının kanat elemanı içerisine tamamen doldurulduğu ve kanat elamanı üzerine bir tabaka halinde yama olarak yapıştırıldığı iki farklı durum için deneysel sistemler oluşturulmuştur. Kanat elemanı üzerinde sürekli bir titreşim oluşturmak için deneysel olarak bir aerodinamik yük oluşturulmuş, bu yük altında farklı durumlar için tasarlanan kontrolcüler test edilmiştir. Deneysel sonuçlar frekans ve zaman cevapları üzerinden değerlendirilmiştir. Manyetoreolojik yama durumunda elde edilen sonuçlar hemen hemen aynı boyuttaki bir piezoelektrik (PZT) yama kullanılarak yapılan aktif titreşim kontrolü sonuçları ile karşılaştırılmıştır.

Anahtar Kelimeler: Rüzgâr Türbin Kanadı, Manyetoreolojik Sıvılar, Piezoelektrik Malzemeler, Gürbüz Kontrol, Aktif Titreşim Kontrolü.

ACKNOWLEDGEMENTS

I would like to express my deepest and sincere gratitude to my supervisor, Prof. Dr. Selim SIVRIOGLU for shared his profound scientific knowledge with me and personals experiences. It was a pleasure to study with him because he has very hard work job discipline and endless science love. His support, suggestions and encouragement gave me the drive and will to complete this work.

I would like to thank Prof. Dr. Hasan KURTARAN and Prof. Dr. Ercan ERTÜRK due to their guidance and encouragements.

I wish to express my warm and sincere thanks to Asst.Prof. Sinan BAŞARAN for his collaboration and interest. I want to thank Res. Asst. Ali Suat YILDIZ and Res. Asst. Gökçe AKGÜN for their support and interest.

Finally, I would like to thank all of my friends and my family members, especially to my wife and my girl GUNES.

TABLE of CONTENTS

	Page
SUMMARY	v
ÖZET	vi
ACKNOWLEDMENTS	vii
TABLE of CONTENTS	viii
LIST of ABBREVIATIONS and ACRONYMS	x
LIST of FIGURES	xii
LIST of TABLES	xvi
1. INTRODUCTION	1
1.1. Literature Review	2
1.2. Contributions of the Thesis	4
1.3. Scope of the Thesis	5
2. MODELING OF THE BLADE ELEMENT	10
2.1. Equivalent Beam Model	10
2.1.1. State Space Equation	14
2.2. Lumped Parameter Model	16
2.2.1. State-Space Model	23
2.3. Natural Frequency Analysis	24
3. MR FLUID BLADE APPLICATIONS	28
3.1. MR Layer Patch	28
3.1.1. Force Characterization	29
3.2. MR Fluid Filled Blade	33
3.2.1. Force Identification	35
4. MULTI-OBJECTIVE H_2/H_∞ CONTROL	39
4.1. Control Objectives	39
4.2. Control Design Blocks	40
4.3. Control Principle	45
4.4 Controller Design for MR Filled Blade System	47
4.5 Controller Design for MR Patch Blade System	49

5. EXPERIMENTAL STUDY 52
5.1. Aerodynamic Load 52
5.2 Active Vibration Control of the Blade with MR Layer Patch 55
5.2.1 Experimental Results 56
5.3. Active Vibration Control using PZT Patch Actuator 60
5.3.1 PZT Force Model 60
5.3.2 State Space Model 62
5.3.3 Controller Design 64
5.3.4 Experimental System 64
5.4 Power Consumption Analysis 68
5.5 Active Vibration Control of the Blade Containing MR Fluid 71
5.5.1 Experimental Results 72
5.6 Switch Control 75
5.6.1 Single-sided Actuation Principle 76
5.6.2 Positive Current Algorithm 76
5.6.3. LQG Control Design 77
5.6.4 State feedback based positive current algorithm 78
5.6.5 Experimental study 81
5.6.6. Results and discussion 82
6. CONCLUSIONS 89

REFERENCES 91
BIOGRAPHY 95
APPENDICES 96

LIST of ABBREVIATIONS and ACRONYMS

Abbreviations and Acronyms		**Explanations**
E_p	:	Young's modulus of the PZT patch
E_f	:	Young's modulus of the blade
I_f		Inertia of the blade
L	:	Length of the blade
ρ	:	Density of the blade
ρ_{air}		Density of the air
L_p	:	Length of the PZT patch
h_p	:	Thickness of the PZT patch
b_p	:	Width of the PZT patch
b_{mr}	:	Width of the magnetorheological layer
h_{mr}	:	Height of the magnetorheological layer
d_{31}	:	Piezoelectric charge constant
C_L	:	Lift coefficient
C_D	:	Drag coefficient
α		Angle of attack
N	:	Number of the coil turn
i_c	:	Control current
μ_0	:	Vacuum permeability
B	:	Magnetic field
G^*	:	Complex shear modulus
S_k	:	Skin thickness of the blade profile
K_δ	:	Bending stiffness
C	:	Width of the Chord
T_b	:	Height thickness of the blade

Ω	:	Blade inertia calculation design constant
f_a	:	Aerodynamic force
f_d	:	Disturbance force
f_e	:	Electromagnet force
f_m	:	Magnetic nonlinear force
i_0	:	Bias current
b_{eb}	:	Width of the equivalent beam
w_p	:	Flexibility of the MR patch

LIST of FIGURES

Figure No:		Page
1.1:	Photos of elastic blade structure, a) front view, b) longitudinal view.	6
1.2:	A damaged wind blade due to vibration.	7
1.3:	MR-Patch actuator.	7
1.4:	Magnetorheological fluid working principle.	8
1.5:	Basic operational modes for controllable MR fluid devices.	9
2.1:	Dimensions of the blade profile, a) cross section, b) the equivalent beam model.	14
2.2:	Frequency response of the blade state space models.	16
2.3:	Lumped parameter model, a) coordinates, b) cross-section.	18
2.4:	Frequency response of the blade model.	24
2.5:	Experimental setup.	25
2.6:	Experimental frequency responses of the hollow and MR fluid filled blade (0 G).	26
2.7:	Mode shape and natural frequency of the blade using FEM**.**	27
3.1:	Structure of the MR fluid patch.	28
3.2:	The MR patch attached on the blade.	29
3.3:	The electromagnet positioned over the MR patch.	29
3.4:	Interaction model between the electromagnet and the MR patch a) initial state, b) expansion of the MR patch, c) control of the blade.	31
3.5:	Variation of the experimental electromagnetic force and the response force of the MR patch.	32
3.6:	Variation the response force, a) with current, b) with displacement.	33
3.7:	Blade profile, a) filled with MR fluid, b) hollow blade.	34
3.8:	Experimental results at constant magnetic field (a) blade vibrations (b) electromagnet currents.	35
3.9:	Illustration of the MR blade and electromagnetic actuator interaction, a) initial setting, b) the application of the bias current i_0, c) the control force f_a generation.	37

3.10:	Force measurements, a) Experimental setup, b) Variation of the electromagnetic force and the transmitted force.	38
4.1:	Multi-objective control structure	40
4.2:	Control design block structure for Design-1.	43
4.3:	Control design block structure of Design-2	44
4.4:	Control design block structure of Design-3	45
4.5:	Control principle of the blade vibrations.	45
4.6:	Frequency responses of the multi-objective controllers	47
4.7:	Frequency responses of the closed loop systems.	47
4.8:	Frequency responses of the weighting filters and uncertainty.	48
4.9:	Frequency responses, a) the multi-objective controller, b) the closed-loop system.	49
4.10:	Frequency responses of the weighting filters and uncertainty.	50
4.11:	Frequency responses, a) the multi-objective controller , b) the closed-loop system.	51
5.1:	Application of aerodynamic load cross-section of the airfoil.	53
5.2:	Aerodynamic load characteristics, a) Lift and drag coefficients, b) Variation of the drag force with air velocity.	53
5.3:	Air nozzle effecting aerodynamic load on the blade element.	54
5.4:	Steady state response in aerodynamic load, a) angle of attack 17.2 degree, b) angle of attack 19 degree.	54
5.5:	Experimental system setup.	55
5.6:	Feedback control structure.	56
5.7:	Experimental frequency responses of the closed loop system, a) full system, b) first two modes	57
5.8:	Experimental results of the closed loop system with steady state aerodynamic load, a) continuous control, b) vibration of the blade element in small scale time range.	58
5.9:	Experimental results of the closed loop system for repeated control with steady state aerodynamic load.	59
5.10:	Experimental control inputs, a) continuous control, b) repeated control.	59
5.11:	Robustness test results for additional mass.	60

5.12:	PZT patch actuator	60
5.13:	PZT patch layout and parameters.	61
5.14:	Layout of the cantilever blade	63
5.15:	Experimental system setup blade with PZT patch.	65
5.16:	Experimental frequency responses of the closed loop system, a) full system, b) first two modes	66
5.17:	Experimental results of the closed loop system with steady state aerodynamic load.	67
5.18:	Experimental results of the repeated controlled and uncontrolled blade vibrations	67
5.19:	Experimental control inputs	68
5.20:	Robustness test results for additional mass	68
5.21:	MR patch structure instantaneous power consumption.	70
5.22:	PZT patch instantaneous power consumption.	70
5.23:	Total power consumption for two structures.	70
5.24:	Experimental system.	71
5.25:	Experimental frequency responses of the closed loop, a) all modes, b) first two modes.	72
5.26:	Experimental results of the closed loop system under steady state aerodynamic load.	73
5.27:	Experimental control inputs, a) continuous control, b) repeated control.	74
5.28:	Robustness test results for an additional mass, a) Steady state case, b) Reference point case.	75
5.29:	The principle of electromagnetic actuation, a) front view, b) longitudinal view.	76
5.30:	State feedback control structure with positive current algorithm.	81
5.31:	Experimental Simulink block.	81
5.32:	Frequency responses of the control system, a) all vibration modes, b) first two modes.	82
5.33:	Experimental time history responses under the steady state aerodynamic disturbance for 10 m/s air speed, a) continuous controlled, b) repeated controlled.	84

5.34: Experimental control inputs for 10 m/s, a) continuous controlled, b) repeated controlled. 85
5.35: Variation in detailed time responses, a) the blade displacement, b) the control input. 86
5.36: Experimental time history responses under the steady state aerodynamic disturbance for 15 m/s, a) continuous controlled, b) repeated controlled. 87
5.37: Experimental control inputs for 15 m/s, a) continuous control, b) repeated control 88
5.38: Worst-case test results for a tip mass. 88

LIST of TABLES

Table No:		**Page**
2.1:	Natural frequencies of the blade vibration modes.	27
3.1:	The measured forces in different currents.	32
5.1:	Amount of reduction in gains with multi-objective controller.	57
5.2:	Parameters of the cantilever blade and PZT patch.	64
5.3:	Amount of reduction in gains with multi-objective controller.	67
5.4:	Compare of total energy consumption.	71
5.5:	Amount of reduction in gains with H_2 / H_∞ controller.	73

1. INTRODUCTION

Engineering flexible structures like beams, plates and shells show modal dynamic behavior when subjected to external disturbances. It is a desired characteristic for such engineering structures to have adaptive behavior according to varying external conditions. The stiffness and damping values of the adaptive structures can be changed by integrating smart materials into these structures. The dynamics of such structures can also be controlled by adjusting the parameters arised from external conditions with active or semi-active systems.

One of the key points in gaining adaptiveness of the structures is the integration of intelligent or smart materials. Smart materials can either restrict the movement of the structure or directly make the desired movement by acting on the structure. Piezoelectric (lead zirconate titanate (PZT)) materials are in the class of these materials and have been studied by many researchers to design smart or adaptive systems. Structures having PZT layer actuators have great potentials especially for aerospace applications. However, there are some difficulties in realization for large engineering systems due to limited outputs of PZTs. Also driving voltages of PZT become very high and costly for large and heavy systems. Moreover, PZT actuators may not be used in semi-active control applications.

Due to the disadvantages of PZT materials, some other intelligent materials are being developed. One of the such materials is magnetorheological (MR) fluid. Magnetorheological (MR) fluids are intelligent materials because of their interchangeable mechanical properties under a magnetic field. Therefore, magnetorheological materials have been attracted much attention for use in engineering systems. The magnetorheological fluids are essentially non-Newtonian fluids consisting of ferromagnetic particles that its rheological properties can be changed under applied external magnetic field. MR fluids have potential to be used in engineering systems such as automotive, aerospace and civil structures. They can be effectively placed as a layer in structural systems. Vibrations of adaptive sandwich structures can be decreased by an applied magnetic field to the MR layer.

In general, control methods also play a role to shape the dynamics of the adaptive structures. Active vibration control approaches improve the performance in

terms of reduction in vibration amplitude of the structures compared with passive systems.

1.1. Literature Review

In recent years, researches on the structures containing MR fluid have been increasing in many areas such as engineering applications in automobile suspension, medical devices and structural systems. In structural systems, MR fluid layer can be embedded in a flexible structure and a vibration control can be performed by using a varying magnetic field. Various researches have been attempted to understand the dynamic behavior of structures containing MR fluid under magnetic field. In this thesis, reviewed MR related studies in the literature are limited to structural system applications of vibration control. In addition, the review mainly focused on modeling, dynamic analysis and active control studies of structural systems.

Some of the most important studies related with adaptive structure applications have been conducted by Yalcintas et al. They studied the dynamics of an electrorheological (ER) material that is implemented in non-homogeneous adaptive beams. In their study, analytical models were obtained for various configurations of sandwich structures. The natural frequencies, mode shapes and damping behaviors were experimentally investigated by applying different magnetic fields on the designed structures. The complex shear modulus of the ER material changes with the applied electric field level, therefore the effect of this change was experimentally investigated for different composite beam configurations [Yalcintas et al., 1997].

Yalcintas and Dai studied on two different sandwich structures that were produced using both electrorheological and magnetorheological fluids as layers inside solid metal or composite layers. Vibration suppression behavior was investigated by applying different magnetic fields on both sandwich structures. It was shown that the dynamics of adaptive sandwich structure might vary when different magnetic fields were applied on the structures. Using such adaptive behavior, it is possible to design structures with variable stiffness, damping properties and Young modulus [Yalcintas and Dai, 1999].

Yalcintas and Dai focused on the vibration response of adaptive sandwich structures containing magnetorheological fluid. The sandwich structures were produced by filling the magnetorheological fluid as a layer between two

homogeneous elastic layers. An analytical model was obtained by using the energy method. Also, different magnetic fields were experimentally applied on the sandwich structure and dynamic behaviors were examined. Natural frequency, loss factor value and vibration damping changes were investigated both experimentally and analytically [Yalcintas and Dai, 2003].

Sun et al. examined the relationship between the magnetic field and the complex shear modulus of MR materials in the pre-yield regime. Moreover, vibration characteristics of MR adaptive structures were predicted for different magnetic field levels. The natural frequency equation was obtained for an adaptive beam using the Hamilton principle. In the results of the study, it was observed that the natural frequencies were shifted as the magnetic field increased [Sun et al., 2003].

In this study, Yeh investigated the vibration analysis of a rectangular plate with a core material of MR elastomer. The effects of magnetic field level on natural frequency and loss factor were investigated. Within the scope of the study, a theoretical model has been developed and the accuracy of the model results has been analyzed by comparing it with the previously studied articles [Yeh, 2013].

A magnetorheological fluid-based sandwich plate was fabricated utilizing two different magneto-rheological fluids (MRF-132DG and MRF-122EG) as the core layer and silicon rubber spacer as the sealant. By using plate theory, the equations of motion of this sandwich plate were obtained and experimental results were compared with the theoretical results and results were consistent. The dynamic reaction of the sandwich structure produced with 132DG material under the magnetic field was observed to be greater than the sandwich structure produced with 122EG material [Eshaghi et al., 2015].

Ghorbanpour et al. surveyed a vibration analysis of a sandwich beam which is containing magnetorheological elastomer core and carbon nanotubes composite face sheets. Halpin-Tsai method was used to determine the matrix phase properties of this structure. Equations of motion were extracted with Hamilton approach. As a result, the natural frequency and the stiffness coefficient of the structure have increased as the magnetic field was increased [Ghorbanpour et al., 2017].

Rajamohan et al. produced a sandwich beam containing a magnetorheological fluid layer and examined the variation of the parameters such as natural frequency, rigidity change and loss factor under the magnetic field. The equations of motion of the proposed sandwich structure with the finite element method were derived and the

accuracy of this model was compared with experimental results. Rajamohan also examined the beam dynamic behavior by filling the magnetic fluid into partially areas within the beam [Rajamohan et al., 2009, 2010, 2013].

In this paper, Manoharan et al. analyzed the vibration responses of the plates with magnetorheological fluid. Effects of different boundary conditions and magnetic field on dynamic response were investigated. Results obtained using finite element method were compared with experimental results [Manoharan et al., 2016].

Rajamohan et al. designed state feedback LQR control and was studied for an adaptive sandwich beam containing magnetorheological fluid as a core layer. The mass and stiffness matrices were obtained by using finite element method. With the designed LQR control, a remarkable damping ratio was obtained in the vibration of the sandwich structure [Rajamohan et al., 2011].

Another research group proposed an analytical model solution for the MR sandwich structure using Hamilton's principle and Kelvin-Voigt model in the pre-yield regime. They designed a controller based on the Lyapunov stability theory. Moreover, the control effect of magnetorheological fluid was demonstrated by simulation studies [Chen and Hansen, 2005].

A simple semi-active vibration control algorithm for free vibrations of a sandwich MR fluid beam based on switching the system equivalent stiffness between two distinct values was proposed in the study of [Romaszko et al., 2015]. Also, [Snamina, 2012] built a vibration control algorithm by applying a non-uniform magnetic field on the beam with magnetorheological fluid. Moreover, [Zhang and Kang, 2015]’s study focuse on the topology optimization of the MR fluid layer in a sandwich plate for improving the semi-active vibration control performance.

1.2. Contributions of the Thesis

This thesis deals with the active vibration control of a flexible blade element using two different magnetorheological fluid applications. In the first control approach, an MR fluid layer patch is prepared and attached on the surface of the blade element. The MR patch-based active control is a new approach and no studies have been reported in the literature. The main contributions of the thesis concerning with MR patch are summarized as:

- A novel magnetorheological fluid patch which is actuated by an electromagnet is designed to suppress vibrations of a small-scale wind turbine blade element.
- An interaction model between the magnetorheological patch and the electromagnetic actuator is derived and a force characterization is realized. The response force characteristics of the MR patch is investigated to understand the effect of patch flexibility.
- The active vibration control of the blade element with MR patch is experimentally examined under the steady-state aerodynamic load conditions. The results of experiments show that the MR layer patch is effective for suppressing vibrations of the blade structure and robust against parametric uncertainty.

In the second active control application, MR fluid is filled completely into the blade element since the inside of the blade is empty and both ends of the blade are closed with leak proof stick after filling. In literature, three-layer beam structures containing MR fluid as the core in between the two elastic layers have been studied as an MR sandwich beam. The proposed MR filled blade structure have differences compared to MR sandwich beams. The blade element containing MR fluid is only affected by the fluid mass inside the structure. MR fluid has no effect on the rigidity of the blade. The stiffness of sandwich beams with MR layer increases by applying a homogeneous magnetic field on the complete structure. However, stiffness of the blade filled with MR fluid is not affected because the magnetic field is not applied on the complete structure. The active control of the flexible blade with an electromagnet uses only magnetic properties of the MR fluid.

1.3. Scope of the Thesis

In structural systems, the placement of the MR fluid is mostly seen as a core layer in composite materials. The actuation of the MR material determines the active or semi-active control structure. In literature, actuation of MR material is separated into two groups:

- First one is to actuate the MR fluid layer inside composite structures under a constant magnetic field using permanent magnets.
- The second is to use a variable magnetic field source. When the magnetic field is not applied on the MR fluid inside the structure, it has no contribution to the stiffness of the structure, it only creates a mass effect. However, when the magnetic field is applied to the MR fluid in an adaptive sandwich structure, it becomes rigid and magnetic field has an influence on the Young modulus, implicitly on the stiffness value of the structure.

In this thesis, the ferromagnetic feature of the MR fluid is employed by an electromagnet actuator to realize an active vibration control. As a control object, an aluminum alloy elastic blade element which is used in a small-scale wind turbine test system is studied for the aims of vibration suppression. The front and longitudinal views of the blade are shown in Figure 1.1(a)-(b), respectively. The blade structure is manufactured with an aluminum extrusion machine. The middle of the airfoil is empty to reduce the weight of the blade. This hollow structure is used to fill the MR fluid. The blade is fixed at its one end with a clamp using a connecting piece fitted with the profile. The length of the blade after clamping is 800 mm and the width of the blade is constant in lengthwise.

a) b)

Figure 1.1: Photos of elastic blade structure a) cross-section view, b) longitudinal view.

- Potential applications

Vibration is one of the most important issues for wind turbine blades in operation. A damaged wind blade due to vibration is shown in Figure 1.2. Many wind turbine blades are damaged every year and additional maintenance and repair costs are inevitable. The active control structure proposed in this thesis can be used to suppress vibration of wind turbine blades.

The application of the proposed MR fluid patch-electromagnetic actuator may be possible for the small- and medium-size wind turbine blades. The electromagnets should move with the blades during wind turbine operation by using slip-rings to conduct power to the electromagnets. Using the displacement information from an optical sensor the electromagnet that fixed on the wind turbine body may reduce the blade vibrations by applying the active force on the MR layer. A detailed conceptual drawing is shown in the Figure 1.3.

Figure 1.2: A damaged wind blade due to vibration.

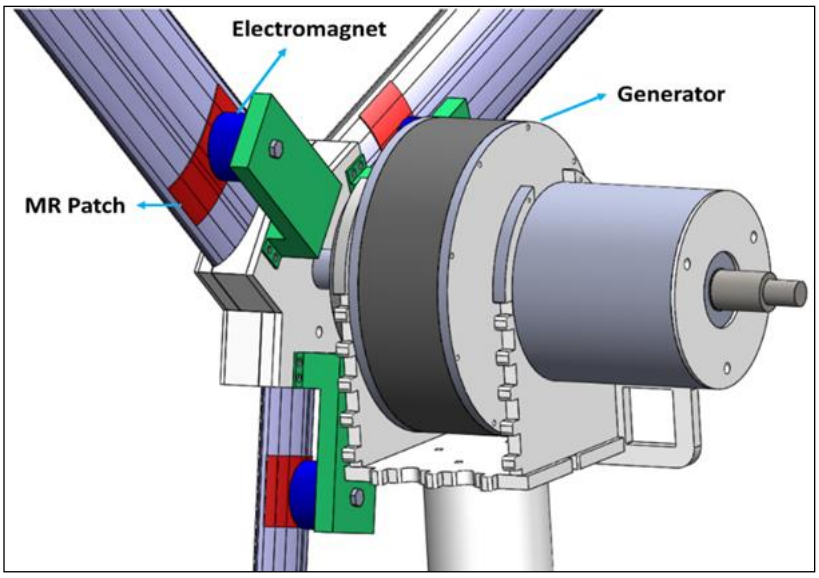

Figure 1.3: MR-Patch actuator.

- Properties of Magnetorheological Fluids

Basically, MR fluid is a low viscosity material obtained by mixing oil and micron sized iron particles. When this fluid is exposed to a magnetic field, the iron particles that are randomly present inside the fluid are ordered very rapidly. Owing to these features, MR fluids have potential to be used in engineering structures due to showing adaptive behavior for changing external conditions. Utilizing a MR fluid layer embedded in a flexible structure, a vibration control system can be built by using a varying magnetic field generated by an electromagnet.

MR fluids can be obtained in different forms depending on the type of oil and ferromagnetic particles. The most widely known and widely used products are the 132DG and 122EG products of LORD company. The iron particles are normally dispersed in the oil as shown in Figure. (1.4a). When the fluid is exposed to a magnetic field, the particles are sequenced as illustrated Figure. (1.4b). The magnetic field may be formed by permanent magnets as shown in Figure. (1.4b) or may be an adjustable magnetic field with coils as in Figure (1.4c). The stationary magnetic field is generally used to examine the dynamic behavior of sandwich structures and determine the natural frequency of the structure. On the other hand, the interchangeable magnetic field is used both in the study of dynamic behavior and in active control applications.

It is classified that MR fluid devices have three working mechanisms or modes. These are flow (valve), shear (clutch) and squeeze (compression) modes as illustrated in Figure 1.5.

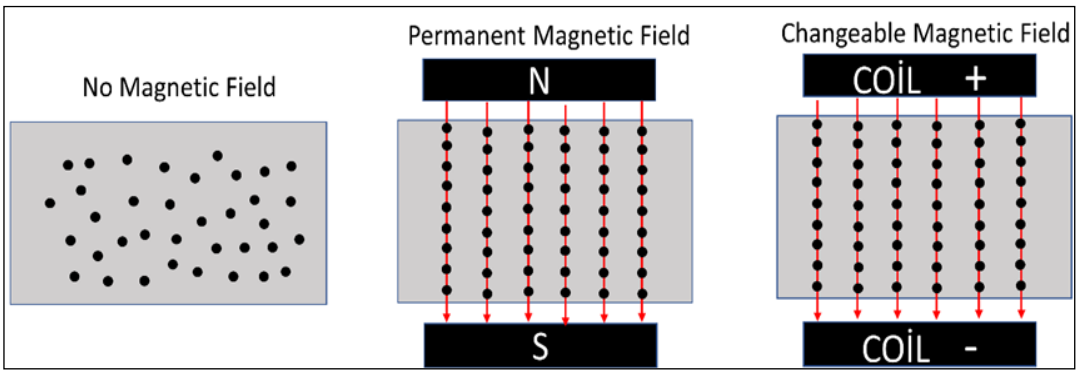

a) b) c)

Figure 1.4: Magnetorheological fluid working principle.

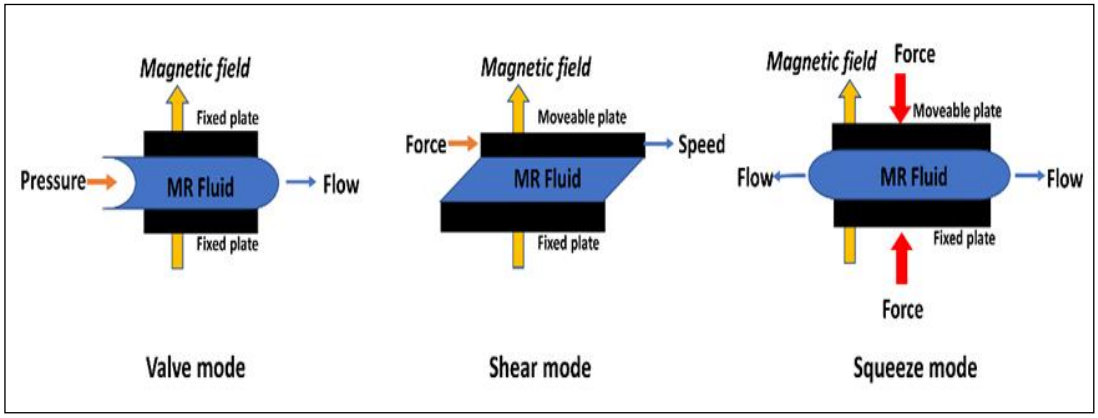

Figure 1.5: Basic operational modes for controllable MR fluid devices.

2. MODELING OF THE BLADE ELEMENT

The determination of the eigenfrequencies and the corresponding eigenfunctions is necessary to analyze vibration problems in a distributed system. A modal analysis is performed for the considered elastic blade element. In this section two different modeling approach is studied to derive the equation of motion of the blade element. State-space equations are obtained using each model to design a controller.

2.1. Equivalent Beam Model

The equivalent beam with MR material considered in this study is schematically illustrated in Figure 2.1b. Hamilton principle can be used to derive the equations of motion of the elastic blade element.

$$\int_{t_1}^{t_2} \left(\delta\mathcal{L} + \delta\mathcal{W}\right) dt = 0 \text{ or } \delta\int_{t_1}^{t_2} \left(\mathcal{L} + \mathcal{W}\right) dt = 0 \tag{2.1}$$

where $\mathcal{L} = T - V$ is the Lagrangian in which T is the kinetic energy due to transverse and rotational motions, V is the corresponding potential energy due to bending and shear stresses of the structure. Also, $\mathcal{W}$ is the work performed by external forces $\mathcal{L}$ and $\mathcal{W}$ are given as

$$\begin{aligned}\mathcal{L} = &\frac{1}{2}\left[\int_0^L \left(\frac{\partial w(x)}{\partial t}\right)^2 \rho(x)\, dx + \int_0^L \left(\frac{\partial \phi(x)}{\partial t}\right)^2 J(x)\, dx\right] \\ &-\frac{1}{2}\left[\frac{1}{2}(h_1+h_2)^2 b h_1 E_f \int_0^L \left(\frac{\partial \phi}{\partial x}\right)^2 dx + 2E_f I_f \int_0^L \left(\frac{\partial^2 w}{\partial x^2}\right)^2 dx + G^* h_2 b \int_0^L \gamma^2 dx\right]\end{aligned} \tag{2.2}$$

$$\mathcal{W} = \int_0^L f(x,t) w(x,t) dx\,, \tag{2.3}$$

and substituting equations (2.2) and (2.3) into (2.1), the equations of motion are obtained as follows

$$\rho \frac{\partial^2 w(x)}{\partial t^2} + 2E_f I_f \frac{\partial^4 w(x)}{\partial x^4} - G^* b_1 h_2 \left(\frac{\partial^2 w(x)}{\partial x^2} - \frac{\partial \phi}{\partial x} \right) = f(x,t) \tag{2.4}$$

$$J \frac{\partial^2 \phi}{\partial t^2} - \frac{b h_1 E_f (h_1 + h_2)^2}{2} \frac{\partial^2 \phi}{\partial x^2} - G^* b h_2 \left(\frac{\partial w}{\partial x} - \phi \right) = 0 \tag{2.5}$$

where $w(x)$ is the transverse displacement of the blade and $\phi(x)$ is the cross-sectional rotation. In this study, the rotation terms in the equation of motion are disregarded. Here E_f is the Young's modulus, I_f is the moment of inertia, ρ is the density of the beam cross section per unit length. Moreover, h_{eb} is the wall thickness of the equivalent beam, h_{mr} is the MR fluid layer thickness, b_{mr} is the width of the MR fluid layer. For the cantilever beam, the eigenfunctions are described by

$$W_n(x) = A_1 \cosh \lambda_n x + A_2 \sinh \lambda_n x + A_3 \cos \lambda_n x + A_4 \sin \lambda_n x \tag{2.6}$$

where C_n and λ_n are defined as

$$C_n = \frac{2G^* h_{mr} \lambda_n}{E_f h_{eb} (h_{eb} + h_{mr})^2 \lambda_n{}^2 + 2G^* h_{mr}}, \quad \lambda_n = \left(\frac{2n-1}{2} \pi + e_n \right) \frac{1}{L} \tag{2.7}$$

The vibration response of the blade element is calculated by the following equations

$$w(x,t) = \sum_{n=1}^{\infty} W_n(x)\, e^{j\omega_n t}, \quad \phi(x,t) = \sum_{n=1}^{\infty} \Phi_n(x)\, e^{j\omega_n t} \tag{2.8}$$

Substituting equations (2.8) into (2.4), the following equation is obtained as

$$\sum_{n=1}^{\infty}\left[-\rho\omega_n^2 W_n(x)+2E_f I_f \frac{d^4 W_n(x)}{dx^4}-G^* b_{eb} h_{mr}\left(\frac{d^2 W_n(x)}{dx^2}-\frac{d\Phi_n(x)}{dx}\right)\right]=0 \tag{2.9}$$

Now inserting the eigenfunctions of (2.6) into (2.9), the natural frequencies of the equivalent beam containing MR fluid are calculated as follows

$$\begin{aligned}&-\rho\omega_n{}^2(A_1\cosh(\lambda_n x)+A_2\sinh(\lambda_n x)+A_3\cos(\lambda_n x)+A_4\sin(\lambda_n x))\\&+2\,\mathrm{EI}(A_4\lambda_n{}^4\cos(\lambda_n x)+A_2\lambda_n{}^4\cosh(\lambda_n x)+A_3\lambda_n{}^4\sin(\lambda_n x)\\&+A_1\lambda_n{}^4\sinh(\lambda_n x))-G^* b_{eb}h_{mr}(A_2\lambda_n{}^2\cosh(\lambda_n x)-A_4\lambda_n{}^2\cos(\lambda_n x)\\&-A_3\lambda_n{}^2\sin(\lambda_n x)+A_1\lambda_n{}^2\sinh(\lambda_n x))=0\end{aligned} \tag{2.10}$$

Boundary conditions are regulated for a clamp-free beam as follows:

$$\begin{aligned}&x=0 \quad \rightarrow \quad U_n(0)=0\\&(\frac{\partial U_n}{\partial x})_{x=0}=0\end{aligned} \tag{2.11}$$

$$\begin{aligned}&(\frac{\partial^2 U_n}{\partial x^2})_{x=L}=0\\&(\frac{\partial^3 U_n}{\partial x^2})_{x=L}=0\end{aligned} \tag{2.12}$$

If the equations (2.11) and (2.12) are applied in equation (2.6), following equations are obtained

$$\begin{aligned}&A_2+A_4=0\rightarrow A_2=-A_4\\&A_1+A_3=0\rightarrow A_1=-A_3\end{aligned} \tag{2.13}$$

$$\begin{aligned}&-\mu\omega_n{}^2A_2+2\,\mathrm{EI}\,\lambda_n{}^4(A_1+A_2)(\cosh(\lambda_n x)-\cos(\lambda_n x)+\sinh(\lambda_n x)-\sin(\lambda_n x))\\&-G^* b_{eb}h_{mr}\lambda_n{}^2(A_1+A_2)(\cos(\lambda_n x)+\cosh(\lambda_n x)+\sin(\lambda_n x)+\sinh(\lambda_n x))=0\end{aligned} \tag{2.14}$$

and using the following trigonometric formulas

$$\cosh(\lambda_n x) + \sinh(\lambda_n x) = \mathrm{e}^{\lambda_n x} \tag{2.15}$$

the new equation is organized as follows

$$\begin{aligned}&(\mu\omega_n{}^2 - 2\,\mathrm{EI}\,\lambda_n{}^4)(A_1 + A_2)\,\mathrm{e}^{\lambda_n x}(\cos(\lambda_n x) + \sin(\lambda_n x))\\&-G^* b_{eb} h_{mr} \lambda_n{}^2 (A_1 + A_2)\,\mathrm{e}^{\lambda_n x}(\cos(\lambda_n x) + \sin(\lambda_n x)) = 0\end{aligned} \tag{2.16}$$

The following two statements must be equal to each other to obtain the solution of the equation (2.16)

$$\mu\omega_n{}^2 - 2\,\mathrm{EI}\,\lambda_n{}^4 (A_1 + A_2)\,\mathrm{e}^{\lambda_n x} = -G^* b_{eb} h_{mr} \lambda_n{}^2 (A_1 + A_2)\,\mathrm{e}^{\lambda_n x} \tag{2.17}$$

and complex natural frequency obtained from equation (2.17) is given as follows

$$\omega_n = \sqrt{\frac{2E_f I_f \lambda_n{}^4 - G^* b_{eb} h_{mr} (\lambda_n C_n - \lambda_n{}^2)}{\rho}} \tag{2.18}$$

where G^* is the complex shear modulus of the MR material and is defined as $G^* = (6.125 \times 10^5 + i63773.5)$ for zero magnetic field in [3]. Natural frequency expression including the complex term is found as follows

$$|\omega_n| = \sqrt{\mathrm{Re}\,\omega_n{}^2 - \mathrm{Im}\,\omega_n{}^2} \tag{2.19}$$

Note that the eigenfunctions given in equations (2.6) are used for uniform single material beam structures.

The transverse displacement is expressed in terms of infinite series

$$w(x,t) = \sum_{n=1}^{\infty} \psi_n(x) \chi_n(t) \tag{2.20}$$

where $\chi_n(t)$ is the generalized displacement and $\psi_n(x)$ is mode shape function. If the results obtained from the equation (2.13) are arranged in the equation (2.6), the mode shape function is obtained as follows

$$\psi_n(x) = \sinh\lambda_n x - \sin\lambda_n x - \left[\frac{\sinh\lambda_n L + \sin\lambda_n L}{\cosh\lambda_n L + \cos\lambda_n L}\right](\cosh\lambda_n x - \cos\lambda_n x) \tag{2.21}$$

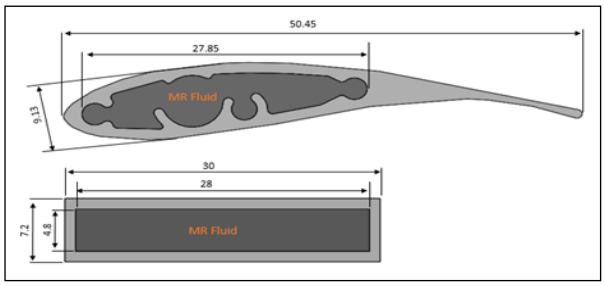

a)

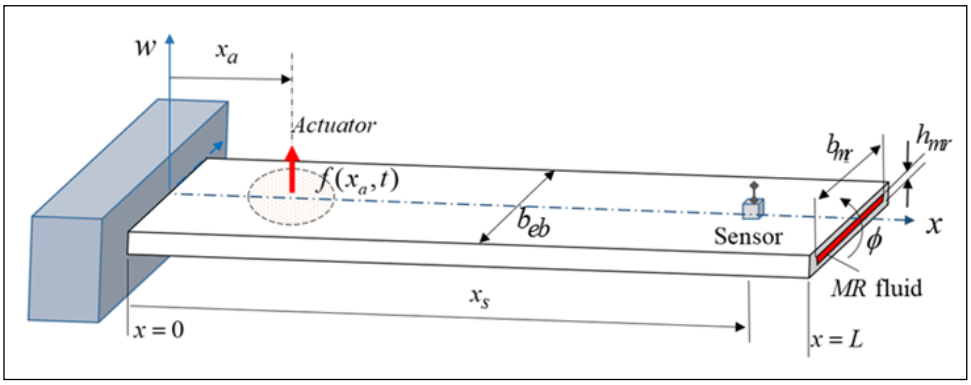

b)

Figure 2.1**:** Dimensions of the blade profile, a) cross section, b) the equivalent beam model.

2.1.1. State Space Equation

After obtaining the natural frequency equation (2.18) it is possible to constitute a dynamic equation for each structural mode. For each vibration mode of the cantilever blade structure, the separated equation of motion is given by

$$\ddot{q}_n(t) + 2\varsigma\omega_n\dot{q}_n(t) + \omega_n^2 q_n(t) = f_a(t)\psi_n(x_a) + f_d(t)\psi_n(x_d) \tag{2.22}$$

where ς is the damping coefficient and $\psi_n(x)$ is the mode shape function. Also, f_a and f_d are the actuator and disturbance forces, respectively. The state space form for each modal equation is obtained as follows

$$\dot{x}_n(t) = A_n x_n(t) + B_n u(t) + D_{wn} d(t) \tag{2.23}$$

where $x_n(t)$ is the state vector, A_n is the system matrix, B_n is the control input matrix and $u(t)$ is the control input. Also, $d(t)$ shows the disturbance input. The structure of the state vector and matrices are as follows

$$x_n = \begin{bmatrix} q_n(t) \\ \dot{q}_n(t) \end{bmatrix}, A_n = \begin{bmatrix} 0 & 1 \\ -\omega_n^2 & -2\varsigma\omega_n \end{bmatrix}, B_n = \begin{bmatrix} 0 \\ \psi_n(x_a) \end{bmatrix}, D_{wn} = \begin{bmatrix} 0 \\ \psi_n(x_d) \end{bmatrix} \tag{2.24}$$

If the modeling is extended for N modes ($n = 1, \ldots, N$), the state space model is given as

$$\dot{x}_f = \begin{bmatrix} \dot{x}_1 \\ \dot{x}_2 \\ \vdots \\ \dot{x}_N \end{bmatrix} = \begin{bmatrix} A_1 & & & 0 \\ & A_2 & & \\ & & \ddots & \\ 0 & & & A_N \end{bmatrix} \begin{bmatrix} x_1 \\ x_2 \\ \vdots \\ x_N \end{bmatrix} + \begin{bmatrix} B_1 \\ B_2 \\ \vdots \\ B_N \end{bmatrix} u + \begin{bmatrix} D_{w1} \\ D_{w2} \\ \vdots \\ D_{wN} \end{bmatrix} d$$

$$y_f = \begin{bmatrix} \psi_1(x_s) & 0 & \psi_2(x_s) & 0 & \cdots \end{bmatrix} \begin{bmatrix} x_1 \\ x_2 \\ \vdots \\ x_N \end{bmatrix} \tag{2.25}$$

The mode shape function ψ_n for the equivalent cantilever beam is defined in equation (2.21). A reduced order state space model for the control design study can be obtained by considering the first two modes of equation (2.25). The reduced order state space equation is written as

$$\begin{aligned} \dot{x}_r(t) &= A_r x_r(t) + B_r u(t) + D_{wr} d(t) \\ y_r(t) &= C_r x_r(t) \end{aligned} \tag{2.26}$$

Distributed parameter systems have theoretically infinite number of vibration modes. The state space model derived as a full model in equation (2.25) considers certain number of assumed modes. In this study, the full order model of the cantilever blade is built by considering the vibration modes up to 1 kHz. In practice, the modal contributions of the higher order modes are inconsiderable due to small modal amplitudes. Also, the reduced order model which contains the first two modes up to 60 Hz is used for controller design. The frequency responses of the full and reduced order state space models are shown in Figure 2.2.

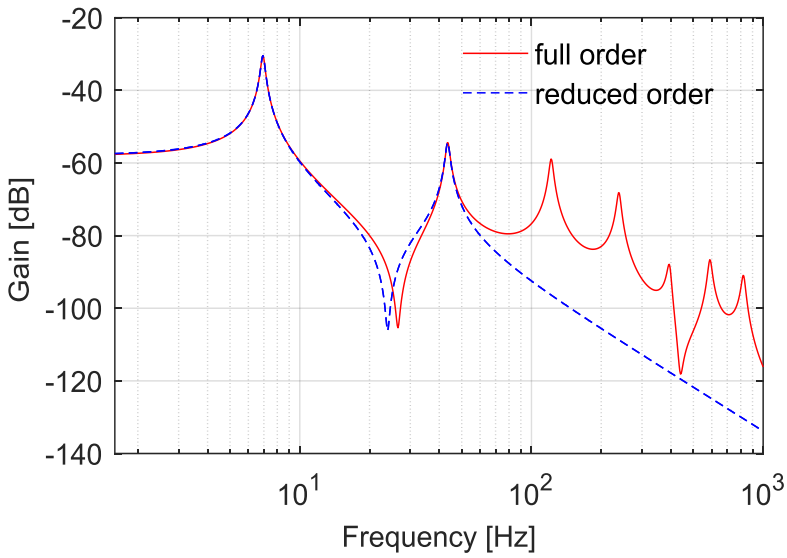

Figure 2.2: Frequency response of the blade state space models.

2.2. Lumped Parameter Model

The mathematical model of the blade profile is also obtained using the lumped parameter approach. The blade is divided into discrete elements of the same ΔL length as shown in Figure 2.3. The amount of displacement on the *w*-axis and the angle of rotation for each part are defined as $w_1, w_2, \ldots, w_n$ and $\delta_1, \delta_2, \ldots, \delta_n$. The kinetic and the potential energy of the cantilever beam for the lumped parameter model are obtained as

$$T = \sum_{n=1}^{N} \frac{1}{2} \Delta m \left(\left(\frac{dW_n}{dt} \right)^2 + \frac{1}{2} J_x \left(\frac{d\delta_n}{dt} \right)^2 \right), \qquad U = \sum_{n=0}^{N-1} \frac{1}{2} K_\delta (\Delta\delta_n)^2 \tag{2.27}$$

where J_x is the moment of inertia of the elementary airfoil. Also, the angles δ_n and the coordinates W_1 and W_n of the gravity center of the elementary airfoils are defined as follows

$$\begin{aligned} &\delta_n = \frac{w_n - w_{n-1}}{\Delta L}, \qquad \Delta\delta_n = \delta_{n+1} - \delta_n \\ &W_1 = \frac{w_1}{2}, \;\; W_n = \frac{w_n + w_{n-1}}{2} \end{aligned} \tag{2.28}$$

The bending stiffness respectively of the hollow blade element and filled blade element are calculated as

$$\begin{aligned} &K_\delta = \frac{M}{\Delta\delta} = \frac{EI_b}{\Delta L}, \\ &K_{\delta MR} = \frac{M}{\Delta\delta} = \frac{E_b I_b + G^* h_{mr} b_{mr}}{\Delta L} \end{aligned} \tag{2.29}$$

where E is Young's modulus of the blade material, I_b is the area moment of inertia of the blade cross-section and the area moment of inertia is calculated using $I_b = 0.0384 b_a [T_b^3 - T_b^3 (1 - 2\Omega)^3]$ equation defined by Steven (2013). Here b_a is the width of the chord, T_b is the height thickness and Ω is a constant ($0 < \Omega < 1$).

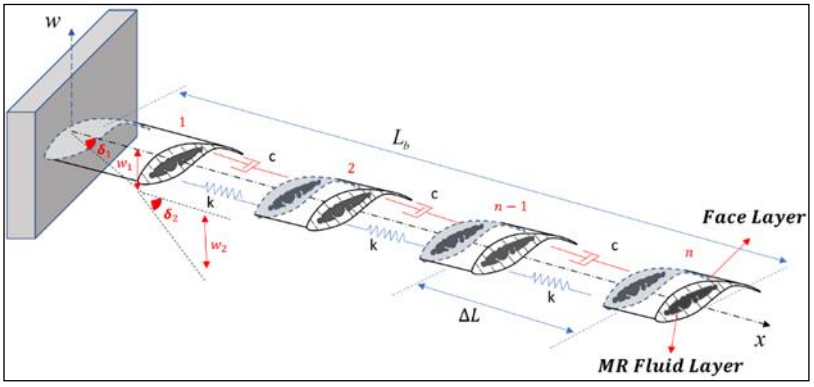

a)

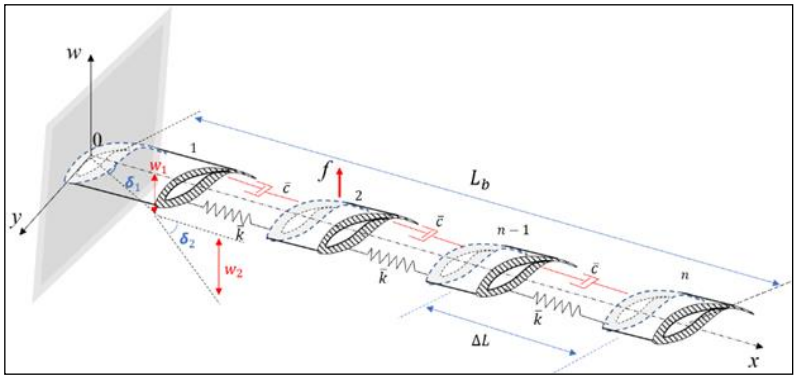

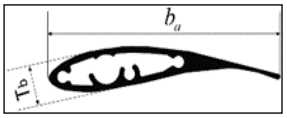

b) c)

Figure 2.3: Lumped parameter model, a) MR fluid filled blade, b) hollow blade coordinates, c) cross-section.

Since the blade element is divided into seven discrete elements the total kinetic energy for N = 7 elements is obtained as follows

$$
\begin{aligned}
T = {} & \frac{1}{2}\Delta m\left(\frac{d\left(\frac{w_1}{2}\right)}{dt}\right)^2 + \frac{1}{2}J_y\left(\frac{d\left(\frac{\delta_1}{\Delta L}\right)}{dt}\right)^2 + \frac{1}{2}\Delta m\left(\frac{d\left(\frac{w_2+w_1}{2}\right)}{dt}\right)^2 \\
& + \frac{1}{2}J_y\left(\frac{d\left(\frac{\delta_2-\delta_1}{\Delta L}\right)}{dt}\right)^2 + \frac{1}{2}\Delta m\left(\frac{d\left(\frac{w_3+w_2}{2}\right)}{dt}\right)^2 + \frac{1}{2}J_y\left(\frac{d\left(\frac{\delta_3-\delta_2}{\Delta L}\right)}{dt}\right)^2 \\
& + \frac{1}{2}\Delta m\left(\frac{d\left(\frac{w_4+w_3}{2}\right)}{dt}\right)^2 + \frac{1}{2}J_y\left(\frac{d\left(\frac{\delta_4-\delta_3}{\Delta L}\right)}{dt}\right)^2 + \frac{1}{2}\Delta m\left(\frac{d\left(\frac{w_5+w_4}{2}\right)}{dt}\right)^2 \\
& + \frac{1}{2}J_y\left(\frac{d\left(\frac{\delta_5-\delta_4}{\Delta L}\right)}{dt}\right)^2 + \frac{1}{2}\Delta m\left(\frac{d\left(\frac{w_6+w_5}{2}\right)}{dt}\right)^2 + \frac{1}{2}J_y\left(\frac{d\left(\frac{\delta_6-\delta_5}{\Delta L}\right)}{dt}\right)^2 \\
& + \frac{1}{2}\Delta m\left(\frac{d\left(\frac{w_7+w_6}{2}\right)}{dt}\right)^2 + \frac{1}{2}J_y\left(\frac{d\left(\frac{\delta_7-\delta_6}{\Delta L}\right)}{dt}\right)^2
\end{aligned}
\tag{2.30}
$$

If the equations are arranged and rewritten

$$
\begin{aligned}
T = {} & \frac{1}{2}\Delta m\left(\frac{\dot{w}_1^{\,2}}{4} + \frac{\dot{w}_2^{\,2} + 2\dot{w}_1\dot{w}_2 + \dot{w}_1^{\,2}}{4} + \frac{\dot{w}_3^{\,2} + 2\dot{w}_2\dot{w}_3 + \dot{w}_2^{\,2}}{4} + \frac{\dot{w}_4^{\,2} + 2\dot{w}_4\dot{w}_3 + \dot{w}_3^{\,2}}{4}\right. \\
& \left. + \frac{\dot{w}_5^{\,2} + 2\dot{w}_5\dot{w}_4 + \dot{w}_4^{\,2}}{4} + \frac{\dot{w}_6^{\,2} + 2\dot{w}_6\dot{w}_5 + \dot{w}_5^{\,2}}{4} + \frac{\dot{w}_7^{\,2} + 2\dot{w}_7\dot{w}_6 + \dot{w}_5^{\,2}}{4}\right) \\
& + \frac{1}{2}J_x\left(\frac{\dot{w}_1^{\,2}}{\Delta L^2} + \frac{\dot{w}_2^{\,2} - 2\dot{w}_1\dot{w}_2 + \dot{w}_1^{\,2}}{\Delta L^2} + \frac{\dot{w}_3^{\,2} - 2\dot{w}_3\dot{w}_2 + \dot{w}_2^{\,2}}{\Delta L^2} + \frac{\dot{w}_4^{\,2} - 2\dot{w}_4\dot{w}_3 + \dot{w}_3^{\,2}}{\Delta L^2}\right. \\
& \left. + \frac{\dot{w}_5^{\,2} - 2\dot{w}_5\dot{w}_4 + \dot{w}_4^{\,2}}{\Delta L^2} + \frac{\dot{w}_6^{\,2} - 2\dot{w}_6\dot{w}_5 + \dot{w}_5^{\,2}}{\Delta L^2} + \frac{\dot{w}_7^{\,2} - 2\dot{w}_7\dot{w}_6 + \dot{w}_6^{\,2}}{\Delta L^2}\right)
\end{aligned}
\tag{2.31}
$$

The total potential energy for N = 7 elements is as follows

$$
\begin{aligned}
U = & \frac{1}{2}K_\delta\left(\frac{2w_1}{\Delta L}\right)^2 + \frac{1}{2}K_\delta\left(\frac{w_2 - w_1}{\Delta L}\right)^2 \\
& + \frac{1}{2}K_\delta\left(\frac{w_3 - 2w_2 + w_1}{\Delta L}\right)^2 + \frac{1}{2}K_\delta\left(\frac{w_4 - 2w_3 + w_2}{\Delta L}\right)^2 \\
& + \frac{1}{2}K_\delta\left(\frac{w_5 - 2w_4 + w_3}{\Delta L}\right)^2 + \frac{1}{2}K_\delta\left(\frac{w_6 - 2w_5 + w_4}{\Delta L}\right)^2 \\
& + \frac{1}{2}K_\delta\left(\frac{w_7 - 2w_6 + w_5}{\Delta L}\right)^2
\end{aligned}
\tag{2.32}
$$

Arranging the equation gives

$$
\begin{aligned}
U = \frac{1}{2}K_\delta\Bigg(& \frac{4w_1}{\Delta L^2} + \frac{{w_2}^2 - 4w_1w_2 + 4{w_1}^2}{\Delta L^2} \\
& + \frac{{w_3}^2 + 4{w_2}^2 + {w_1}^2 - 4w_2w_1 - 4w_3w_2 + 2w_3w_1}{\Delta L^2} \\
& + \frac{{w_4}^2 + 4{w_3}^2 + {w_2}^2 - 4w_4w_3 - 4w_3w_2 + 2w_4w_2}{\Delta L^2} \\
& + \frac{{w_5}^2 + 4{w_4}^2 + {w_3}^2 - 4w_5w_4 - 4w_4w_3 + 2w_5w_3}{\Delta L^2} \\
& + \frac{{w_6}^2 + 4{w_5}^2 + {w_4}^2 - 4w_6w_5 - 4w_5w_4 + 2w_6w_4}{\Delta L^2} \\
& + \frac{{w_7}^2 + 4{w_6}^2 + {w_5}^2 - 4w_7w_6 - 4w_6w_5 + 2w_7w_5}{\Delta L^2}\Bigg)
\end{aligned}
\tag{2.33}
$$

The Lagrange equation can be used to derive equations of motion as follows

$$\frac{d}{dt}\left(\frac{\partial T}{\partial \dot{w}_i}\right)-\frac{\partial T}{\partial w_i}+\frac{\partial U}{\partial w_i}=Q_i \tag{2.34}$$

where Q_i shows the external force and moments. After applying the Lagrange to the total kinetic and potential energy equations, equation of motion for each degree of freedom is obtained as

$$\left(\frac{\Delta m}{2}+\frac{2J_y}{\Delta L^2}\right)\ddot{w}_1+\left(\frac{\Delta m}{4}-\frac{J_y}{\Delta L^2}\right)\ddot{w}_2+\frac{K_\delta}{\Delta L^2}\left(6w_1-4w_2+w_3\right)=0 \tag{2.35}$$

$$\begin{aligned}&\left(\frac{\Delta m}{4}-\frac{J_y}{\Delta L^2}\right)\ddot{w}_1+\left(\frac{\Delta m}{2}+\frac{2J_y}{\Delta L^2}\right)\ddot{w}_2+\left(\frac{\Delta m}{4}-\frac{J_y}{\Delta L^2}\right)\ddot{w}_3\\&+\frac{K_\beta}{\Delta L^2}\left(-4w_1+6w_2-4w_3+w_4\right)=f_{MR_patch}\end{aligned} \tag{2.36}$$

$$\begin{aligned}&\left(\frac{\Delta m}{4}-\frac{J_y}{\Delta L^2}\right)\ddot{w}_2+\left(\frac{\Delta m}{2}+\frac{2J_y}{\Delta L^2}\right)\ddot{w}_3+\left(\frac{\Delta m}{4}-\frac{J_y}{\Delta L^2}\right)\ddot{w}_4\\&+\frac{K_\beta}{\Delta L^2}\left(w_1-4w_2+6w_3-4w_4+w_5\right)=0\end{aligned} \tag{2.37}$$

$$\begin{aligned}&\left(\frac{\Delta m}{4}-\frac{J_y}{\Delta L^2}\right)\ddot{w}_3+\left(\frac{\Delta m}{2}+\frac{2J_y}{\Delta L^2}\right)\ddot{w}_4+\left(\frac{\Delta m}{4}-\frac{J_y}{\Delta L^2}\right)\ddot{w}_5\\&+\frac{K_\beta}{\Delta L^2}\left(w_2-4w_3+6w_4-4w_5+w_6\right)=0\end{aligned} \tag{2.38}$$

$$\begin{aligned}&\left(\frac{\Delta m}{4}-\frac{J_y}{\Delta L^2}\right)\ddot{w}_4+\left(\frac{\Delta m}{4}+\frac{J_y}{\Delta L^2}\right)\ddot{w}_5+\left(\frac{\Delta m}{4}-\frac{J_y}{\Delta L^2}\right)\ddot{w}_6\\&+\frac{K_\beta}{\Delta L^2}\left(w_3-4w_4+6w_5-4w_6+w_7\right)=0\end{aligned} \tag{2.39}$$

$$\left(\frac{\Delta m}{4}-\frac{J_y}{\Delta L^2}\right)\ddot{w}_5+\left(\frac{\Delta m}{4}+\frac{J_y}{\Delta L^2}\right)\ddot{w}_6+\left(\frac{\Delta m}{4}-\frac{J_y}{\Delta L^2}\right)\ddot{w}_7$$
$$+\frac{K_\beta}{\Delta L^2}(w_4-4w_5+5w_6-2w_7)=0 \tag{2.40}$$

$$\left(\frac{\Delta m}{4}-\frac{J_y}{\Delta L^2}\right)\ddot{w}_6+\left(\frac{\Delta m}{4}+\frac{J_y}{\Delta L^2}\right)\ddot{w}_7+\frac{K_\beta}{\Delta L^2}(w_5-2w_6+w_7)=0 \tag{2.41}$$

where J_y is the moment of inertia about the z-axis which is perpendicular to the xy-plane of the elementary blade.

The equations of motion are obtained for each blade element and written in matrix form as follows

$$\begin{bmatrix} \psi & \beta & 0 & 0 & 0 & 0 & 0 \\ \beta & \psi & \beta & 0 & 0 & 0 & 0 \\ 0 & \beta & \psi & \beta & 0 & 0 & 0 \\ 0 & 0 & \beta & \psi & \beta & 0 & 0 \\ 0 & 0 & 0 & \beta & \psi & \beta & 0 \\ 0 & 0 & 0 & 0 & \beta & \psi & \beta \\ 0 & 0 & 0 & 0 & 0 & \beta & \psi/2 \end{bmatrix}\begin{bmatrix} \ddot{w}_1 \\ \ddot{w}_2 \\ \ddot{w}_3 \\ \ddot{w}_4 \\ \ddot{w}_5 \\ \ddot{w}_6 \\ \ddot{w}_7 \end{bmatrix}+\frac{K_\delta}{\Delta L^2}\begin{bmatrix} 6 & -4+\lambda K_w & 1 & 0 & 0 & 0 & 0 \\ -4 & 6 & -4 & 1 & 0 & 0 & 0 \\ 1 & -4 & 6 & -4 & 1 & 0 & 0 \\ 0 & 1 & -4 & 6 & -4 & 1 & 0 \\ 0 & 0 & 1 & -4 & 6 & -4 & 1 \\ 0 & 0 & 0 & 1 & -4 & 5 & -2 \\ 0 & 0 & 0 & 0 & 1 & -2 & 1 \end{bmatrix}\begin{bmatrix} w_1 \\ w_2 \\ w_3 \\ w_4 \\ w_5 \\ w_6 \\ w_7 \end{bmatrix}=\begin{bmatrix} 0 \\ K_i \\ 0 \\ 0 \\ 0 \\ 0 \\ 0 \end{bmatrix} i_C \tag{2.42}$$

where K_w and K_i are parameters of the linear electromagnetic force. The other parameters are given as

$$\psi=\left(\frac{\Delta m}{2}+\frac{2J_y}{\Delta L^2}\right),\qquad \beta=\left(\frac{\Delta m}{4}-\frac{J_y}{\Delta L^2}\right) \tag{2.43}$$

$$\lambda=\frac{\Delta L^2}{K_\delta} \tag{2.44}$$

Equation (2.42) can also be written as

$$M\ddot{w} + Kw = Fu \tag{2.45}$$

If a linear damping is considered, the equation of motion obtained in (2.45) extends to

$$M\ddot{w} + C\dot{w} + Kw = Fu \tag{2.46}$$

C is constructed with a linear combination of the mass and stiffness matrices $C = \chi M + \gamma K$, and χ, γ are constants.

2.2.1. State-Space Model

The equation of motion (2.46) should be transform to a suitable form to truncate some of the modes for a control design. First, a transformation from physical coordinate to the modal coordinate is realized as follows

$$\ddot{\xi} + \Lambda\dot{\xi} + \Omega^2\xi = f_0\, u \tag{2.47}$$

The modal matrix Φ is used to transform the system matrices of $I = \Phi^T M \Phi$, $\Omega^2 = \Phi^T K \Phi$, $\Lambda = 2\varsigma\,\Omega$ and $f_0 = \Phi^T F$. A state space form of equation (2.47) can be obtained as

$$\begin{aligned} \dot{x}_f(t) &= A_f x_f(t) + B_f u(t) + D_f d(t) \\ y_r(t) &= C_f x_f(t) \end{aligned} \tag{2.48}$$

where the structure of the system matrices are as follows

$$A_f = \begin{bmatrix} 0 & I \\ -\Omega^2 & -\Lambda \end{bmatrix},\ B_f = \begin{bmatrix} 0 \\ f_0 \end{bmatrix},\ C_f = \begin{bmatrix} C_0\Phi & 0 \end{bmatrix},\ D_f = \begin{bmatrix} 0 \\ d_0 \end{bmatrix} \tag{2.49}$$

where D_f is the disturbance input vector defined for a control design. Note that d_0 can be obtained in the modal transformation $d_0 = \Phi^T H$, where H is the disturbance input vector. To design a controller, a reduced order system model is obtained from equation (2.48)

$$\begin{aligned} \dot{x}_r(t) &= A_r x_r(t) + B_r u(t) + D_r d(t) \\ y_r(t) &= C_r x_r(t) \end{aligned} \tag{2.50}$$

The state space model obtained as a full model in equation (2.48) considers a certain number of modes since the blade has theoretically infinite number of modes. In this study, the full order model of the cantilever blade element was formed by considering the first seven natural frequencies. Since the modal contributions of the higher order modes are inconsiderable due to small modal amplitudes the reduced order model constituted with only two vibration modes is preferred for a control design study.

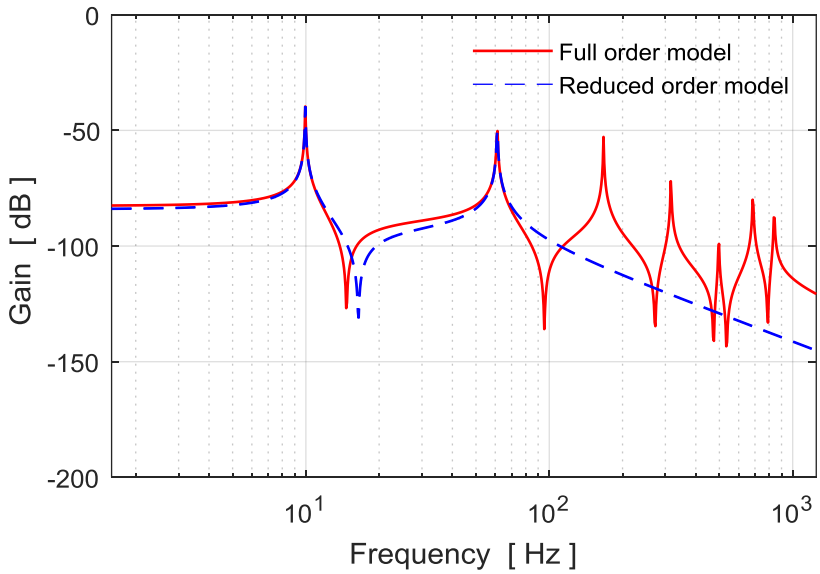

Figure 2.4: Frequency response of the blade model.

2.3. Natural Frequency Analysis

In the previous sections two different modeling approach is applied to derive the equation of motion of the blade element. At this stage it is better to compare the

natural frequencies of the blade with obtained model and experimental results. Also, the effect of the MR fluid in the case of filled into the blade element is analyzed. The photo of the experimental system setup for natural frequency analysis is shown in Figure 2.5. To show the effect of the MR fluid in the structure two identical feature blade elements which one of it is hollow and the other is filled with MR fluid was used. Each blade element is fixed at one end using a clamp and an accelerometer is attached on it. Natural frequency analysis of the blade was experimentally realized using a Bruel&Kjaer-3053 vibration analyzer with FFT analysis mode. In the first case of the analysis, the frequency measurements were taken for the hollow blade element. After that, the blade element filled with MR fluid was used for the natural frequency analysis.

The experimental frequency responses of the hollow and MR fluid-containing blade structures presented in Figure 2.6. Since the natural frequencies shifted lower values, the blade profile containing MR fluid is only affected by the fluid mass inside the structure when it is not in the magnetic field. MR fluid has no effect on the rigidity of the structure. Therefore, the natural frequency values of the hollow wing are higher than those of the MR fluid filled wing profile due to less mass.

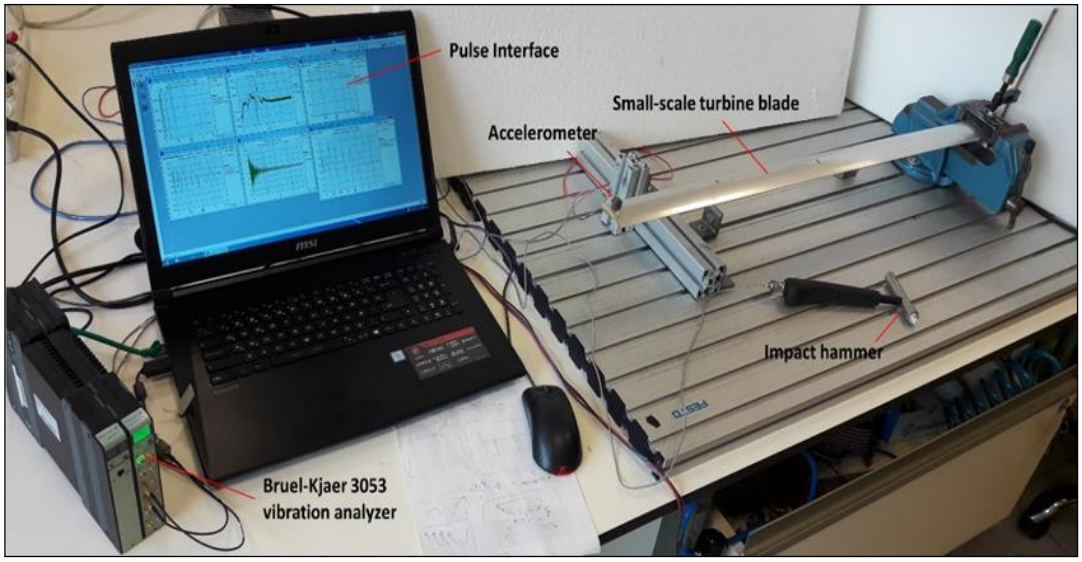

Figure 2.5: Experimental setup.

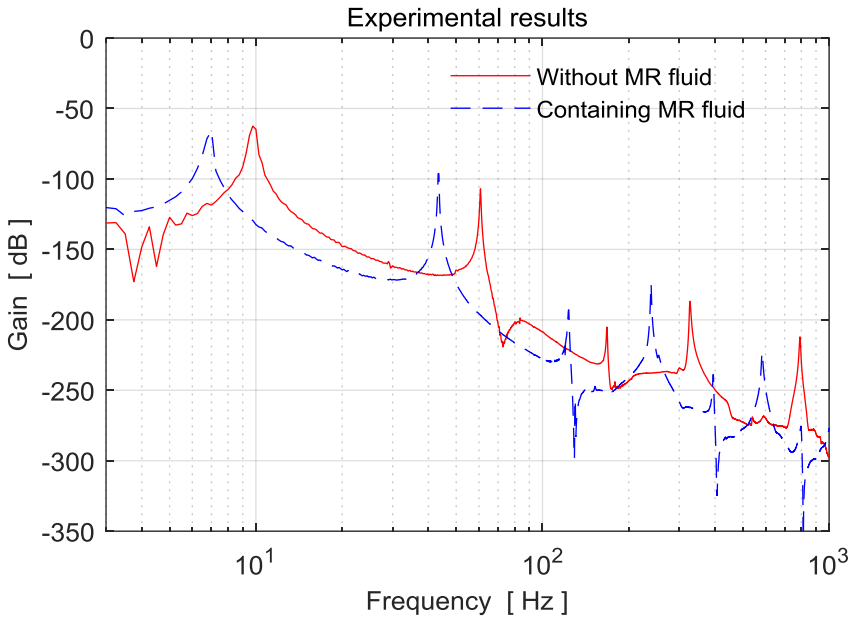

Figure 2.6: Experimental frequency responses of the hollow and MR fluid filled blade.

For the numerical analysis of the blade profile, a three-dimensional model of the blade element was created in Solidworks and transfered to Anysys Workbench finite element software. The material properties of the MR fluid in the numerical model was taken as defined in references [Fonseca et al., 2016; Weiss et al., 1994]. Using the modal analysis mode of the Ansys, the natural frequencies of the blade element model were obtained. Finally, the equivalent beam containing MR fluid was created and a modal analysis was performed in the Ansys in Figure 2.7. A lumped parameter model of the equivalent beam containing MR fluid was also obtained as defined in Section 2.1. The results of the first five natural frequencies using the defined approaches are given in Table 2.1. From these analysis results, it is observed that the values of the natural frequencies for different approaches are close to each other. The results of the lumped parameter model have been verified using FEM analysis by examining the original profile and the equivalent beam.

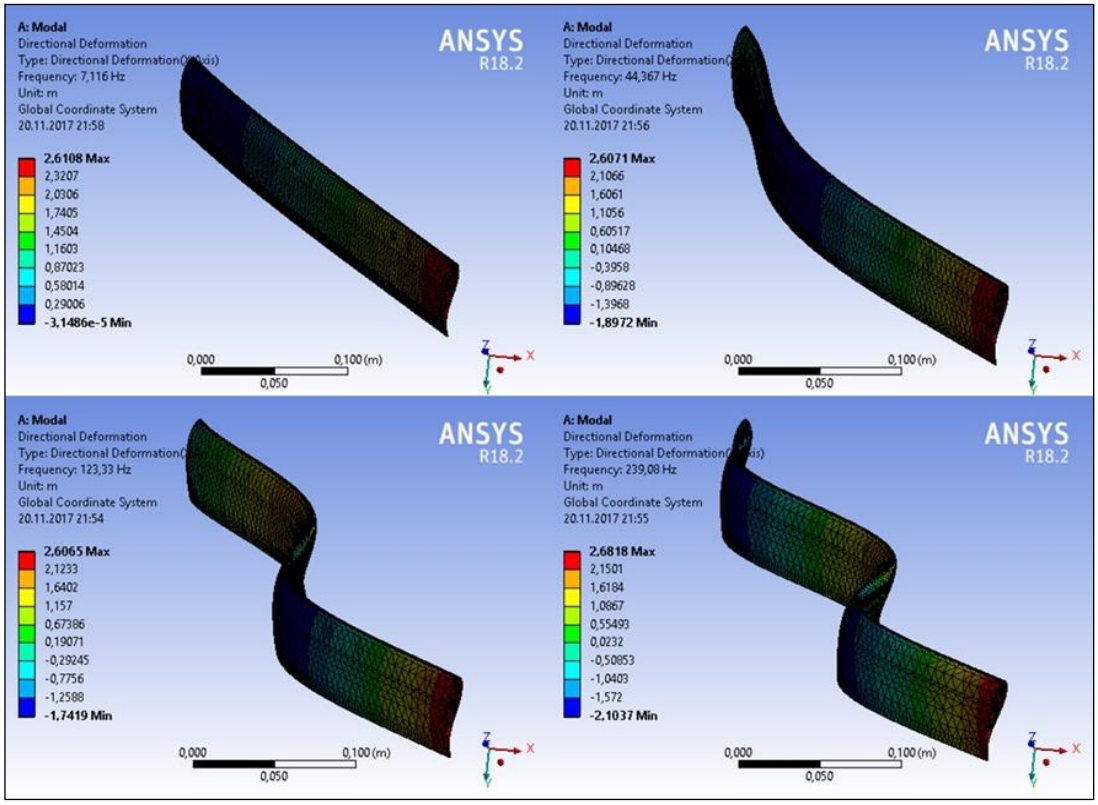

Figure 2.7: Mode shape and natural frequency of the blade using FEM**.**

Table.2.1: Natural frequencies of the blade vibration modes.

Mode	**Blade Profile Experimental Results [Hz]**		**Blade profile-MR filled**		**Equivalent beam – MR filled**	
	Hollow	**MR filled**	**ANSYS Results [Hz]**	**Lumped Model [Hz]**	**ANSYS Results [Hz]**	**Lumped Model [Hz]**
1	9.5	7	7.11	7.46	7.12	7.44
2	59.5	43.25	44.36	44.41	44.45	44.37
3	167	122.75	123.33	125.32	123.72	125.17
4	326	239.25	239.08	240.08	240.20	239.90
5	531.5	394.50	389.48	377.21	392.12	376.94

3. MR FLUID BLADE APPLICATIONS

In the thesis, two different magnetorheological fluid applications are proposed for active vibration control. For each treatment of the MR fluid a force identification is realized and the behavior of MR fluid under the effect of the electromagnetic actuator is characterized.

3.1. MR Layer Patch

A layer patch of the MR fluid is prepared by using a thin plastic bag. The width and length of the patch shown in Figure 3.1 are decided according to the width of the blade and the diameter of the electromagnet. The patch is filled with the Lord Corporation's MRF-132DG type fluid product. The average thickness of the MR patch after filling is 4.6 mm and the volume of MR fluid used in the patch is 7 ml. The locked plastic bag is glued to ensure that leak-proof of the open edge as shown in Figure 3.1. The MR patch is stuck on the blade with a tape to prevent large bag flexibility under magnetic field as shown in Figure 3.2.

The MR fluid patch presented in this study has some differences from the works done in the literature. The MR fluid is generally filled into a layer along the length of a sandwich structure, which means excess weight and loss of material. So, the use of the MR patch in control applications is more advantageous than using it as a layer. Moreover, the MR patch is easily formed and may take the shape of the structure when it is attached. It can be applicable to any structure locally.

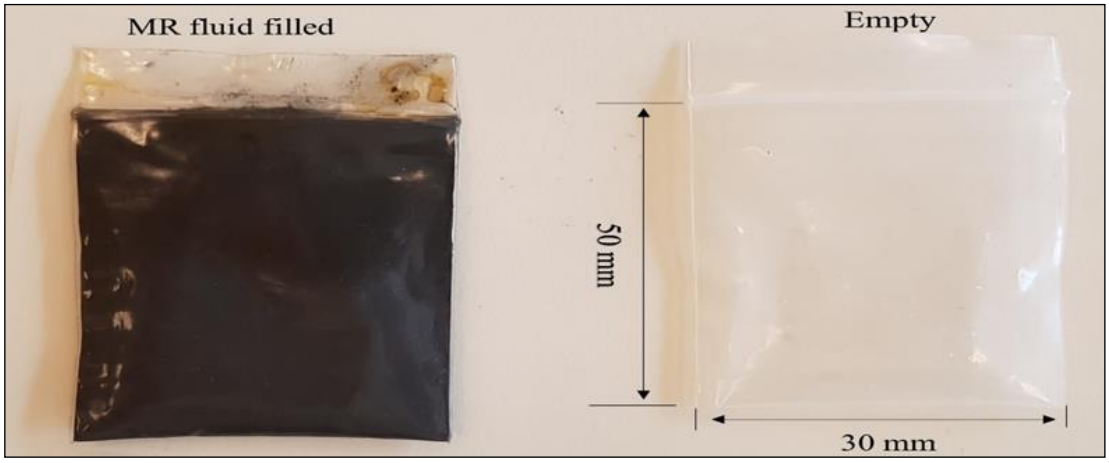

Figure 3.1: Structure of the MR fluid patch.

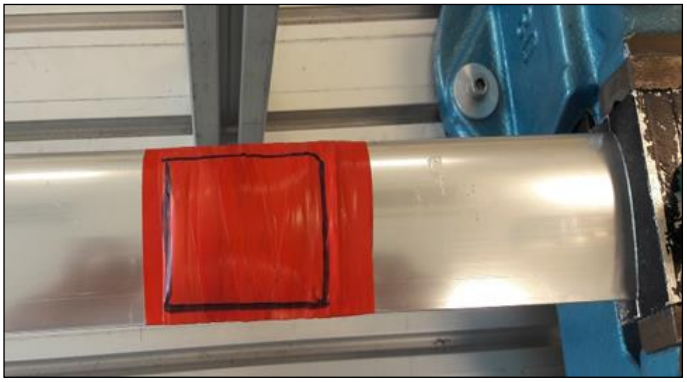

Figure 3.2: The MR patch attached on the blade.

3.1.1. Force Characterization

The electromagnet is positioned opposing the MR patch with an air gap over the blade element to apply magnetic field to the patch as illustrated in Figure 3.3. When the current is applied to the electromagnet and a magnetic field is created, the iron particles in the MR patch become ordered and an attractive force on the blade is generated so that the vibrations of the blade are suppressed. The magnitude of the force depends on the magnetic flux generated by the controller according to the displacement information of the blade obtained using an optical sensor in a feedback control structure.

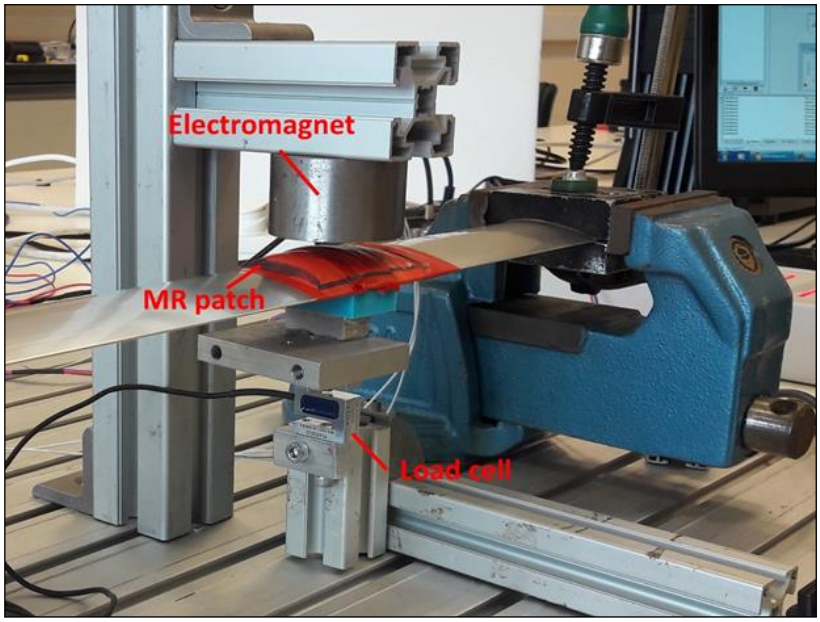

Figure 3.3: The electromagnet positioned over the MR patch.

The interaction between the electromagnet and the MR patch should be modeled for a control design study. To understand the interaction phenomenon cross section views are illustrated in Figures 3.4(a)-(c). At the initial state as shown in Figure 3.4(a), the electromagnet is positioned over the blade with an air gap of w_0. Although the MR patch is tightly fixed on the blade, an expansion of the plastic bag is unavoidable under the force effect. When the current is started to apply to the electromagnet shown in Figure 3.4(b), the MR patch is attracted by the electromagnet and an expansion with the amount of w_p is occurred due to flexibility of the plastic bag. At this stage, the blade is not moving and the magnetic force and current that extend the MR patch are f_0 and i_0 , respectively. After the expansion of the patch is over the MR patch with the blade move toward the electromagnet. The electromagnetic force is defined as

$$f_{MR}(t) = k\frac{[i_0 + i_c(t)]^2}{\left[w_0 - (w_p + w(t))\right]^2} \tag{3.1}$$

where $k = (1/4)\mu_0 N^2 A$. Here A is the area of the electromagnet, N is the number of the coil turn and μ_0 is the vacuum permeability. Also i_c is the control current. The electromagnetic force is linearized around (i_0, w_0) values as follows.

$$f_p(t) = K_w w + K_i i_c \tag{3.2}$$

where $K_w = 2k(i_0^2 / w_0^3)$ and $K_i = 2k(i_0 / w_0^2)$.

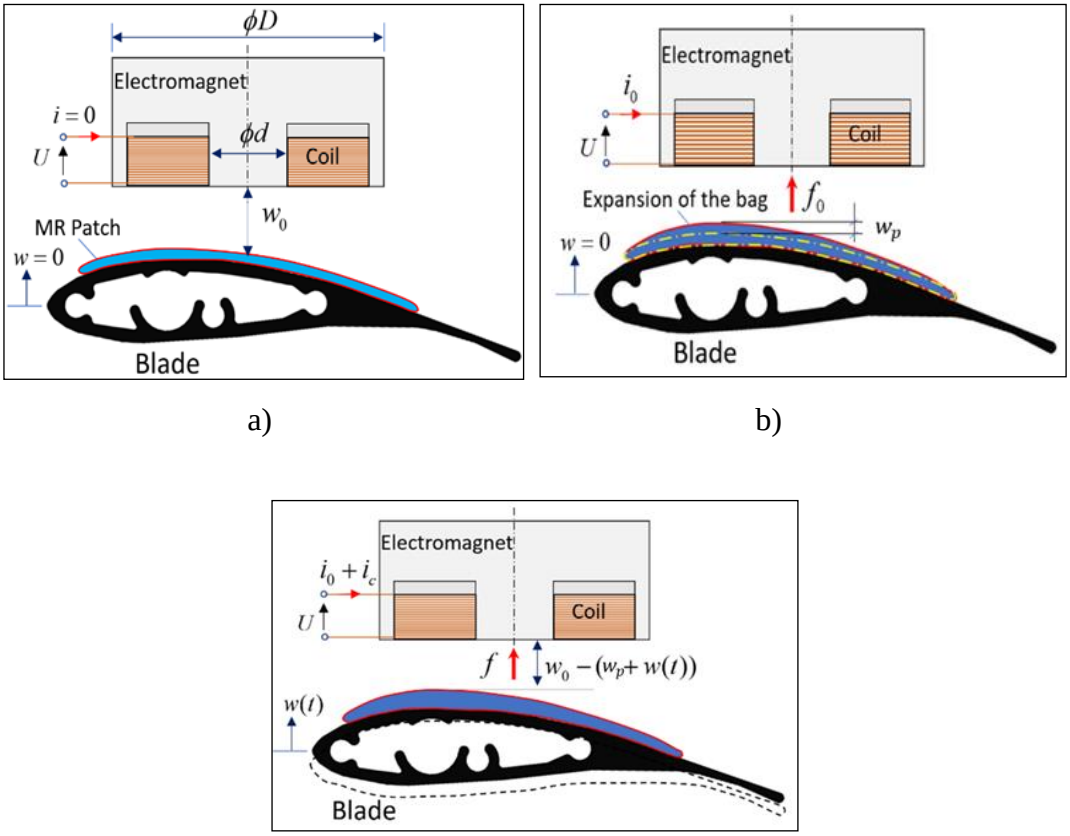

a) b)

c)

Figure 3.4: Interaction model between the electromagnet and the MR patch, a) initial state, b) expansion of the MR patch, c) control of the blade.

Since the MR patch has some flexibility the response force of the MR patch layer to the electromagnet force input should be investigated. It is important to show how much electromagnetic force is transmitted to the MR patch. To understand the force variation at the MR patch side a load cell is installed under the blade as shown in Figure 3.3. It is not possible to measure electromagnetic force directly, but the magnetic field can be measured by a gauss meter. The experimental force f_e exerted by the electromagnet obtained using the experimental data with the following equation

$$f_e = \frac{A}{\mu_0} B^2 \tag{3.3}$$

where B is the magnetic field measured by using a gauss meter. The variations of the experimental forces are shown in Figure 3.5. In these experiments, the air gap

between the electromagnet and MR patch is set to 1 mm. Table 3.1 also shows the data of the measured experimental forces in different currents. At large coil currents, the loss is increasing as seen in Figure 3.5 and Table 3.1.

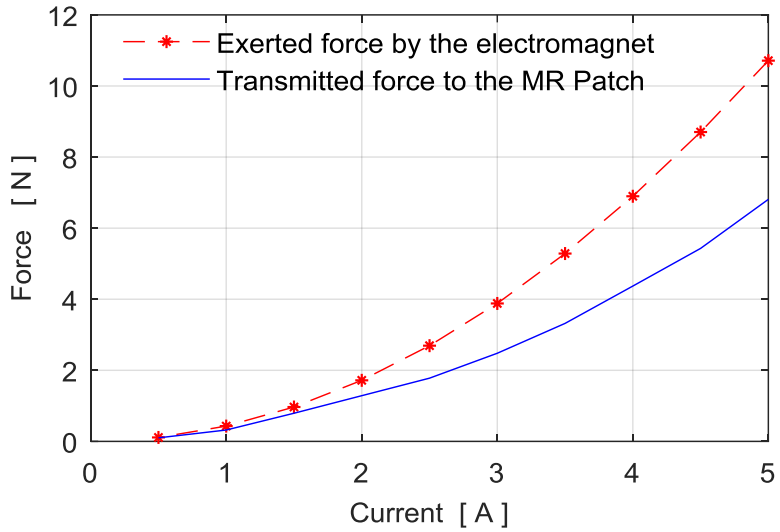

Figure 3.5: Variation of the experimental electromagnetic force and the response force of the MR patch.

Table 3.1: The measured forces in different currents.

Applied Current [A]	**Force at MR Patch Side [N] (Measured by the Load cell)**	**Electromagnet Force [N] (Computed from Gaussmeter Measurements)**	**Loss %**
5	6.91	10.71	35.4
4.5	5.73	8.70	34.1
4	4.52	6.89	34.3
3.5	3.43	5.28	35.0
3	2.58	3.88	33.5
2.5	1.87	2.69	30.4
2	1.29	1.71	25.1
1.5	0.78	0.96	18.7
1	0.34	0.43	20.9
0.5	0.10	0.12	16.6

To understand the dependence of the response force to the coil current and air gap another force characterization is realized. For this aim the coil current of the electromagnet is increased from 0.5 ampere to 5 amperes by setting the electromagnet at a fixed distance of 1 mm from the patch surface. Similarly, while the coil current set to 5 amperes, the distance between the electromagnet and the

blade surface is increased by 1 mm for each measurement. Figures 3.6(a)-(b) show the variation of response force with the coil current and the displacement respectively. As seen in these figures the characteristics of the force is nonlinear with respect to the displacement and current.

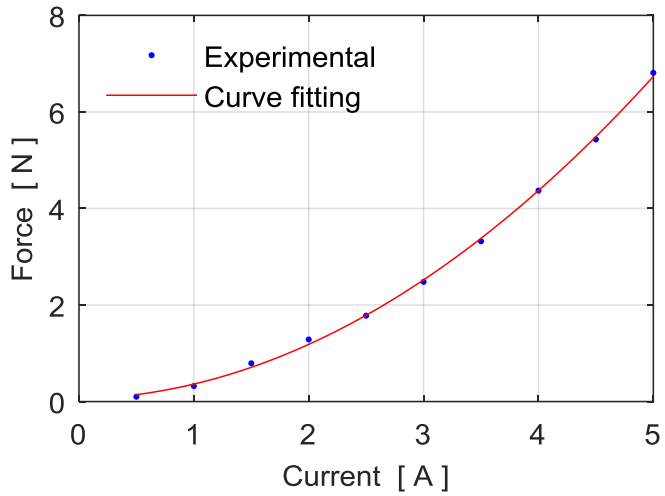

a)

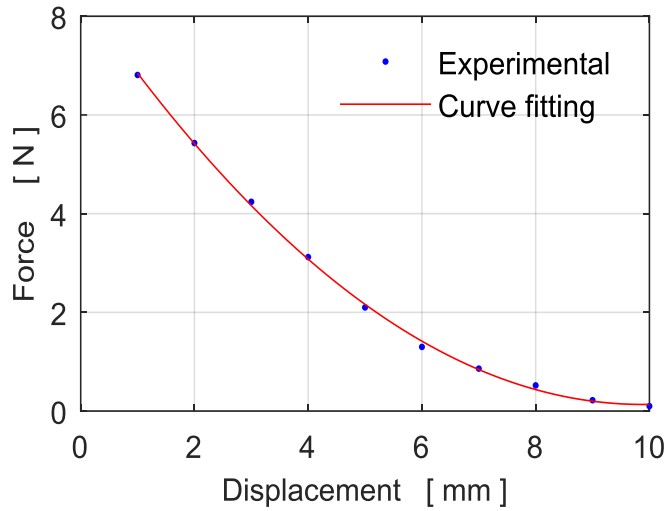

b)

Figure 3.6: Variation the response force, a) with current, b) with displacement.

3.2. MR Fluid Filled Blade

As a second active control application, the layer patch is removed and MR fluid is injected completely into the blade element since the middle of the blade is

empty. Both ends of the blade element are closed with leak proof material after filling. Figure 3.7. shows the blade structure used for the control study.

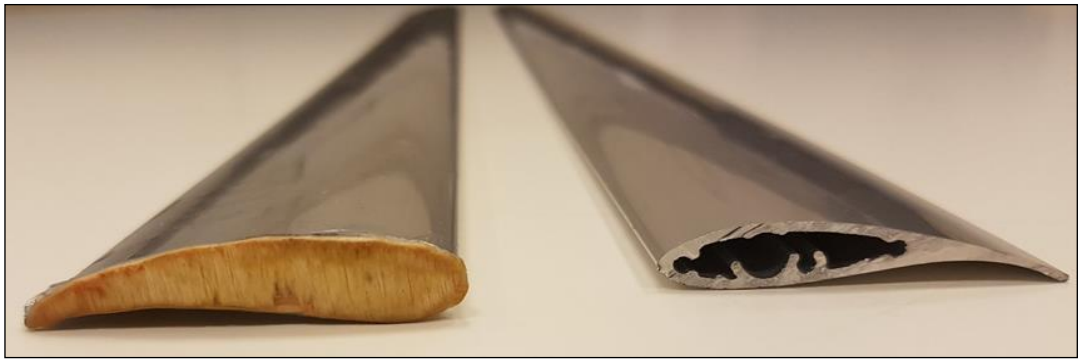

Figure 3.7: Blade profile, a) filled with MR fluid, b) hollow blade.

The amount of the MR fluid filled into the blade profile is 87 mL. The code number of the fluid is MR 122EG. The experimental frequency responses of the hollow and MR fluid-containing blade structures is presented in the previous section of Figure 2.6. Some tests are realized to understand the response performance of the MR blade to the electromagnet. The experimental blade vibrations in the case of constant electromagnet currents i_s without any feedback are given in Figure 3.8(a). The applied currents are also shown in Figure 3.8(b). As seen in Figure 3.8(a), the blade vibrations have some peaks at the upper side of the amplitude due to the pulling force effect of the electromagnet.

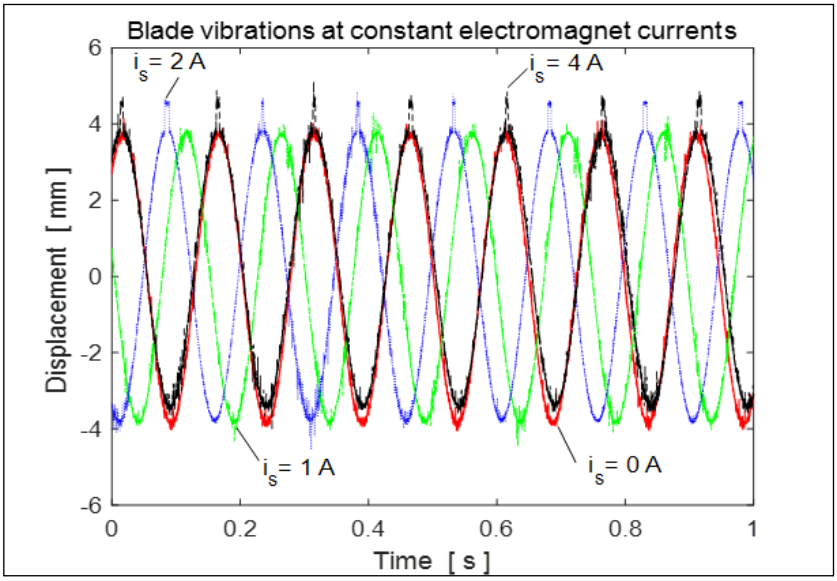

a)

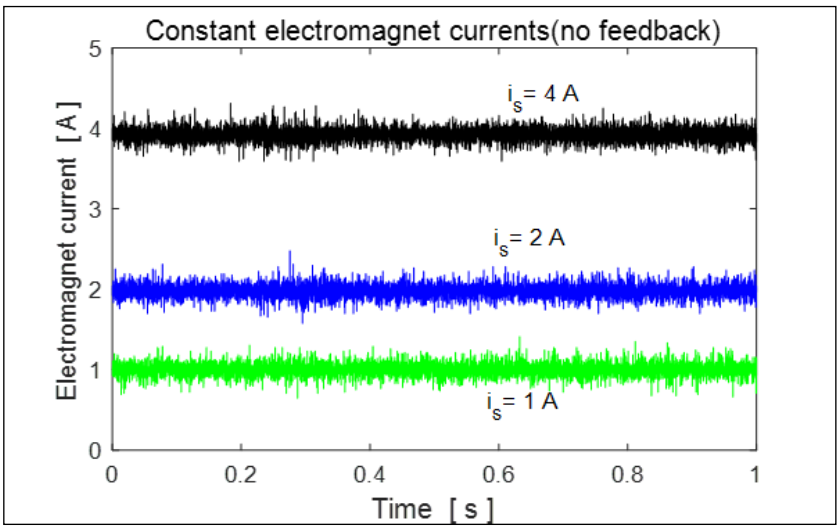

b)

Figure 3.8: Experimental results at constant magnetic field, a) blade vibrations, b) electromagnet currents.

3.2.1. Force Identification

The electromagnetic actuator used in the patch case is also used to control the vibration of the MR filled blade. In this section the force relation between the electromagnet and the MR fluid is derived to have a model. The main difference defined in the previous section is that there is no plastic bag flexibility in fully filled blade case. MR behavior has the same characteristics and the magnetic field generated by the electromagnet attracts the iron particles inside the MR fluid. The

amount of fluid inside the blade is much more compared to patch case and only the electromagnet location collects the iron particles.

To explain the interaction phenomenon cross-section views are illustrated in Figures 3.9(a)-(c). The electromagnet is positioned over the MR blade element with an air gap (Figure 3.10(a)). When the current is supplied to the electromagnet and a magnetic field is generated, the iron particles inside the MR fluid become ordered and an attractive force is applied on the blade (Figure 3.9(b)). At this stage, the blade stands at the nominal position and still not moving. When the current increases the attractive force also increases and the blade moves to the actuator side as shown in Figure 3.9(c). The magnitude of the force depends on the magnetic flux given by the controller according to the optical sensor in a feedback control structure. The nonlinear magnetic force is derived as

$$f_m(t) = k\frac{(i_0 + i_c(t))^2}{\left[w_0 - w(t)\right]^2} \tag{3.4}$$

where i_c is the control current. The electromagnetic force is linearized around (i_0, w_0) values as follows.

$$f_a(t) = K_w w + K_i i_c \tag{3.5}$$

where $K_w = 2k(i_0^2 / w_0^3)$ and $K_i = 2k(i_0 / w_0^2)$.

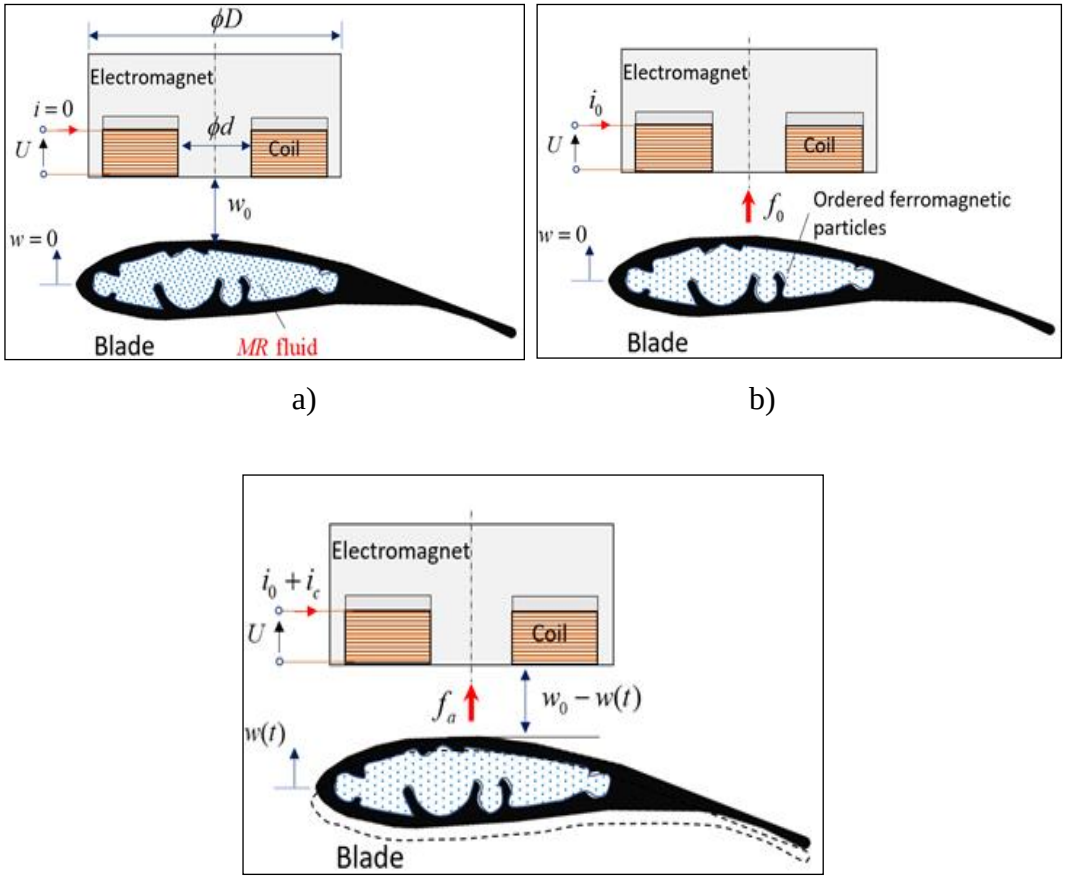

a) b)

c)

Figure 3.9**.** Illustration of the MR blade and electromagnetic actuator interaction, a) initial setting, b) the application of the bias current i_0, c) the control force f_a generation.

To understand the level of the transmitted force to the MR blade element a similar characterization study is realized as is done in Section 3.1.1. The setup is prepared as shown in Figure 3.10(a). The measured experimental forces are shown in Figure 3.10(b). The variation of the force is nonlinear and reflects the electromagnetic force characteristics. Also, it is observed that the loss in the transmitted force is increasing at large coil currents as seen in Figure 3.10(b).

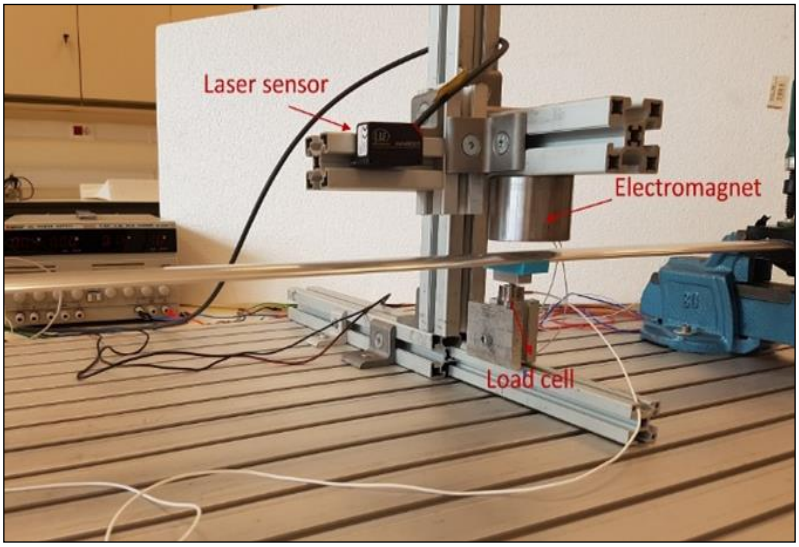

a)

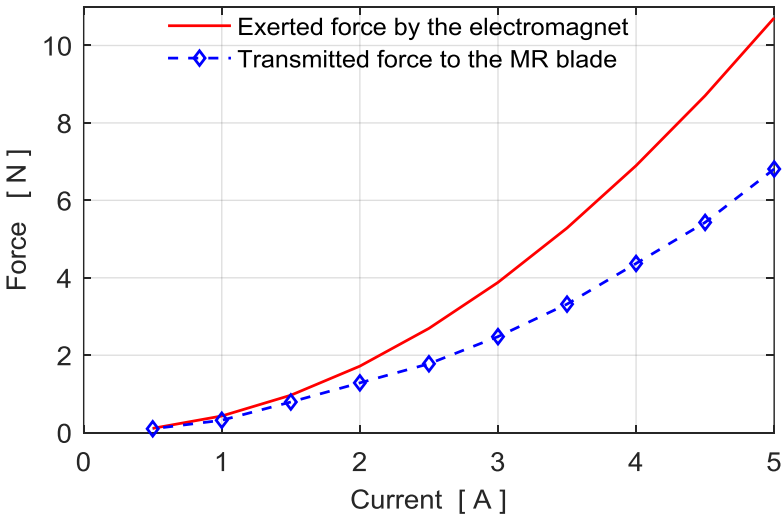

b)

Figure 3.10: Force measurements, a) Experimental setup, b) Variation of the electromagnetic force and the transmitted force.

4.MULTI-OBJECTIVE H_2/H_∞ CONTROL DESIGN

A control design study is necessary for active vibration control of the blade element with MR fluid. A multi-objective control design is preferred due to fulfilling the time domain and frequency domain objectives at the same time. Since distributed mass systems like beams and plates have infinite number of structural modes and a model reduction is necessary for state-space models, neglected or unmodeled high-frequency dynamics in the blade element may cause the spillover effect. To avoid such effects a norm based robust control design is a good choice due to shaping the controller gain at higher frequencies with design filters.

4.1. Control Objectives

In norm based robust control, H_2 and H_∞ norm performances are two important specifications. While H_∞ performance is convenient to enforce robustness against model uncertainty, H_2 performance is useful to handle stochastic aspects such as measurement noise and control cost. The generalized control design block structure of the multi-objective control is shown in Figure 4.1. The output channel z_∞ is associated with the H_∞ performance while the channel z_2 is associated with the H_2 performance. Also, $T_\infty(s)$ and $T_2(s)$ are the closed-loop transfer functions from w_d to z_∞ and z_2, respectively. The state-space realization of the augmented plant having both design objectives is given by

$$\begin{aligned}
\dot{x} &= Ax + B_1 w_d + B_2 u \\
z_\infty &= C_\infty x + D_{\infty 1} w_d + D_{\infty 2} u \\
z_2 &= C_2 x + D_{21} w_d + D_{22} u \\
y &= C_y x + D_{y1} w_d
\end{aligned} \tag{4.1}$$

Using the closed loop transfer functions, minimization of a trade-off criterion can be formed such that design a controller K(s) that minimizes the mixed H_2 / H_∞ norm criterion

$$\alpha \|T_\infty(s)\|_\infty^2 + \beta \|T_2(s)\|_2^2 \quad , \alpha, \beta \geq 0 \tag{4.2}$$

subject to

$$\|T_\infty(s)\|_\infty < \gamma_0 \, , \; \|T_2(s)\|_2 < \nu_0 \; , \; \gamma_0, \nu_0 > 0 \tag{4.3}$$

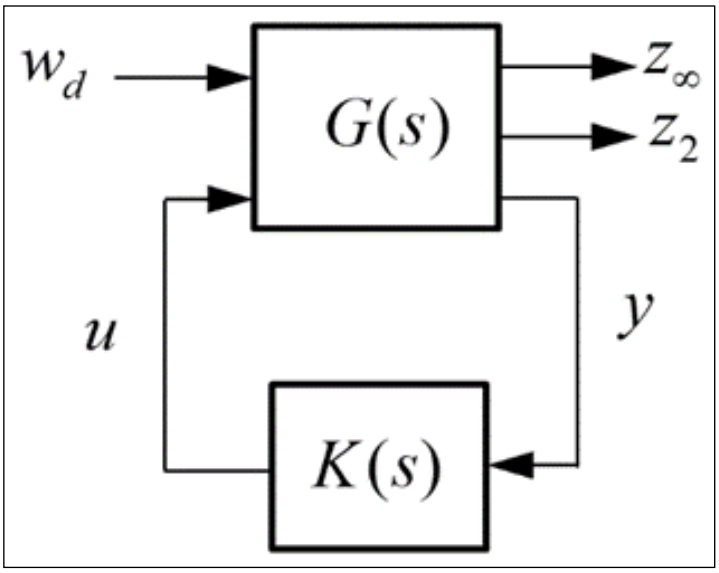

Figure 4.1: Multi-objective control structure.

4.2. Control Design Blocks

In this study, three different control design blocks are studied for different sensitivity shaping conditions. The analysis of sensitivity functions gives quantitative information about how the nominal model is sensitive to uncertainties of the system disturbances or measurement noises. There are two main objectives in the considered design blocks. The first objective is the robustness against neglected high frequency dynamics. This objective satisfies that uncontrolled high frequency vibration modes of the blade may not be excited by the controller due to spillover effect. The second objective is to reject the disturbance entering at the blade element. Vibration suppression of the blade can be considered in the second objective.

- Design-1.

The control design block structure for Design-1 study is shown in Figure 4.2. In this block, P(s) is the reduced order plant model and K(s) is the controller that will be designed. In the blade system, the input n shows the aerodynamic disturbances and sensor noise. Also, the input d represents the disturbance caused by unstructured uncertainty or unmodeled high frequency dynamics in the system. The controlled variables z_∞ and z_2 are outputs of the transfer functions obtained for each external input. Consider the points p_1, p_2 and p_3 in Figure 4.2. The transfer functions from n to p_1, p_2 and p_3 are obtained as

$$\begin{aligned} G_{p_1 n}(s) &= -\frac{K(s)\varepsilon}{I + P(s)K(s)} = -\varepsilon K(s)S(s) \\ G_{p_2 n}(s) &= G_{p_1 n}(s) \\ G_{p_3 n}(s) &= \frac{\varepsilon}{I + P(s)K(s)} = \varepsilon S(s) \end{aligned} \tag{4.4}$$

where $S(s) = (I + P(s)K(s))^{-1}$ is the sensitivity function. Moreover, the transfer functions from the disturbance d to the points p_1, p_2 and p_3 are given as

$$\begin{aligned} G_{p_1 d}(s) &= -\frac{P(s)K(s)}{I + P(s)K(s)} = -T(s) \\ G_{p_2 d}(s) &= G_{p_1 d}(s) \\ G_{p_3 d}(s) &= \frac{P(s)}{I + P(s)K(s)} = T_c(s) \end{aligned} \tag{4.5}$$

Here $T(s)$ is the complementary sensitivity function and $T_c(s)$ is the settling function. In a control system design, shaping with $T(s)$ transfer function is preferable for noise attenuation and tracking. Also, $T(s)$ transfer function is important for robust stability with respect to multiplicative uncertainties at the system output. In Design-1 block structure, the control cost is adjusted both H_2 and H_∞ norm objectives. The weighting function $W_2(s)$ is used to compromise between

the control effort and the disturbance rejection performance. Consider the weighting functions for Design-1 block

$$W_1(s) = k_1 \times \frac{s^2 + 2\omega_{nm}\varsigma_{nm} + \omega_{nm}{}^2}{s^2 + 2\omega_{dm}\varsigma_{dm} + \omega_{dm}{}^2}, \quad W_2(s) = k_2 \times \frac{s^2 + 2\omega_{nm}\varsigma_{nm} + \omega_{nm}{}^2}{s^2 + 2\omega_{dm}\varsigma_{dm} + \omega_{dm}{}^2}$$
$$W_e(s) = k_e \times \frac{\sigma}{s + \omega_e} \tag{4.6}$$

The frequency shaping filters $W_1(s)$ and $W_2(s)$ are selected in a systematic rule using multiplicative uncertainty which represents unmodeled high-frequency vibration mode dynamics in the control system model. While the filter nominator frequency ω_{nm} is taken as the controlled last vibration mode frequency, the denominator frequency ω_{dm} is selected as the first unmodeled frequency or the third vibration mode frequency. The multiplicative uncertainty $\Delta_m(j\omega)$ in the system is obtained as

$$\Delta_m(j\omega) = \frac{P_f(j\omega) - P_r(j\omega)}{P_r(j\omega)} \tag{4.7}$$

where $P_f(j\omega)$ shows the full order system model and $P_r(j\omega)$ is reduced order system model. The robust stability filter $W_1(s)$ essentially covers the unstructured uncertainties existing in the system such as

$$\left|\Delta_{\mathrm{m}}(j\omega)\right| \le \left|W_1(j\omega)\right| \qquad \forall\omega \tag{4.8}$$

Using the transfer functions obtained in equations (4.5) and (4.6), the controlled outputs with H_∞ norm objective are derived as $z_\infty^{(1)} = W_1(s)G_{p_1n}(s)$, $z_\infty^{(2)} = W_e(s)G_{p_3n}(s)$, $z_\infty^{(3)} = W_1(s)G_{p_1d}(s)$ and $z_\infty^{(4)} = W_e(s)G_{p_3d}(s)$. Also, the outputs with H_2 norm objective is obtained as $z_2^{(1)} = W_2(s)G_{p_2n}(s)$ and $z_2^{(2)} = W_2(s)G_{p_2d}(s)$. In robust control design, mixed-sensitivity approach shapes

one or more closed loop transfer functions. The objective of the Design-1 configuration is to minimize

$$\left\| \begin{bmatrix} W_e(s)\varepsilon S(s) \\ W_1(s)\varepsilon K(s)S(s) \\ W_e(s)T_c(s) \\ W_1(s)T(s) \end{bmatrix} \right\|_\infty < \gamma_0 \quad \text{and} \quad \left\| \begin{bmatrix} W_2(s)\varepsilon K(s)S(s) \\ W_2(s)T(s) \end{bmatrix} \right\|_2 < \nu_0 \tag{4.9}$$

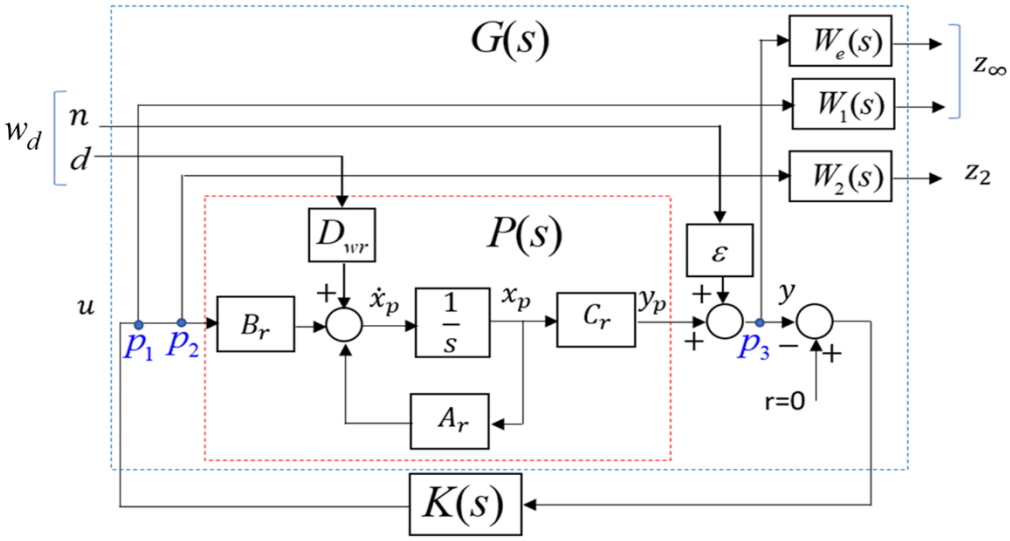

Figure 4.2: Control design block structure for Design-1.

- Design-2.

In Design-2 configuration given in Figure 4.3, the transfer functions from n to p_2 and d to p_2 differ from the Design-1.

$$\begin{aligned} G_{p_2 n}(s) &= -\varepsilon \frac{P(s)K(s)}{I + P(s)K(s)} = -\varepsilon T(s) \\ G_{p_2 d}(s) &= \frac{P(s)}{I + P(s)K(s)} = T_c(s) \end{aligned} \tag{4.10}$$

The objective is to minimize the output sensitivity and the control signal transfer functions, complementary and settling transfer function by H_∞ norm and output sensitivity, settlings transfer function by H_2 norm.

$$\left\| \begin{bmatrix} W_e(s)\varepsilon K(s)S(s) \\ W_1(s)\varepsilon T(s) \\ W_e(s)T(s) \\ W_1(s)T_c(s) \end{bmatrix} \right\|_\infty < \gamma_0 \quad \text{and} \quad \left\| \begin{bmatrix} W_2(s)\varepsilon S(s) \\ W_2(s)T_c(s) \end{bmatrix} \right\|_2 < \nu_0 \tag{4.11}$$

The weighting functions for Design-2 are selected as

$$W_1(s) = h_1 \times \frac{\sigma}{s+\omega_1}, \quad W_2(s) = h_2 \times \frac{\sigma}{s+\omega_2},$$

$$W_e(s) = h_e \times \frac{s^2 + 2\omega_{nm}\varsigma_{nm} + \omega_{nm}{}^2}{s^2 + 2\omega_{dm}\varsigma_{dm} + \omega_{dm}{}^2} \tag{4.12}$$

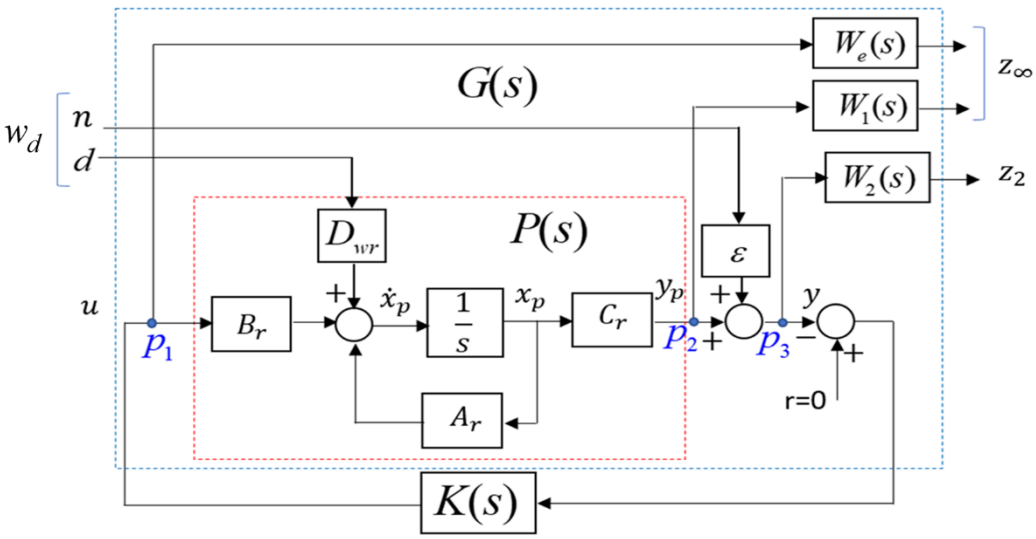

Figure 4.3: Control design block structure of Design-2

- Design-3.

Finally, Design-3 configuration shown in Figure 4.4 aims to minimize the sensitivity and control signal transfer function by H_2 norm and minimize the complementary, settling transfer function and the output sensitivity transfer function by H_∞ norm.

$$\left\| \begin{bmatrix} W_1(s)\varepsilon T(s) \\ W_e(s)\varepsilon S(s) \\ W_1(s)T_c(s) \\ W_e(s)T_c(s) \end{bmatrix} \right\|_\infty < \gamma_0 \quad \text{and} \quad \left\| \begin{bmatrix} W_2(s)\varepsilon K(s)S(s) \\ W_2(s)T(s) \end{bmatrix} \right\|_2 < \nu_0 \tag{4.13}$$

Also, the filters are given for Design-3 as follows

$$\begin{aligned} W_1(s) &= l_1 \times \frac{\sigma}{s+\omega_1}, \quad W_2(s) = l_e \times \frac{s^2 + 2\omega_{nm}\varsigma_{nm} + \omega_{nm}^{\ 2}}{s^2 + 2\omega_{dm}\varsigma_{dm} + \omega_{dm}^{\ 2}}, \\ W_e(s) &= l_e \times \frac{\sigma}{s+\omega_e} \end{aligned} \tag{4.14}$$

In Design-2 and Design-3 studies, the robust stability filters $W_2(s)$ and $W_e(s)$ are also selected using unmodeled high-frequency vibration mode dynamics as shown in Figure 4.3.

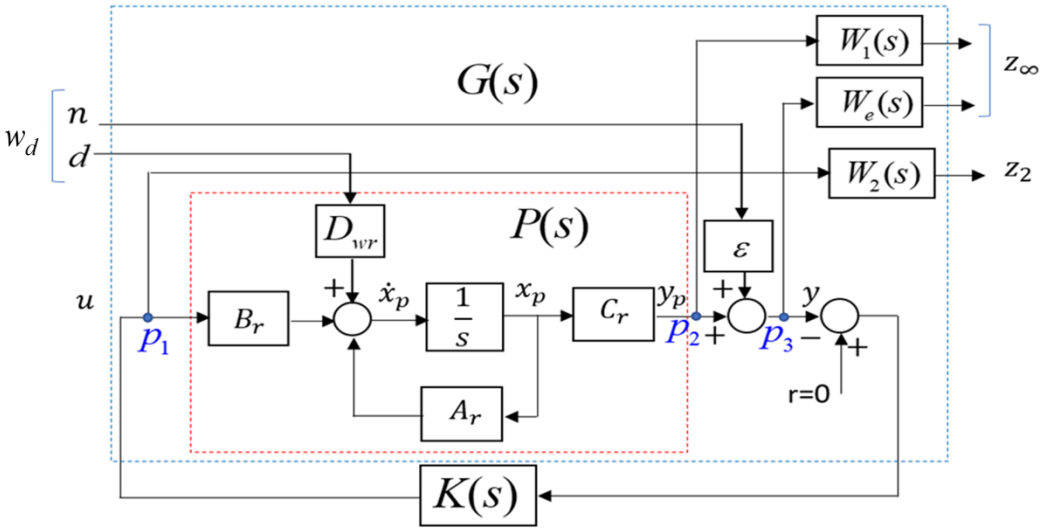

Figure 4.4: Control design block structure of Design-3.

4.3. Control Principle

To suppress the vibration of the blade element the electromagnetic actuator applies an attractive force to the MR blade according to blade position measured by

an optic sensor. In this study, the magnetic field or resulting magnetic force of the electromagnet is controlled by driving the coil current. Since only one actuator is employed, the attractive force is generated when the blade moves to downward from the nominal position. Otherwise, the electromagnet does not generate the attractive force when the blade approaches to the electromagnet. Control principle of the blade vibrations is illustrated in Figure 4.5.

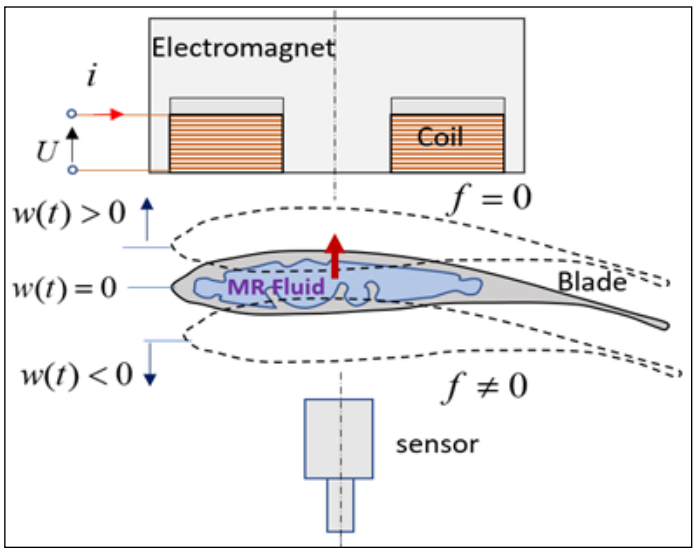

Figure 4.5: Control principle of the blade vibrations.

The frequency response characteristics of the three H_2 / H_∞ controllers are shown in Figure 4.6. The gain characteristic of Design-3 controller is different due to H_2 norm objective on control signal. The closed loop frequency responses for control cases are given in Figure 4.7.

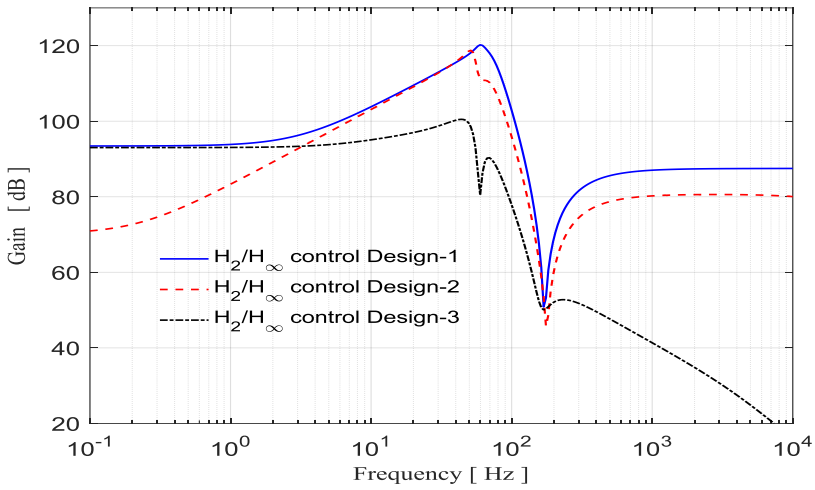

Figure 4.6. Frequency responses of the multi-objective controllers

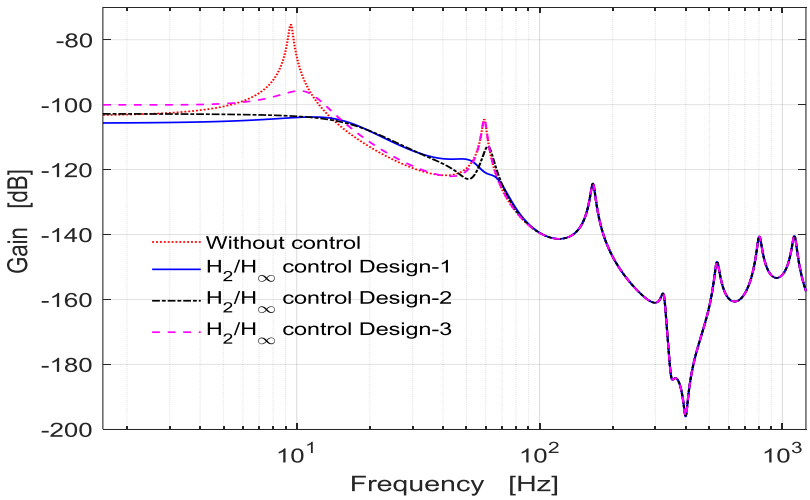

Figure 4.7. Frequency responses of the closed loop systems.

4.4. Controller Design for MR Filled Blade System

The state space models are given in equations (2.14) and (2.16) obtained for the MR filled blade system are used to have an uncertainty model $\Delta_m(s)$ in the system. The frequency shaping filters $W_1(s)$, $W_2(s)$ and $W_e(s)$ given in equation (4.8) are decided using the uncertainty model. The frequency responses of the filters and multiplicative uncertainty are shown in Figure 4.8. The multi-objective H_2 / H_∞ controller is designed using the control design block structure of Design-1 explained

in Section 4.1. The other Design-2 and Design-3 blocks-based controller designs also performed to compare the controller performances. In order to limit the content of the thesis, the results of Design-1 which provide the best performance from these three different H_2 / H_∞ controllers are presented.

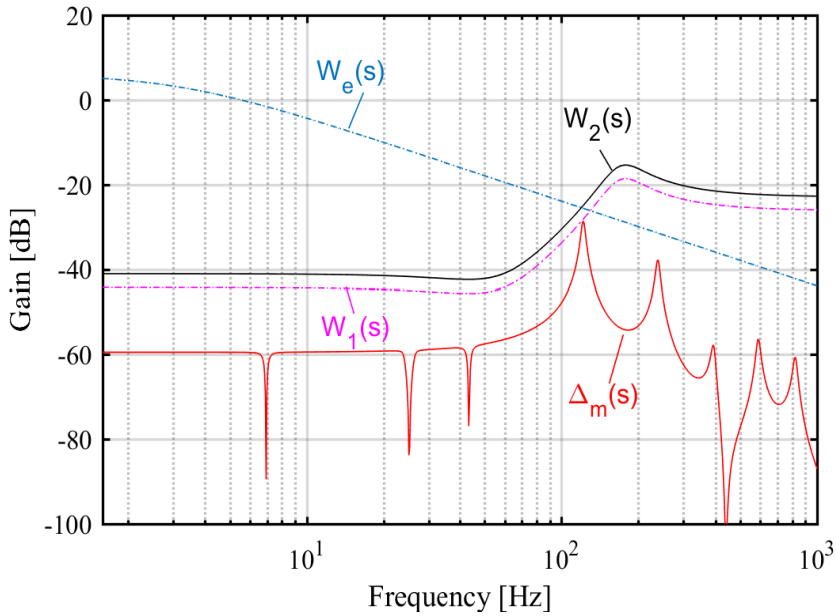

Figure 4.8: Frequency responses of the weighting filters and uncertainty.

After having an augmented system matrix using the system state space and frequency shaping filters the multi-objective H_2 / H_∞ controller is designed using *hinfmix* command in Matlab. This function performs multi-objective output-feedback synthesis and computes an LTI controller that minimizes the mixed H_2 / H_∞ norm criterion. The objective of the Design-1 is minimized as given in equation (4.9). The frequency response characteristic of the H_2 / H_∞ controller is shown in Figure 4.9(a). The closed loop frequency response is given in Figure 4.9(b).

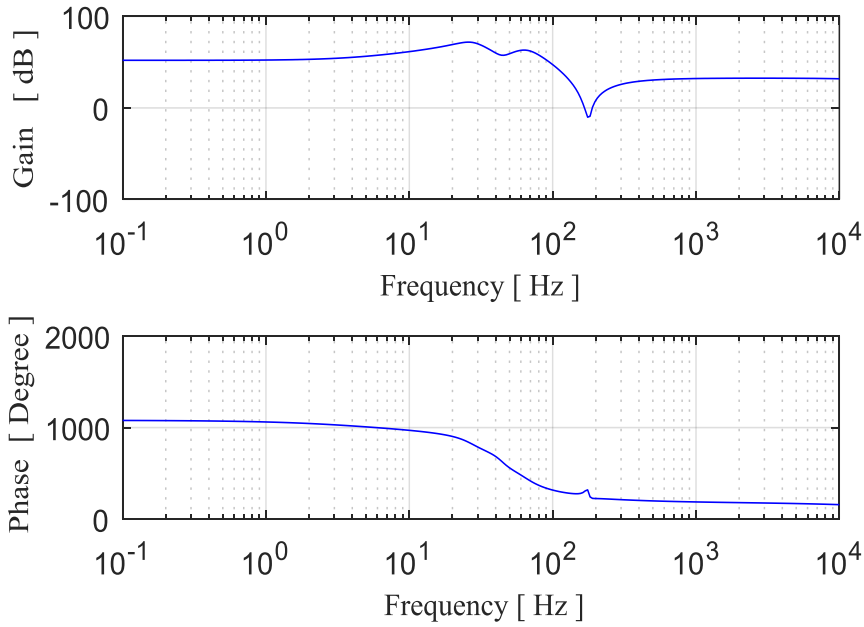

a)

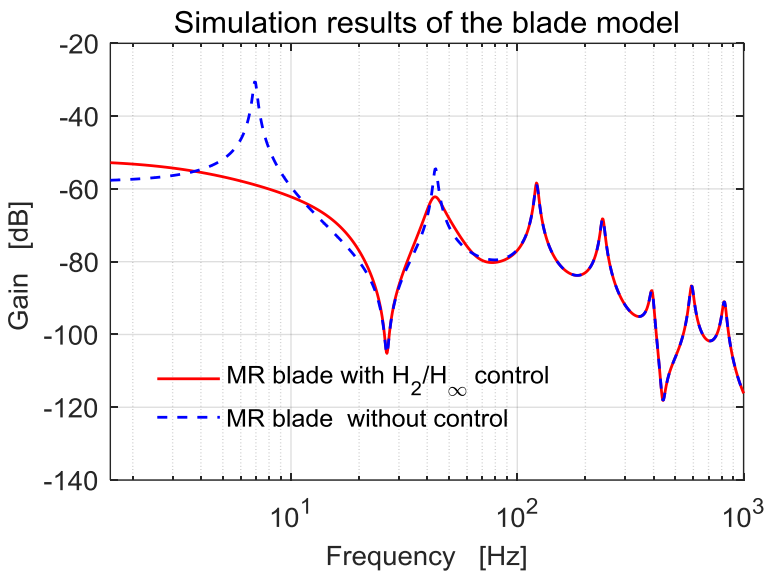

b)

Figure 4.9: Frequency responses, a) the multi-objective controller, b) the closed-loop system.

4.5. Controller Design for MR Patch Blade System

Using the similar design steps given in the previous section the multi-objective H_2 / H_∞ controller is designed for the MR patch blade system based on the control design structure Design-1. The state space models obtained in equations (2.38) and

(2.39) are used to derive uncertainty model and controller design. The mixed H_2 / H_∞ controller has the form of

$$\begin{aligned} \dot{x}_{K2\infty} &= A_{K2\infty} x_{K2\infty} + B_{K2\infty} y \\ u &= C_{K2\infty} x_{K2\infty} + D_{K2\infty} y \end{aligned} \tag{4.15}$$

The simulation results of the control design obtained for the MR Patch structure are shown in Figure 4.10-4.11.

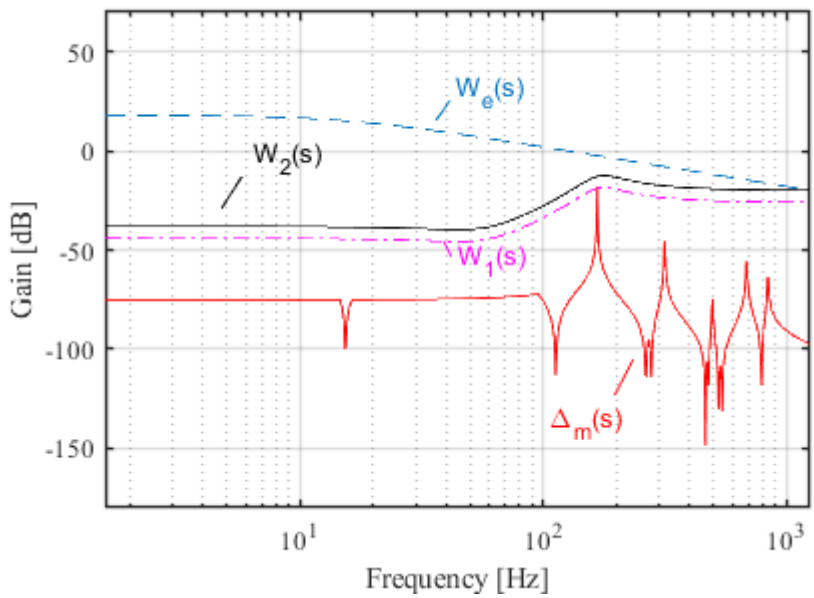

Figure 4.10: Frequency responses of the weighting filters and uncertainty.

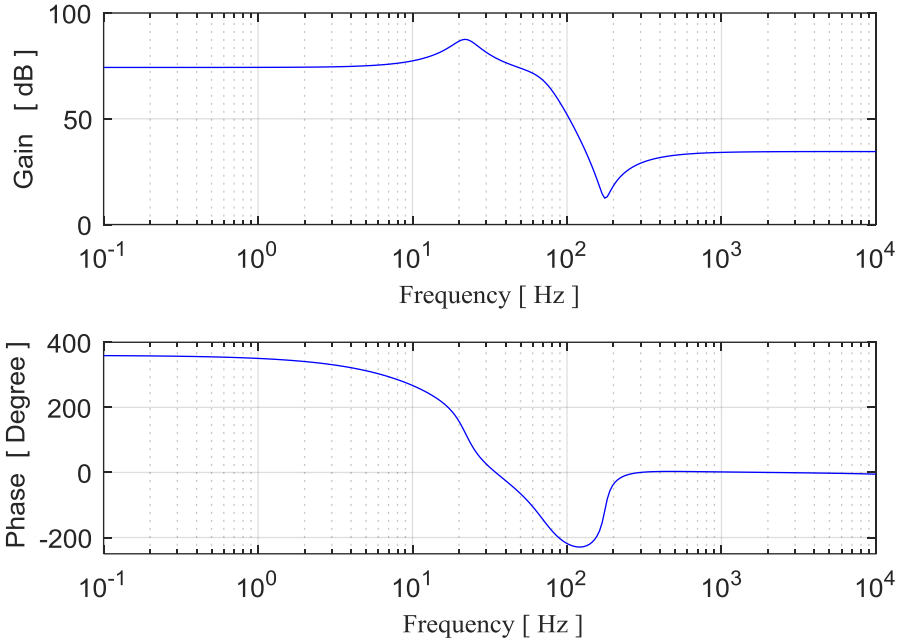

a)

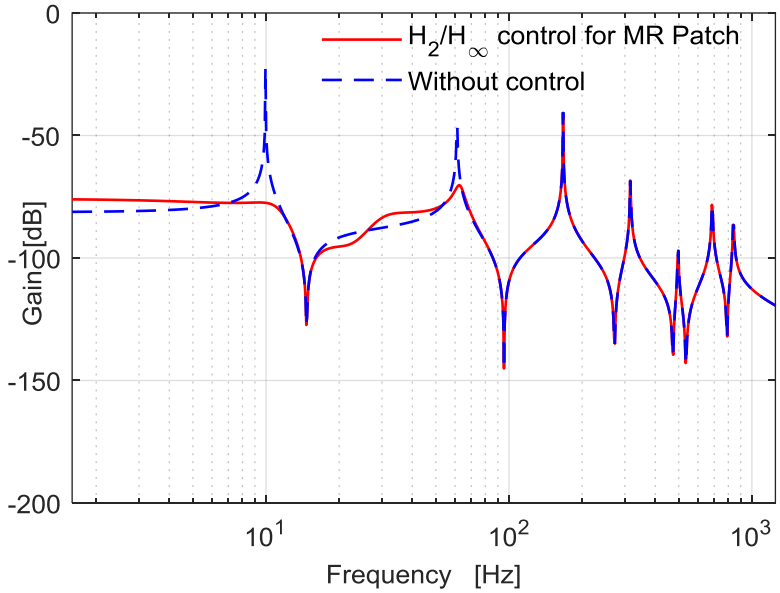

b)

Figure 4.11: Frequency responses, a) the multi-objective controller, b) the closed-loop system.

5. EXPERIMENTAL STUDY

5.1. Aerodynamic Load

To test the designed controllers under a steady state disturbance, an aerodynamic load effecting on the blade structure is generated using an air nozzle. Application of aerodynamic load to the airfoil is schematically illustrated in Figure 5.1. In wind turbines, the air current flows over the blades with a certain angle of attack. Lift and drag forces occur as the air passes over the blades. The forces are defined as

$$F_L = \frac{1}{2} C_L \rho_{air} L_N b_a v^2 \ , \ F_D = \frac{1}{2} C_D \rho_{air} L_N b_a v^2 \tag{5.1}$$

where C_L and C_D are lift and drag coefficients. Also, L_N is the air load length, b_a is the width of the blade and v is the relative wind speed. The wing is forced to bend by the effect of aerodynamic drag force F_D. The lift and drag coefficient data of the SH3055 airfoil used in the blade element of this study is given in reference [Selig and McGranahan, 2004]. Using these data, the variation of C_L and C_D with angle of attack is shown in Figure 5.2(a). The variation of the drag force with air velocity is computed for different angle of attack as shown in Figure 5.2(b).

The air nozzle used to create the aerodynamic load in the experimental setup of the blade structure is illustrated in Figure 5.3. It blows air to the end of the blade element in adjusted air speeds. In the experimental system, it is observed that the blade starts to vibrate at the angle attack of 14 degrees. The reason is that the air flow over the blade stalls around at an angle of attack of 14 degrees. When the flow over an airfoil stalls the flow separates from the surface of the airfoil and the vortex shedding creates fluctuations in the lift causing vibrations on the blade. In this study, the angle of attack of the air nozzle is set to 17.2 degrees.

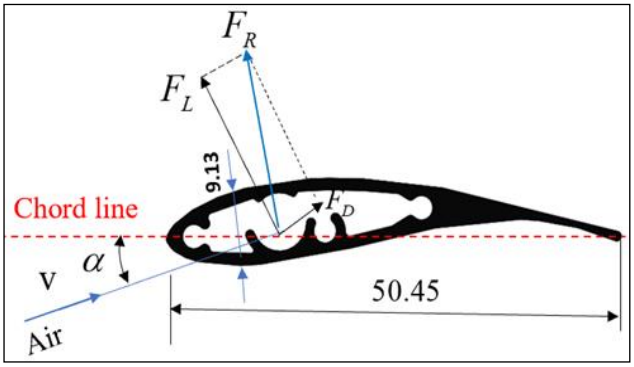

Figure 5.1: Application of aerodynamic load to the airfoil.

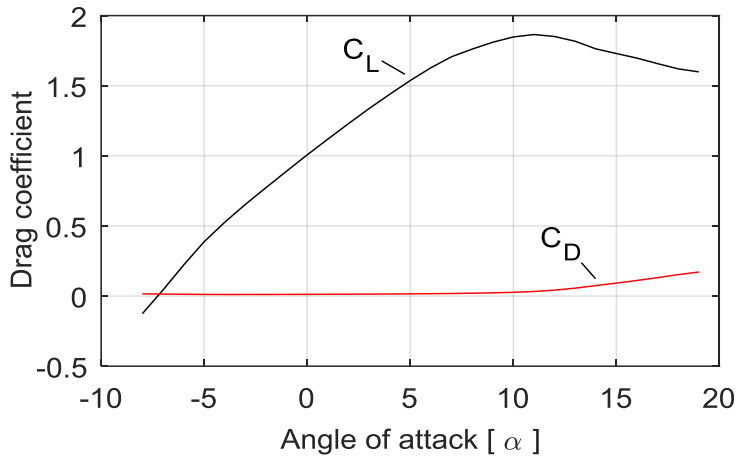

a)

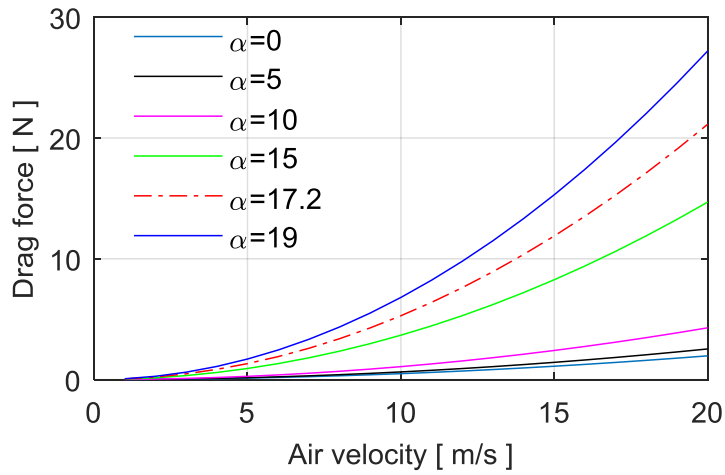

b)

Figure 5.2: Aerodynamic load characteristics, a) Lift and drag coefficients, b) Variation of the drag force with air velocity.

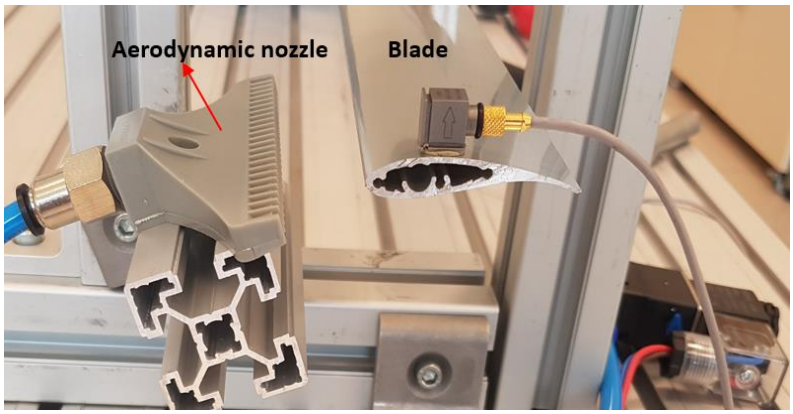

Figure 5.3: Air nozzle effecting aerodynamic load on the blade element.

A steady state vibration of the blade element is created using the air nozzle. Figure 5.4: (a)-(b) shows the vibration response of the blade profile under different angle of attack. As shown in these figures, as the angle of attack increases, the drag force increases and therefore the vibration amplitudes increase.

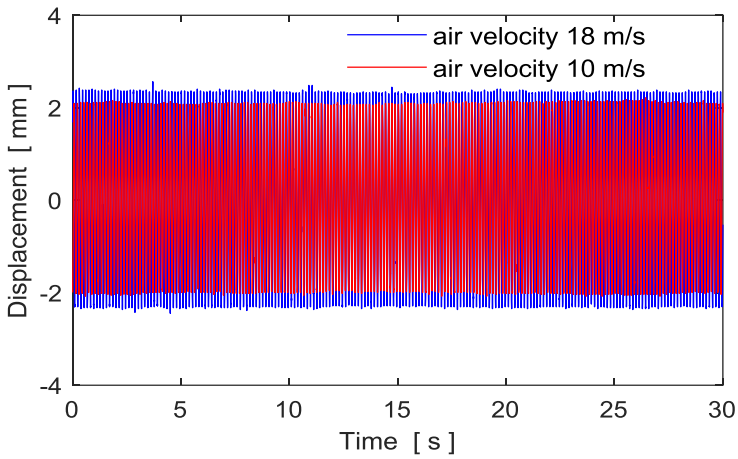

a)

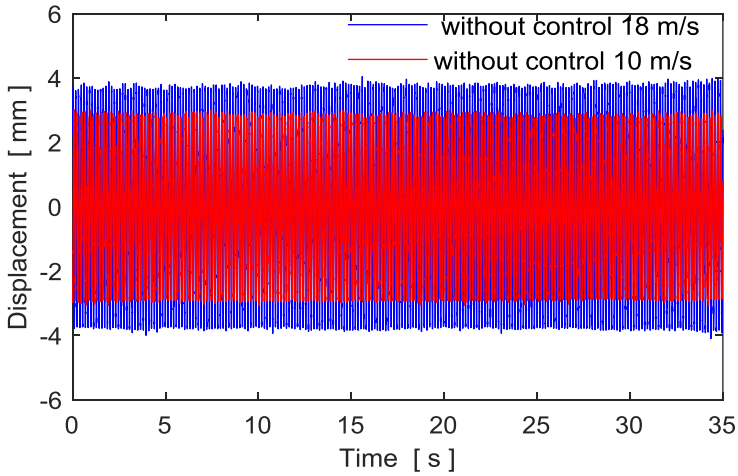

b)

Figure 5.4: Steady state response in aerodynamic load, a) angle of attack 17.2 degree, b) angle of attack 19 degree.

5.2. Active Vibration Control of the Blade with MR Layer Patch

The photo of the experimental system setup is shown in Figure 5.5. The MR patch is attached on the surface of the blade and the blade is fixed at one end using a clamp. In the experimental system, an Advanced Motion Controls MC1XAZ01 current driver with 0-17A range is used to drive the electromagnet. The displacement of the blade is measured with an optic sensor. The electromagnet resistance and inductance values are 0.7 ohm and 1.12 mH, respectively. Also, the number of coil turns is 194 and the copper wire thickness is 1 mm. Power supplies and a personal computer are used as peripheral devices. Vibration analysis of the blade is performed using a Bruel&Kjaer 3053 device.

A feedback control system structure is built to generate a control input to the electromagnetic actuator as shown schematically in Figure 5.6. The designed multi-objective controller is realized using dSpace 1104 control card. The controller is discretized and compiled in the state space form using a Matlab/Simulink file and installed on dSpace control card. According to the displacement information from the optical sensor, the controller produces an input current to the actuator through the current driver.

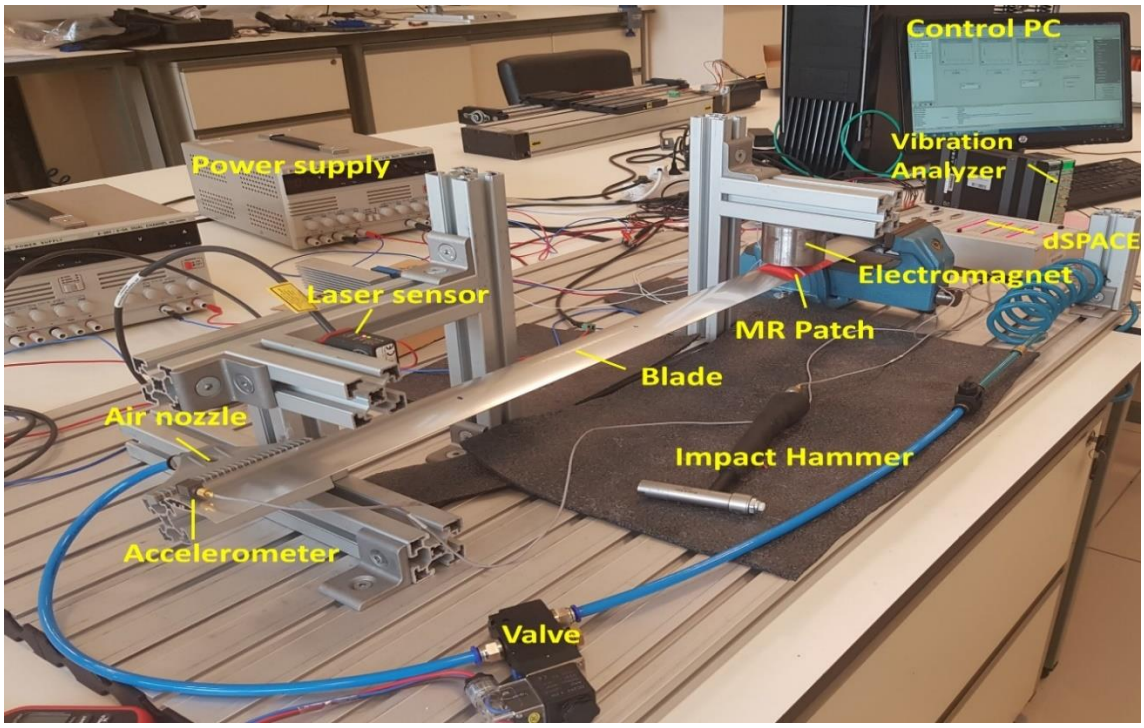

Figure 5.5: Experimental system setup.

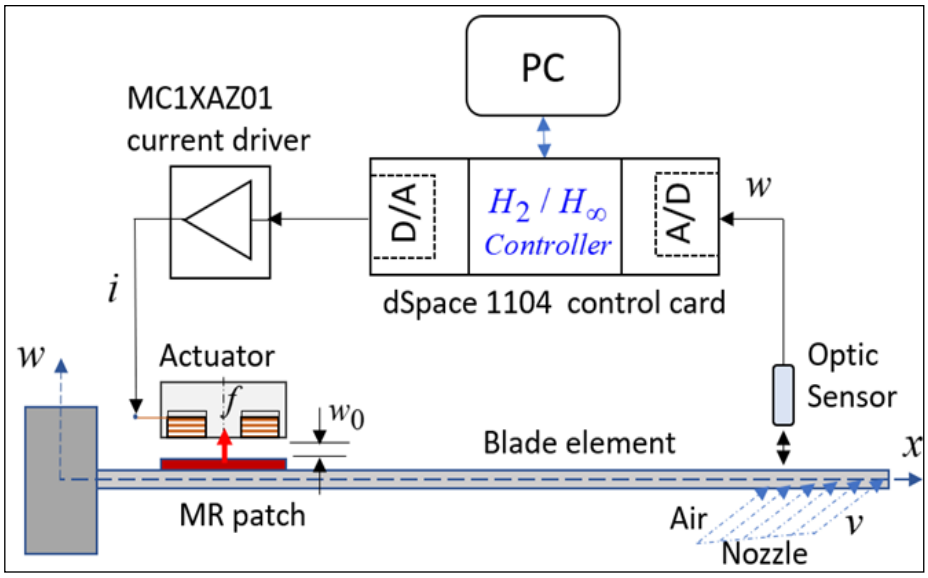

Figure 5.6: Feedback control structure.

5.2.1. Experimental Results

- Frequency domain responses

The closed-loop frequency responses of the blade element with MR patch is obtained using the vibration analysis device in experiments. The frequency responses with H_2 / H_∞ controller and without control are shown in Figure 5.7. Since the first two modes of the cantilever blade structure are considered in the control design, only these targeted modes are suppressed by the mixed norm controller. The other uncontrolled modes are not excited by the controller. This is a desired characteristic for a controller to avoid spillover effect in the distributed parameter systems. The gain reduction level in the amplitudes with control is given in Table 5.1. As seen in these results, large amount of vibration suppression is obtained in the blade element with the MR patch actuation.

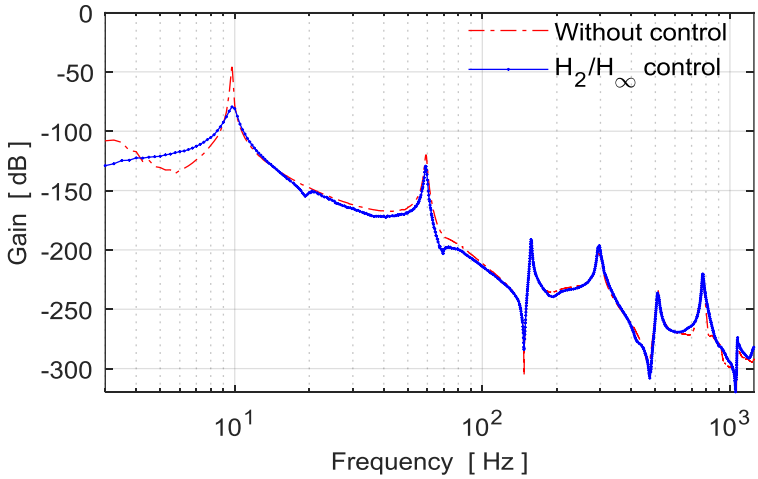

a)

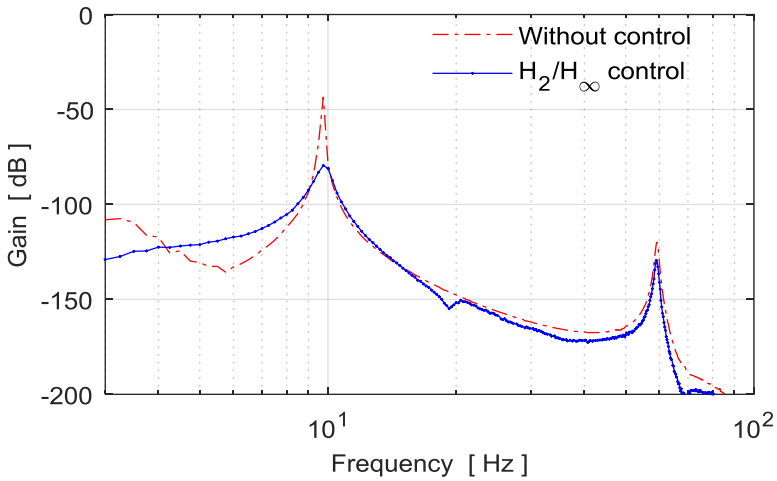

b)

Figure 5.7. Experimental frequency responses of the closed loop system, a) full system, b) first two modes

Table 5.1: Amount of reduction in gains with multi-objective controller.

Mode Number	Gain Reduction [dB]
Mode 1	36.15
Mode 2	9.67

- Time domain responses

The control system of the blade element with the MR patch actuator were tested in different conditions under the steady state aerodynamic load generated by the air nozzle. Experimental time history responses of the closed loop system for a continuous control case from a starting time is shown in Figures 5.8(a). For a detailed behavior of the blade element with and without control cases are given in Figure 5.8(b). Moreover, the repeated controlled tests are realized to understand the

response characteristics of the controllers as given in Figures 5.9. The control inputs obtained in the experiments are shown in Figures 5.10(a-b) for the continuous and repeated control tests.

A robustness test was also performed in the case of parameter variation by attaching an extra mass on the surface of the blade. The results are shown in Figure 5.11 when an additional mass of 12% of the blade mass is added. The feedback control systems of the blade element with MR patch are quite robust against parameter uncertainty and vibration attenuation level with additional tip mass are still very large. The force applied to the MR patch is shown in Figure 5.12.

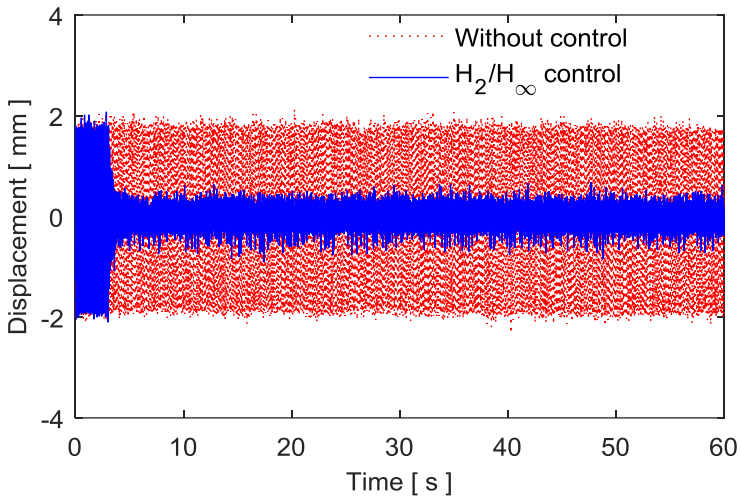

a)

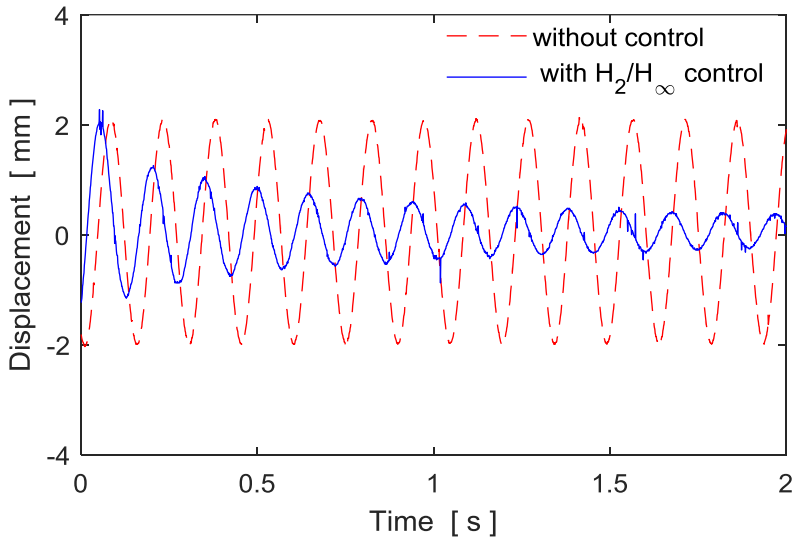

b)

Figure 5.8: Experimental results of the closed loop system with steady state aerodynamic load, a) continuous control, b) vibration of the blade element in small scale time range.

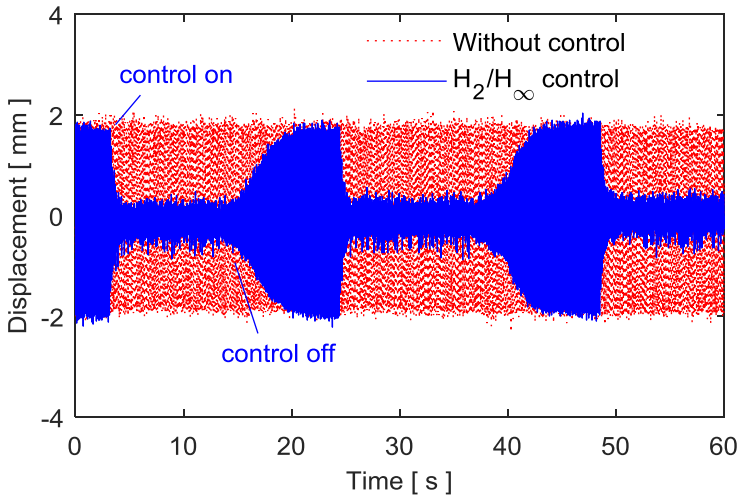

Figure 5.9: Experimental results of the closed loop system for repeated control with steady state aerodynamic load.

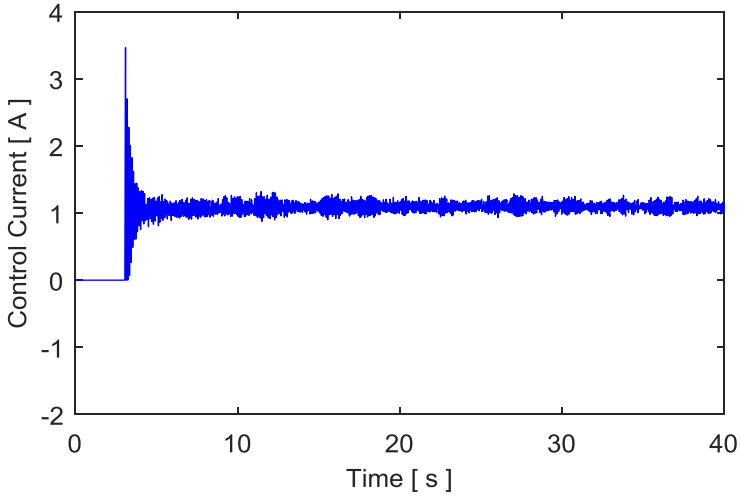

a)

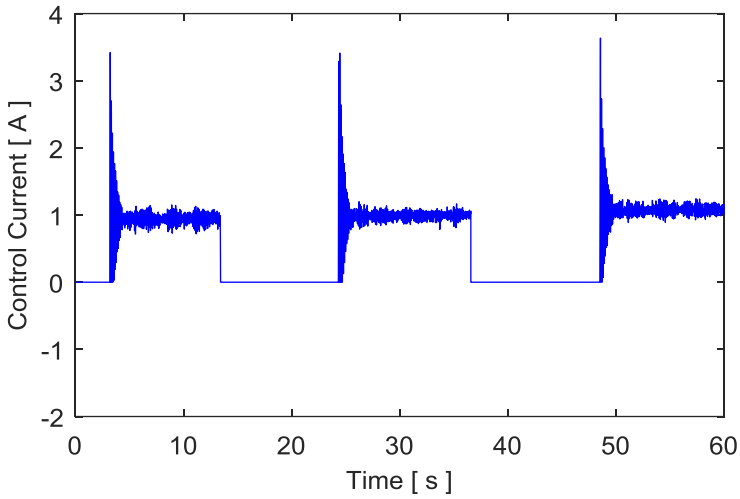

(b)

Figure 5.10: Experimental control inputs, a) continuous control, b) repeated control.

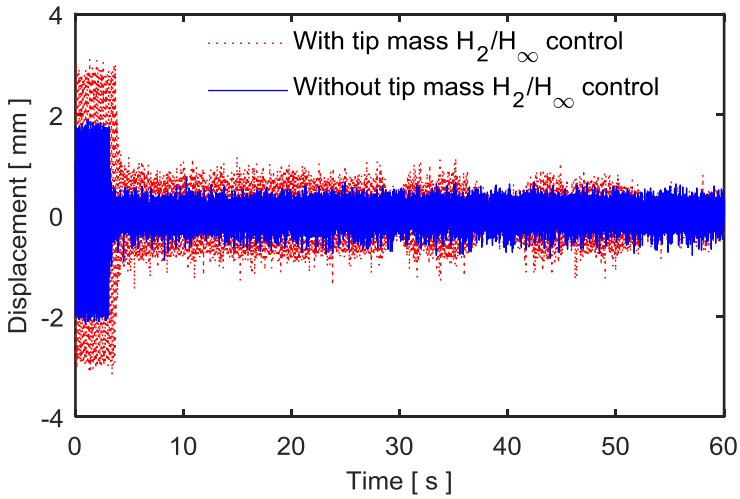

Figure 5.11: Robustness test results for additional mass.

5.3. Active Vibration Control using PZT Patch Actuator

In literature, active vibration control of flexible structural systems has been studied by many researchers using piezoelectric patch actuator. To understand the control effectiveness of the proposed MR patch and compare the MR patch results with respect to vibration suppression, a PZT patch-based control study is also performed. The attached PZT patch (Figure 5.12) has almost same dimensions with the MR patch and parameters of the PZT patch is given in Table5.2.

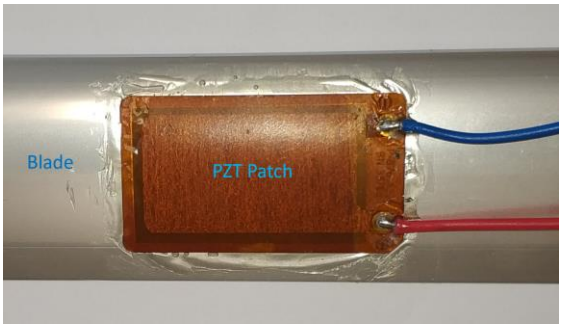

Figure 5.12: PZT patch actuator.

5.3.1. PZT Force Model

The actuation principle of the MR and PZT patches are completely different. To compare performances of the MR and PZT patches according to vibration

attenuation results the force equation of PZT should also be derived. The derivation of force equation for a PZT patch actuator is presented in many references. The parameters of the PZT layer for a modeling and control design study is shown in Figure 5.13. In general, the bending moment generated by a PZT patch attached on a beam is defined as

$$M_p = -e_{31} V_p b_p z_m \quad , \tag{5.2}$$

where V_p is the applied voltage, z_m is the distance from the half thickness of the blade to the half thickness of the PZT. In addition, b_p shows the width of the PZT and e_{31} shows the PZT patch constant. The force applied by PZT actuator is derived as follows

$$f_a(t) = \frac{M_p(t)}{I_i}\left[\psi_n'(l_i)\right] = \frac{-d_{31}E_p b_p\left(\frac{h_b + h_p}{2}\right)V_p}{\rho_b A_b L_b^3 + \rho_p A_p L_p^3}\left[\psi_n'(l_2) - \psi_n'(l_1)\right]$$

$$S_p = -\frac{d_{31}E_p b_p\left(\frac{h_b}{2} + \frac{h_p}{2}\right)}{\rho_b A_b L_b^3 + \rho_p A_p L_p^3} \tag{5.3}$$

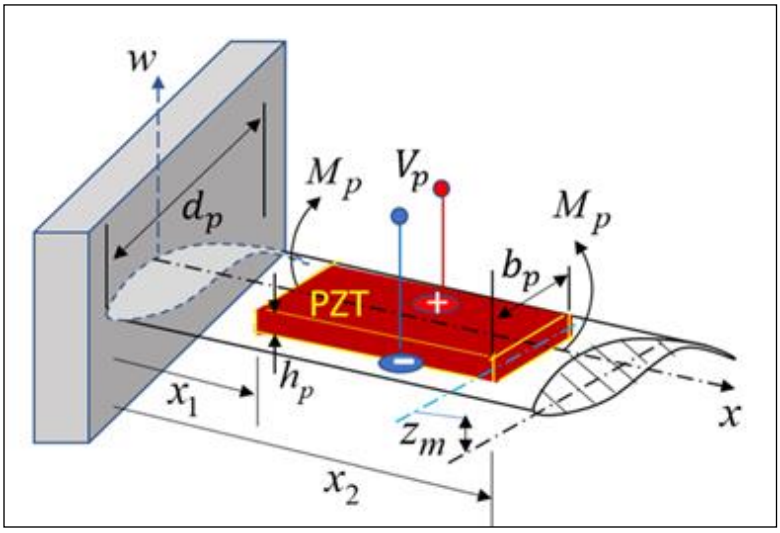

Figure 5.13: PZT patch layout and parameters.

5.3.2. State Space Model

The layout of the same cantilever blade structure with PZT layer for control design study is shown in Figure 5.14. Here x coordinate is related with the longitudinal dynamics and w coordinate shows the direction of vibration of the blade. The piezoelectric patch is located on the blade surface between l_1 and l_2 distances. The aerodynamic load effects at the end of the blade between a_1 and a_2 distances. The distance x_s denotes the sensor location.

For each vibration mode of the cantilever blade element, the separated equation of motion is given by

$$\ddot{q}_n(t) + 2\varsigma\omega_n\dot{q}_n(t) + \omega_n^2 q_n(t) = f_a(t)u(t) + f_d(t)d(t) \tag{5.4}$$

where ω_n is the mode natural frequency, ς is the damping coefficient. The state space equation for each modal behavior is obtained using equation (5.2) as follows

$$\begin{aligned} \dot{\bar{x}}_n(t) &= A_n\bar{x}_n(t) + B_n u(t) + D_{wn}d(t) \\ y_n &= C\,\bar{x}_n(t) = \begin{bmatrix} C_n & 0 \end{bmatrix}\bar{x}_n(t) \end{aligned} \tag{5.5}$$

where $\bar{x}_n(t)$ is the state vector, A_n is the system matrix, B_n is the control input matrix and $u(t)$ is the control input. The matrix C_n is computed using mode shape function.

The structure of the state vector and matrices are as follows

$$\bar{x}_n = \begin{bmatrix} x_n(t) \\ \dot{x}_n(t) \end{bmatrix}, A_n = \begin{bmatrix} 0 & 1 \\ -\omega_n^2 & -2\varsigma\omega_n \end{bmatrix}, B_n = \begin{bmatrix} 0 \\ \psi_n(x_a) \end{bmatrix}, D_{wn} = \begin{bmatrix} 0 \\ \psi_n(x_d) \end{bmatrix} \tag{5.6}$$

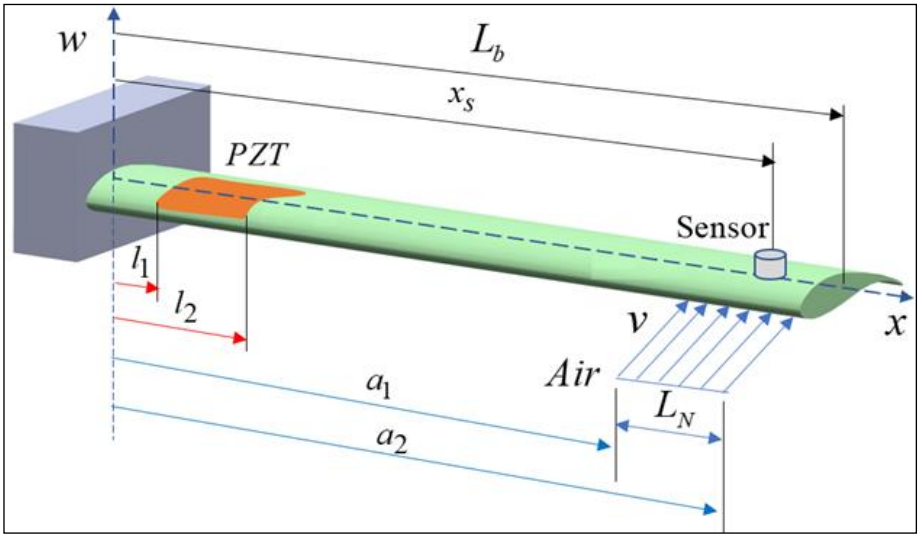

Figure 5.14: Layout of the cantilever blade.

If the modeling is extended for N modes ($n = 1, \ldots, N$), the state space structure is obtained as follows.

$$\dot{x}_f = \begin{bmatrix} \dot{\bar{x}}_1 \\ \dot{\bar{x}}_2 \\ \vdots \\ \dot{\bar{x}}_N \end{bmatrix} = \begin{bmatrix} A_1 & & & 0 \\ & A_2 & & \\ & & \ddots & \\ 0 & & & A_N \end{bmatrix} \begin{bmatrix} \bar{x}_1 \\ \bar{x}_2 \\ \vdots \\ \bar{x}_N \end{bmatrix} + \begin{bmatrix} B_1 \\ B_2 \\ \vdots \\ B_N \end{bmatrix} u + \begin{bmatrix} D_{w1} \\ D_{w2} \\ \vdots \\ D_{wN} \end{bmatrix} d$$

$$y_f = \begin{bmatrix} C_1 & C_2 & \ldots & C_N \end{bmatrix} \begin{bmatrix} \bar{x}_1 \\ \bar{x}_2 \\ \vdots \\ \bar{x}_N \end{bmatrix} \tag{5.7}$$

A reduced order state space model for the control design study can be obtained by considering the first two modes of equation (5.7). The reduced order state space equation is written as

$$\begin{aligned} \dot{x}_r(t) &= A_r x_r(t) + B_r u(t) + D_{wr} d(t) \\ y_r(t) &= C_r x_r(t) \end{aligned} \tag{5.8}$$

Table 5.2: Parameters of the cantilever blade and PZT patch.

Symbol	Meaning	Value	Unit
L_b	Length of the blade	0.8	m
b_b	Width of the blade	0.035	m
h_b	Thickness of the beam	0.0074	m
ρ_b	Density of the beam	2780	kg/m^3
E_b	Young's modulus of the beam	70	GPa
L_p	Length of the PZT patch	0.050	m
b_p	Width of the PZT patch	0.030	m
h_p	Thickness of the PZT patch	0.0005	m
d_{31}	Piezoelectric charge constant	-1.8×10^{-10}	C/N
ρ_p	Density of the PZT patch	7800	kg/m^3
E_p	Young's modulus of the PZT patch	6.2	GPa

5.3.3. Controller Design

To compare the PZT patch results with MR patch an equal control design condition is satisfied. A multi-objective H_2 / H_∞ controller is designed using the design block Design-1.

5.3.4. Experimental System

The photo of the experimental system setup for PZT patch is shown in Figure 5.15. The piezoelectric patch is attached on the surface of the blade and the blade is fixed at one end using a clamp. In the PZT based experimental system, a PI DuraAct (P-876.A12) PZT patch with $61\times35\times0.5$ mm dimension and a piezo driver (E-413.D2) are used. Supply voltage for the PZT patch is between -100 $+400$ V. The designed multi-objective controller is realized using dSpace 1104 control card. The controller is discretized and compiled in the state space form using a Matlab/Simulink file and installed on dSpace control card.

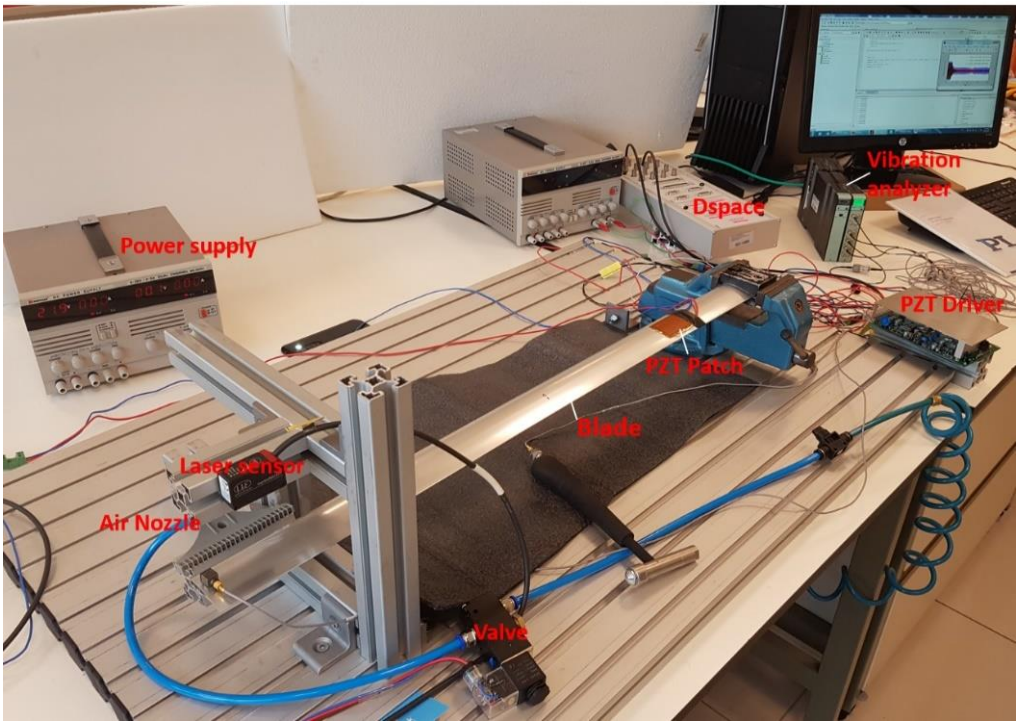

Figure 5.15: Experimental system setup blade with PZT patch.

- Experimental Results

The closed loop frequency responses of the blade with PZT patch actuator is obtained using the vibration analysis device in experiments. The frequency responses obtained with H_2 / H_∞ controller is shown in Figure 5.16 respectively. Since the first two modes of the cantilever blade structure are considered in the control design, the targeted modes are only suppressed by the controller. The other uncontrolled modes are not excited by the controller. This is a desired characteristic for a controller to avoid spillover effect in the distributed parameter systems. The reduction level in the amplitudes of the gains is given in Table 5.3

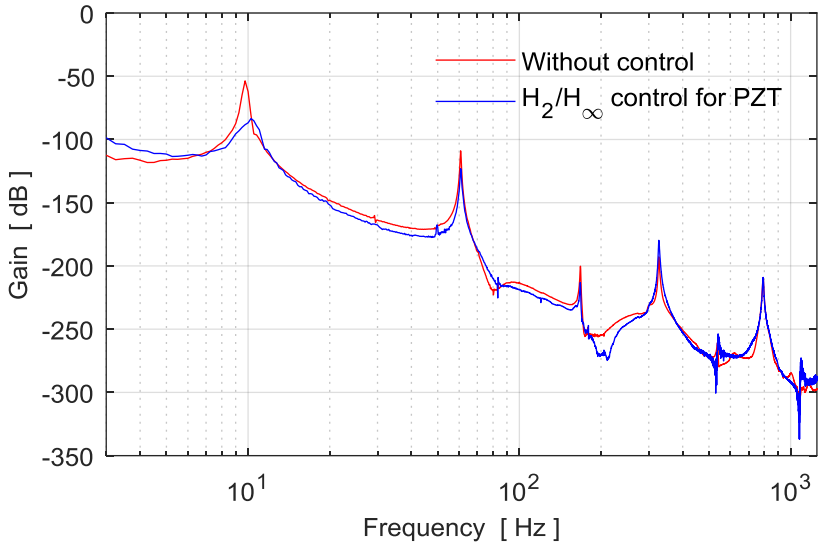

(a)

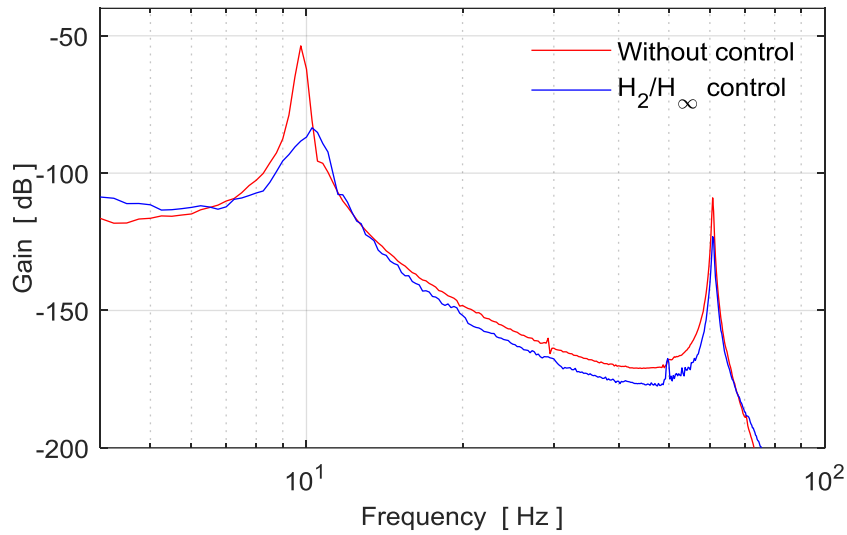

(b)

Figure 5.16: Experimental frequency responses of the closed loop system, a) full system, b) first two modes

Table 5.3: Amount of reduction in gains with multi-objective controller.

Mode Number	MR Patch	PZT Patch
1.mode	36.15	29.82
2.mode	9.67	14.19

The designed multi-objective controller for the PZT patch actuator is tested in different conditions under the steady state aerodynamic load generated by the air nozzle. Experimental time history responses of the closed loop system for a continuous control case from a starting time are shown in Figures 5.17. Moreover, the repeated controlled and uncontrolled tests are realized to understand the response

characteristics of the controllers as given in Figures 5.18. As seen in the time history responses, the blade with PZT patch actuator shows significant results to attenuate vibrations of the blade. The control input is shown in Figures 5.19 for repeated control tests.

A robustness test is also performed in the case of parameter variation by attaching an extra mass on the surface of the blade. The results are shown in Figure 5.20 when an additional mass of 12% of the blade mass is added. The feedback control systems are quite robust against parameter uncertainty and vibration attenuation with additional mass.

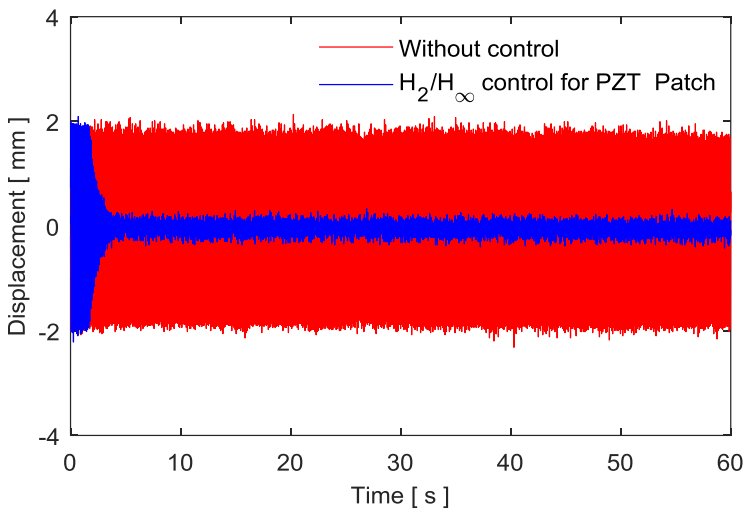

Figure 5.17: Experimental results of the closed loop system with steady state aerodynamic load.

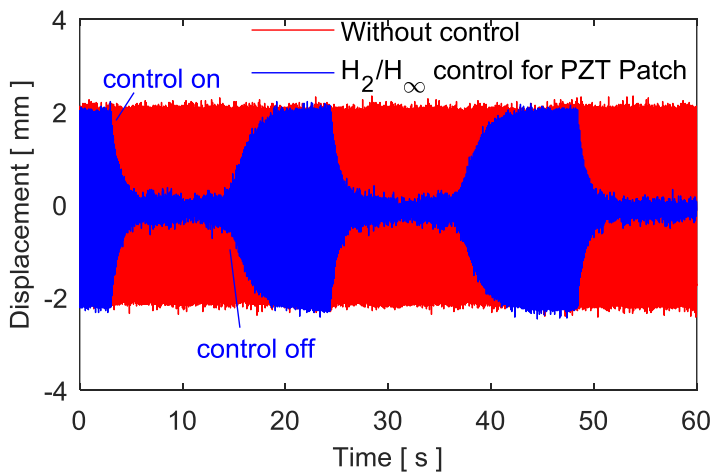

Figure 5.18: Experimental results of the repeated controlled and uncontrolled blade vibrations

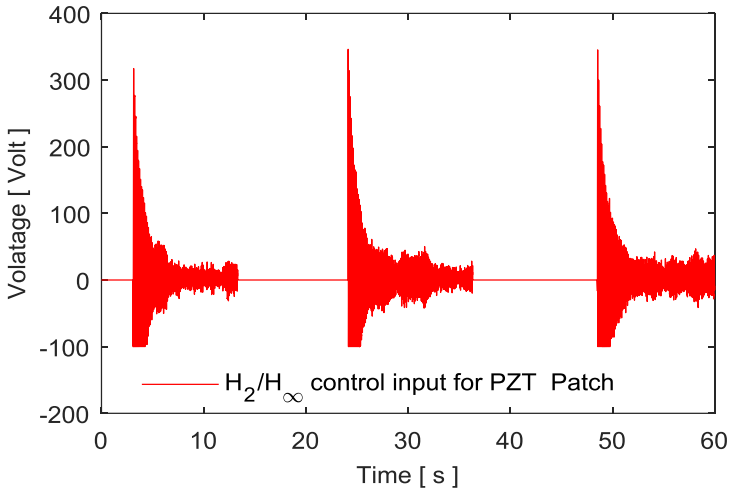

Figure 5.19: Experimental control inputs

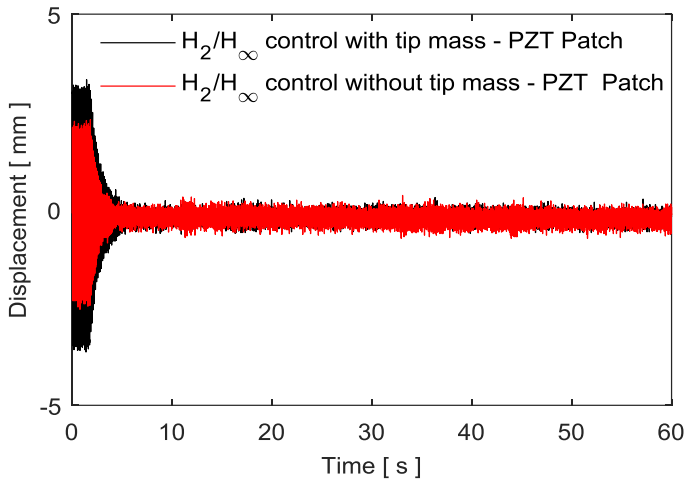

Figure 5.20: Robustness test results for additional mass.

5.4. Power Consumption Analysis

Active vibration control of the flexible blade element using MR layer patch and PZT patch were presented in Section 5.2 and 5.3 respectively. Both patch actuators suppress the blade vibrations effectively. To compare control performances of the MR patch and PZT patch results power consumption of the both methods should be considered. In the MR patch case, the control force is generated by driving the current of the electromagnet. Therefore, the amount of consumed power by the electromagnet can be computed as

$$P_{MR} = I^2 R \tag{5.9}$$

where R is the self-resistance value of the electromagnet and $I = i_0 + i_c$ is the total current of the electromagnet.

In the PZT patch case, the control force is generated by driving the voltage of the piezoelectric patch. The amount of power is calculated using the following equation

$$P_{PZT} = \pi \omega C V^2 \tag{5.10}$$

where C denotes the electrical capacitance value of the piezoelectric material, ω is the frequency (cycles of per second) and V is the control voltage applied by the piezoelectric driver.

Using the experimental control results for a period of 30 second repeated control case, power consumptions of the patch actuators were computed. Figure 5.21 shows the instantaneous power consumption value calculated using the control current of the MR patch structure. Figure 5.22 illustrates the amount of instantaneous power consumption value calculated using the control voltage in the case of PZT patch. Comparation of the both consumed powers of patch actuator are given in Figure 5.23 and Table 5.4.

As seen in the power consumption results, PZT patch consumes less energy compared to MR patch. This is the advantage of the distributed actuation of the PZT patch. The reason of the higher power consumption of the MR patch comes from the electromagnetic force characteristics. If control forces compared for both cases it is actually seen same level of amplitudes. The electromagnetic force equation (3.1) is proportional to the square of the current but inversely proportional to the square of the gap. Since PZT patch is attached on the surface of the blade element it is actually the gap is zero. If the gap between the electromagnet and blade decreases the power consumption of the electromagnet also becomes less because much smaller current will be needed to generate the same amplitude of force with PZT. In practice the gap is set to 1 mm to prevent the vibrating blade striking the electromagnet. On the other hand, to generate large forces using PZT patch needs very high control voltages and expensive driver units. For large system applications, the MR patch will have some advantages because the electromagnets may generate large forces with less costs.

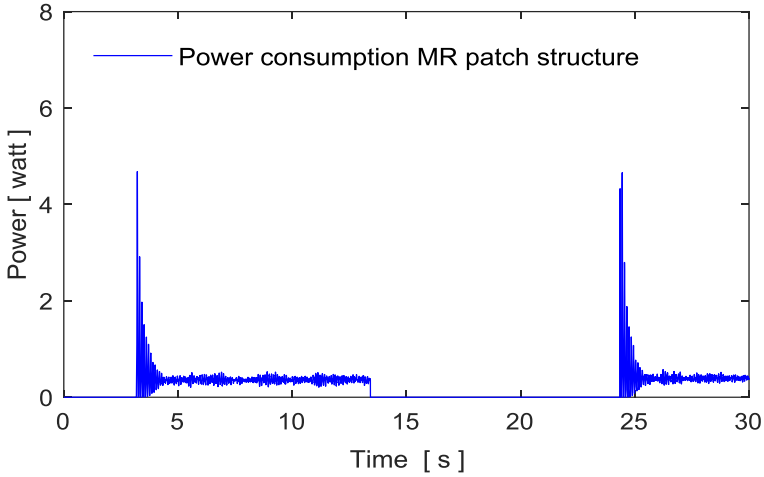

Figure 5.21: Instantaneous power consumption of the MR patch structure.

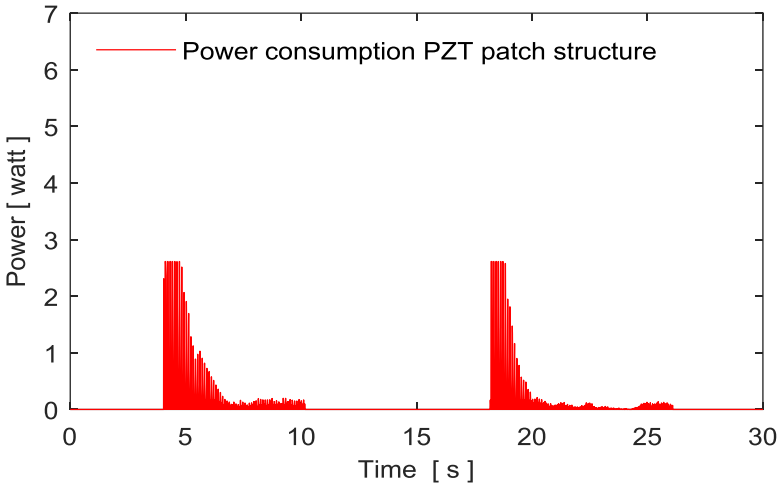

Figure 5.22: Instantaneous power consumption of the PZT patch.

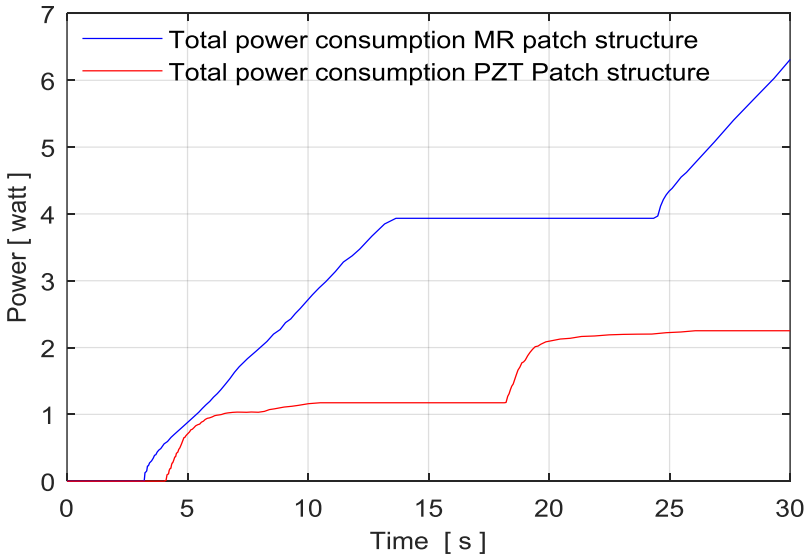

Figure 5.23: Total power consumption for both patch actuator structures.

Table 5.4: Total power consumption results.

Proposed Control Structures	MR Patch Structure	Piezoelectric Patch
Total Power Consumption (Watt)	6.31	2.26

5.5. Active Vibration Control of the Blade Containing MR Fluid

The experimental study is repeated for the MR filled blade element using the multi-objective controller. The photo of the experimental system setup for active control is shown in Figure 5.24. The same setup peripheral devices, current driver and optical sensor are used. The control implementation is also realized using dSpace control card.

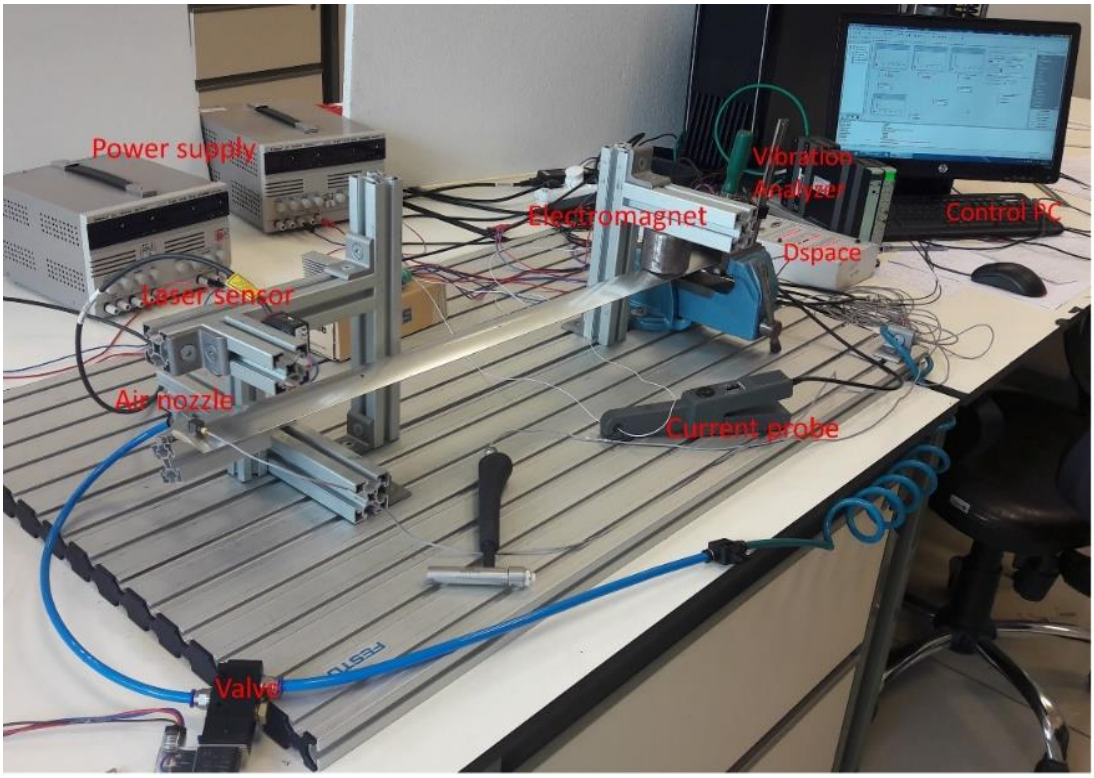

Figure 5.24: Experimental system setup.

5.5.1. Experimental Results

The experimental closed loop frequency responses of the MR filled blade element with H_2 / H_∞ controller is shown in Figure 5.25. Since the first two modes of the cantilever blade are targeted in control design, these modes are suppressed by the controller in different levels of gains as shown in Table 5.25(b).

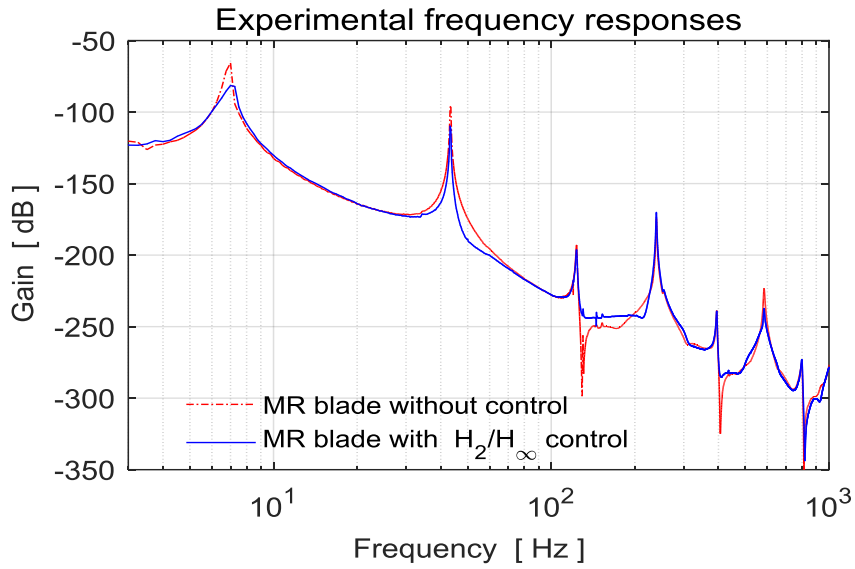

a)

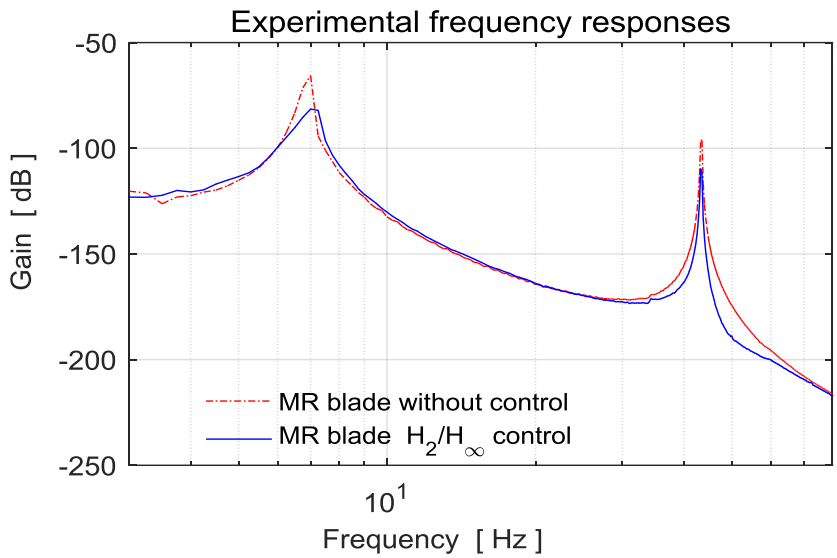

b)

Figure 5.25: Experimental frequency responses of the closed loop, a) all modes, b) first two modes.

Table 5.5: Amount of reduction in gains with H_2 / H_∞ controller.

Mode Number	Gain Reduction [dB]
1.mode	15.83
2.mode	13.07

The designed multi-objective controller is tested in different conditions under the steady state aerodynamic load. Experimental time history responses of the closed loop system for a continuous control case from a starting time are shown in Figure 5.26(a). Moreover, the repeated controlled and uncontrolled tests are realized to understand the response characteristics of the controllers as given in Figure 5.26(b).

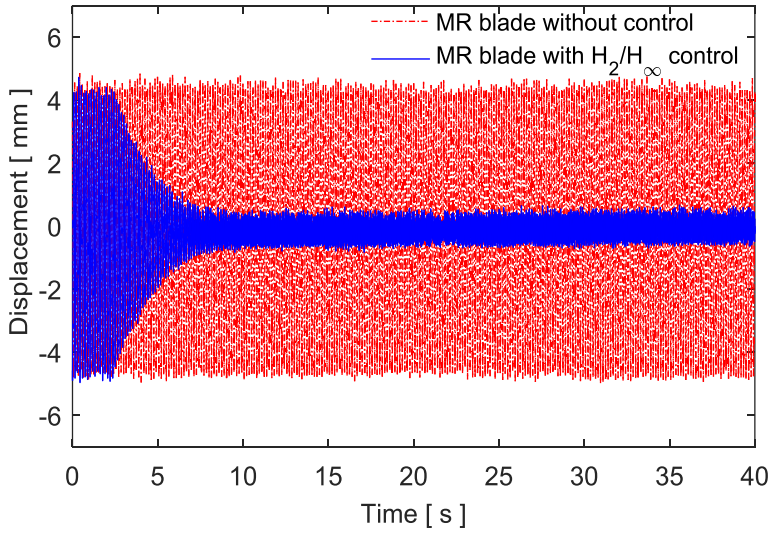

(a)

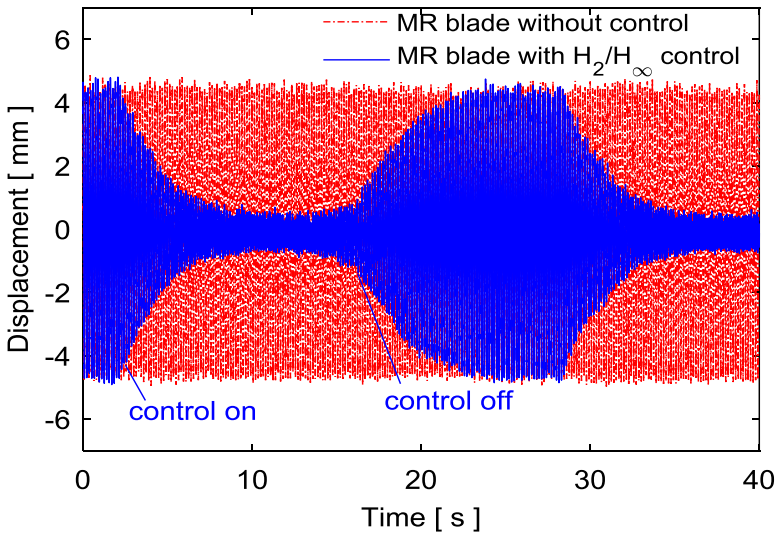

(b)

Figure 5.26: Experimental results of the closed loop system under steady state aerodynamic load, a) continuous control, b) repeated control

The control inputs are shown in Figure 5.27 for the control case of Figure 5.26. Moreover, a robustness test is performed in the case of parameter variation by attaching an extra mass on the surface of the blade. The results are shown in Figure 5.28 when an additional mass of 12% of the blade mass is added. The control system is quite robust against parameter uncertainty and vibration attenuation with additional mass.

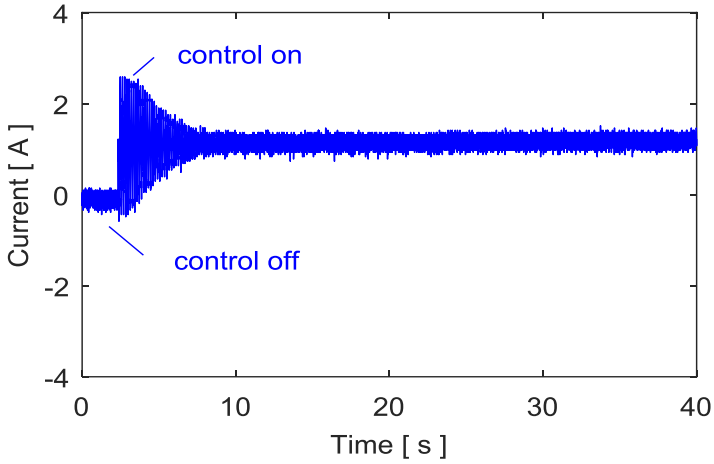

a)

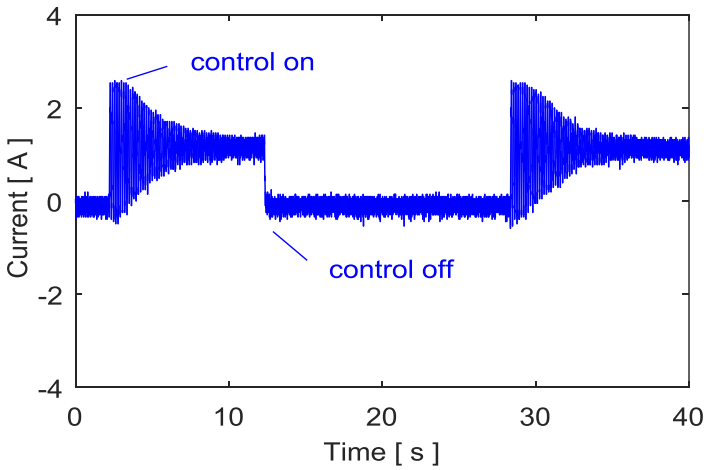

b)

Figure 5.27: Experimental control inputs, a) continuous control, b) repeated control.

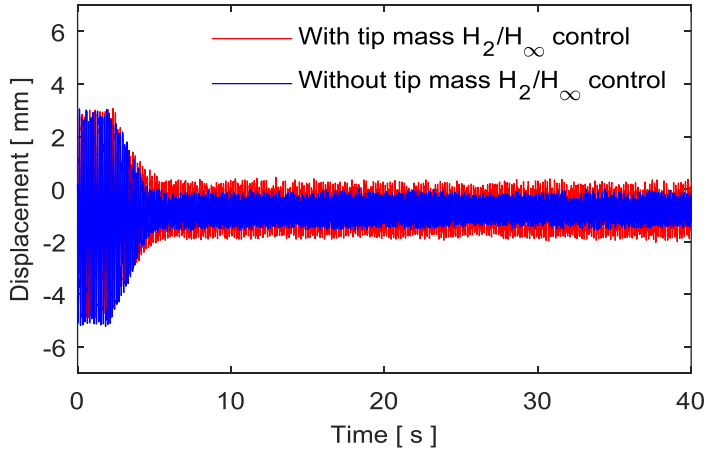

a)

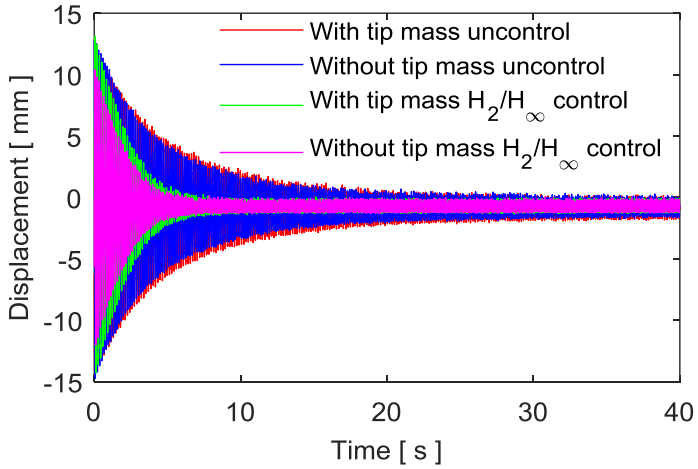

b)

Figure 5.28: Robustness test results for an additional mass, a) steady state case, b) reference point case.

5.6. Switching Control

In the previous control applications, the model-based controller produces the control signal as if there were two mutually operating electromagnets in the system. This means that the controller designed using the state space model of the blade may generate the control input $u = i_c$ and $u = -i_c$ depend on the blade displacement. There is actually only one electromagnet and negative current is for an electromagnet that does not exist in the system. Therefore, only positive current can be applied in the blade control system. In this section, an algorithm is developed to realize a switching control that only gives positive current.

5.6.1. Single-sided Actuation Principle

In the proposed control system, there is only one electromagnet to apply the attractive force when the blade moves to downward from the nominal position. On the other hand, the electromagnet does not apply any force when the blade approaches to the electromagnet. Therefore, a single-sided control actuation exists to suppress the blade vibrations. A detailed illustration of the control structure is depicted in Figure 5.29.

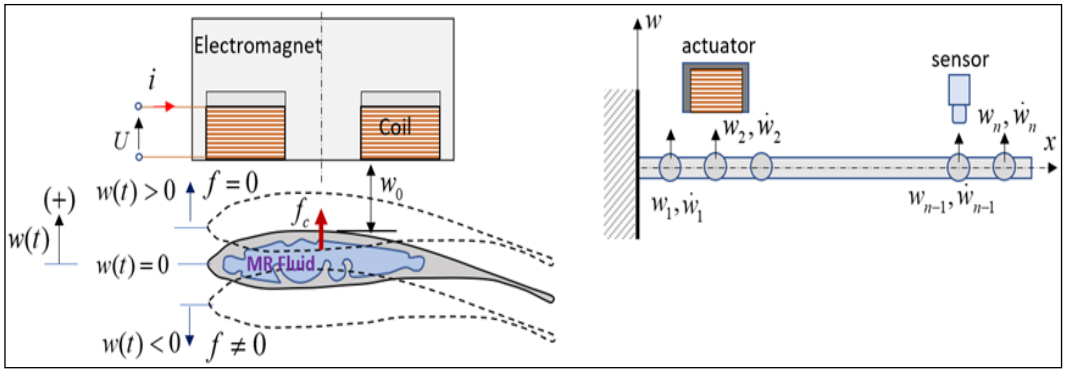

(a) (b)

Figure 5.29: The principle of electromagnetic actuation, a) front view, b) longitudinal view.

5.6.2. Positive Current Algorithm

An algorithm that generates a positive control current can be obtained depending on the blade state variables. We assume that a controller computes the controller current with respect to state variables such as $i_c = \mathcal{K}(w(t), \dot{w}(t))$. For the positive state variables of the blade element, the algorithm is given as

$$if \quad w(t) \geq 0 \text{ and } \dot{w}(t) \geq 0 \quad \text{then} \quad i = i_c = 0, \quad f = f_c = 0 \tag{5.9}$$

$$if \quad w(t) \geq 0 \text{ and } \dot{w}(t) < 0 \quad \text{then} \quad \begin{cases} i_c > 0 & i = i_c & f = f_c \\ i_c \leq 0 & i = 0 & f = 0 \end{cases} \tag{5.11}$$

where f_c is the control force. Similarly, the positiveness of the current is maintained for the negative state variables of the blade as follow.

$$if \quad w(t) < 0 \quad \text{and} \quad \dot{w}(t) < 0 \quad \text{then} \quad i = i_c, \quad f = f_c \tag{5.12}$$

$$if \quad w(t) \leq 0 \quad \text{and} \quad \dot{w}(t) > 0 \quad \text{then} \quad \begin{cases} i_c > 0 & i = i_c & f = f_c \\ i_c \leq 0 & i = 0 & f = 0 \end{cases} \tag{5.13}$$

5.6.3. LQG Control Design

LQG control is a modern control design method and it is a combination of optimal control (LQR) with the optimal state estimation (Kalman filter). Positiveness of the control current defined in Section 5.6.2 can be maintained by using Kalman filter output and state feedback gain. The state space model obtained in equation (2.26) for the blade element is considered as LQG control design model as follows.

$$\begin{aligned} \dot{x}_r(t) &= A_r x_r(t) + B_r u(t) + \Gamma w_s(t) \\ y_r(t) &= C_r x_r(t) + v_o(t) \end{aligned} \tag{5.14}$$

where $w_s(t)$ is the system noise and $v_o(t)$ is the observation noise. These are zero mean, white, uncorrelated Gaussian random signals. The LQG control problem aims to minimize the cost function

$$J = \lim_{t_f \to \infty} \frac{1}{t_f} E\left[\int_0^{t_f} \left[x_r^T(t) Q x_r(t) + u^T(t) R u(t) \right] dt \right] \tag{5.15}$$

where $E\{.\}$ is the statistical expectation operator. Also, Q and R are the weighting matrices applied to the states and control inputs, respectively. The full state feedback gain K_a obtained using an optimal control approach is computed as

$$K_a = -R^{-1} B_r^T P \tag{5.16}$$

where P is the matrix which is obtained in the solution of the Algebraic Riccati Equation (ARE). The state estimate $\hat{x}$ is formed using the Kalman filter state estimator as follows

$$\dot{\hat{x}}_r(t) = A_r\hat{x}_r(t) + B_r u(t) + K_e(y_r(t) - C_r\hat{x}_r(t)) \tag{5.17}$$

where K_e is the Kalman filter gain and computed as

$$K_e = SC_r{}^T V^{-1} \tag{5.18}$$

Here S is the solution of the following ARE

$$A_r S + SA_r{}^T - SC_r{}^T V^{-1} C_r S + \Gamma W \Gamma^T = 0 \tag{5.19}$$

where V and W are the spectrum of the system and observation noises.

5.6.4. State Feedback Based Positive Current Algorithm

The optimal control input is constituted using the state feedback gain matrix K_a and the estimated state vector $\hat{x}$ of the Kalman filter.

$$u = i_c = -K_a\hat{x} \tag{5.20}$$

Assume that the estimated state vector is separated as

$$\hat{x} = \begin{bmatrix} x_{a1} \\ \dot{x}_{a1} \end{bmatrix}, \quad x_{a1} = \begin{bmatrix} w_1 \\ \vdots \\ w_{nd} \end{bmatrix}, \quad \dot{x}_{a1} = \begin{bmatrix} \dot{w}_1 \\ \vdots \\ \dot{w}_{nv} \end{bmatrix} \tag{5.21}$$

where x_{a1} and $\dot{x}_{a1}$ are the estimated displacement and velocity vectors, respectively. The state feedback matrix is also separated as

$$K_a = [k_{a1} \quad k_{a2}], \quad k_{a1} = [k_{1d} \quad \dots \quad k_{md}], \quad k_{a2} = [k_{1v} \quad \dots \quad k_{mv}] \tag{5.22}$$

where k_{a1} and k_{a2} are the feedback vectors for the displacements and velocities respectively. The control current is computed based on the separated feedback gain vectors and the estimated states as follows.

$$\begin{aligned} i_c &= -k_{a1}x_{a1} - k_{a2}\dot{x}_{a1} \\ &= -k_{1d}w_1 - k_{2d}w_2, \dots - k_{md}w_{nd} - k_{1v}\dot{w}_1 - k_{2v}\dot{w}_2, \dots - k_{mv}\dot{w}_{nv} \end{aligned} \tag{5.23}$$

The positiveness of the control current is maintained by considering each part of the control input. In each case, the positive current is determined by the sign check of the feedback gain and state multiplications. If the products of displacement and velocity vectors with the feedback gains are positive, then the control current is taken zero due to negative sign in equation (21). Case I shows this situation as follow

Case I:

$$\begin{aligned} &if \quad k_{a1}x_{a1} \geq 0 \quad \text{and} \quad k_{a2}\dot{x}_{a1} \geq 0 \\ &\text{then} \quad i_c = -k_{a1}x_{a1} - k_{a2}\dot{x}_{a1} \leq 0 \quad \begin{cases} i = i_c = 0 \\ f = f_c = 0 \end{cases} \end{aligned} \tag{5.24}$$

When the multiplication of feedback gain and the velocity vector is negative while the other multiplication is still positive as shown in Case II

Case II:

$$\begin{aligned} &if \quad k_{a1}x_{a1} > 0, \quad \text{and} \quad k_{a2}\dot{x}_{a1} < 0 \\ &\text{then} \quad i_c = -k_{a1}x_{a1} - (-k_{a2}\dot{x}_{a1}) = -k_{a1}x_{a1} + k_{a2}\dot{x}_{a1} \end{aligned} \tag{5.25}$$

then the current computation of Case II results two possible conditions such as

$$\begin{aligned} &1. \quad if \quad |k_{a1}x_{a1}| > |k_{a2}\dot{x}_{a1}| \quad \text{then} \quad i_c < 0 \quad \begin{cases} i = i_c = 0 \\ f = f_c = 0 \end{cases} \\ &2. \quad if \quad |k_{a1}x_{a1}| < |k_{a2}\dot{x}_{a1}| \quad \text{then} \quad i_c > 0 \quad \begin{cases} i = i_c \\ f = f_c \end{cases} \end{aligned} \tag{5.26}$$

The comparisons of the other possibilities are checked in Case III and Case IV as follows

Case III:

$$\begin{aligned} &\textit{if} \quad k_{a1}x_{a1} \le 0 \quad \text{and} \quad k_{a2}\dot{x}_{a1} \le 0 \\ &\text{then} \quad i_c = k_{a1}x_{a1} + k_{a2}\dot{x}_{a1} > 0 \quad \begin{cases} i = i_c \\ f = f_c \end{cases} \end{aligned} \tag{5.27}$$

Case IV:

$$\begin{aligned} &\textit{if} \quad k_{a1}x_{a1} < 0, \quad \text{and} \quad k_{a2}\dot{x}_{a1} > 0 \\ &\text{then} \quad i_c = -(-k_{a1}x_{a1}) - k_{a2}\dot{x}_{a1} = k_{a1}x_{a1} - k_{a2}\dot{x}_{a1} \end{aligned} \tag{5.28}$$

Similar to Case II, the positiveness of the current depends on the value of each part

$$\begin{aligned} &1. \quad \textit{if} \quad |k_{a1}x_{a1}| > |k_{a2}\dot{x}_{a1}| \quad \text{then} \quad i_c > 0 \quad \begin{cases} i = i_c \\ f = f_c \end{cases} \\ &2. \quad \textit{if} \quad |k_{a1}x_{a1}| < |k_{a2}\dot{x}_{a1}| \quad \text{then} \quad i_c < 0 \quad \begin{cases} i = i_c = 0 \\ f = f_c = 0 \end{cases} \end{aligned} \tag{5.29}$$

The structure of the control system is depicted in Figure 5.30. Note that the algorithm block in Figure 5.30 realizes all cases given in equations (5.24) -(5.29).

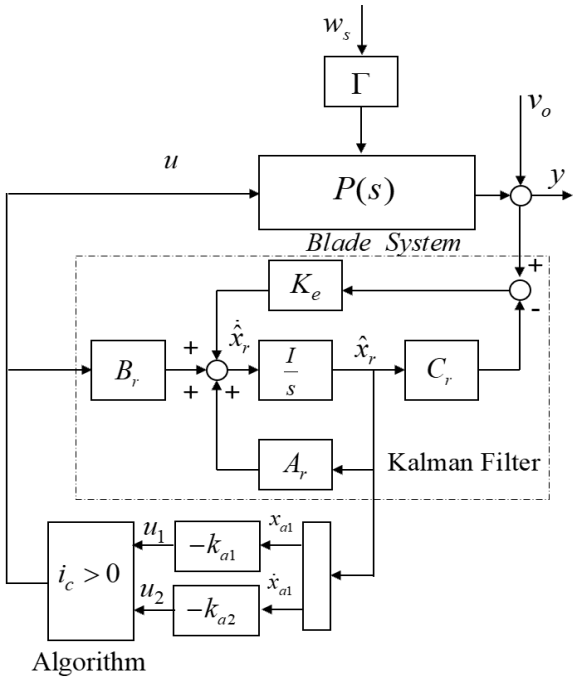

Figure 5.30: State feedback control structure with positive current algorithm.

5.6.5. Experimental Study

The blade element filled with MR fluid explained in Section 2 is studied for vibration suppression experiments. The switching LQG control is implemented using the Simulink block as depicted in Figure 5.31.

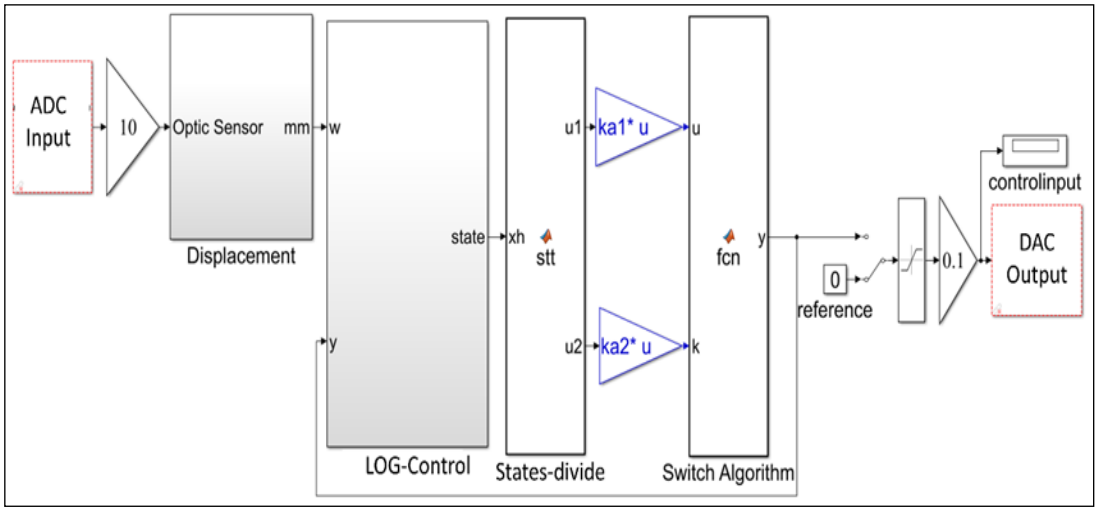

Figure 5.31: Experimental Simulink block.

5.6.6. Results and Discussion

The effectiveness of the proposed switching control is evaluated in frequency responses of the blade element. The experimental frequency response of the blade obtained with and without the controller is shown in Figure 5.32(a) for up to 1 kHz. The controlled first two modes of the blade structure are depicted in Figure 5.32(b). The switching LQG controller provided a significant gain reduction in the first vibration mode of the blade element. The second vibration mode is also reduced at an acceptable level. The amount of reduction in the closed loop frequency response gains are 18.53 dB in the first mode and 9.36 dB in the second mode.

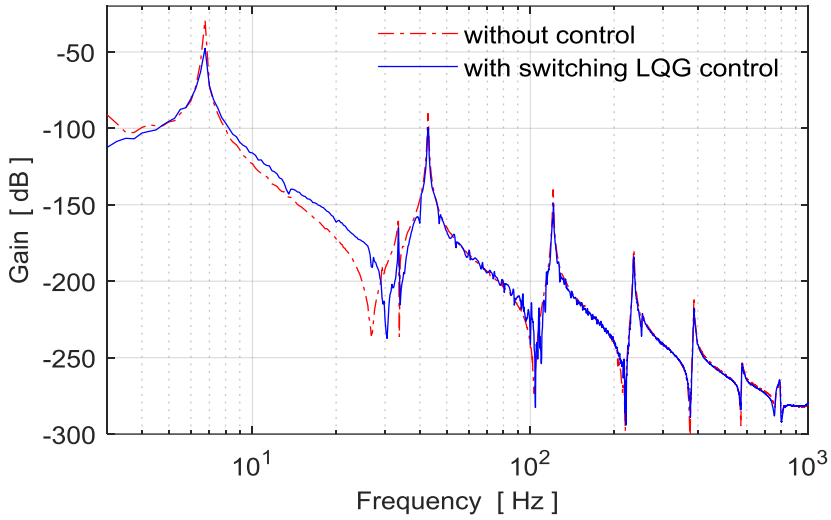

a)

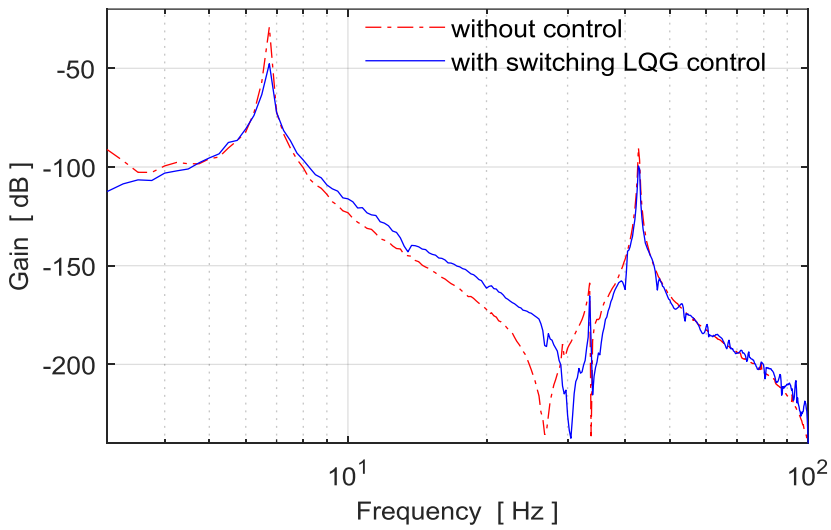

b)

Figure 5.32: Frequency responses of the control system, a) all vibration modes, b) first two modes.

The switching LQG controller performance is examined under a steady-state aerodynamic disturbance for different air speeds of the nozzle. The experimental results are evaluated for two different air loads. The closed-loop system time history responses with the switching LQG control in the case of 10 m/s air speed are obtained for a continuous controlled case as shown in Figure 5.33(a). In addition, the repeated controlled experiments are performed to understand the response characteristics of the controller as given in Figure 5.33(b). These results are compared uncontrolled case to exhibit the vibration attenuation level. The proposed switching controller reduced the steady-state disturbance drastically. The control inputs generated using positive current algorithm and applied in experiments are shown in Figure 5.34(a)-(b). It is clear that the defined algorithm produces positive control currents in all control cases. To see the variation of the displacement with controlled and uncontrolled cases and control input a more detailed time response of the blade obtained at 10 m/s air speed is illustrated in Figure 5.35 in the small-scale time range.

The air speed of the nozzle increased to 15 m/s and applied to the blade structure to test the limits of the control performance. The closed-loop control system results obtained in experiments with 15 m/s air speed are illustrated in Figure 5.36(a)-(b). As is seen, the switching controller succeeded to suppress the vibration of the blade significantly. Moreover, Figure 5.37(a)-(b) show the positive control current characteristics for the continuous and repeated controlled cases, respectively. A worst-case test is also implemented by mounting an extra mass on the surface of the blade. Figure 5.38 shows the experimental results when a tip mass which is 6% of the blade mass is added. The switching controller gave reasonable results against parameter uncertainty and attenuated the blade vibrations with the tip mass.

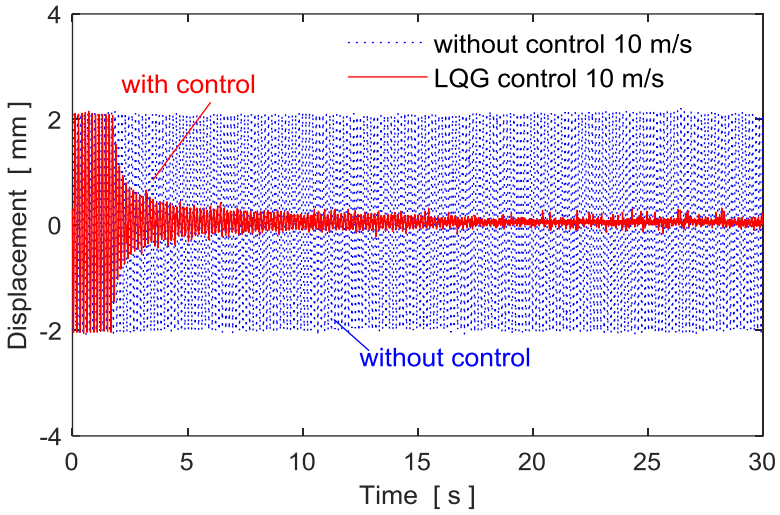

a)

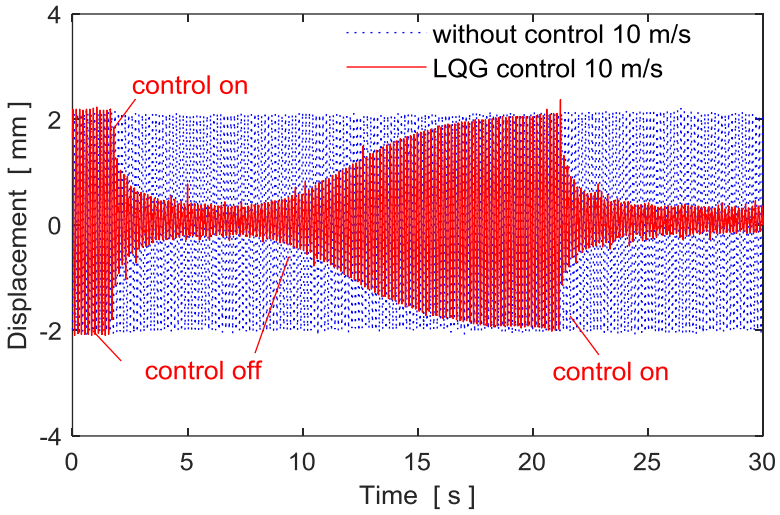

b)

Figure 5.33: Experimental time history responses under the steady state aerodynamic disturbance for 10 m/s air speed, a) continuous controlled, b) repeated controlled.

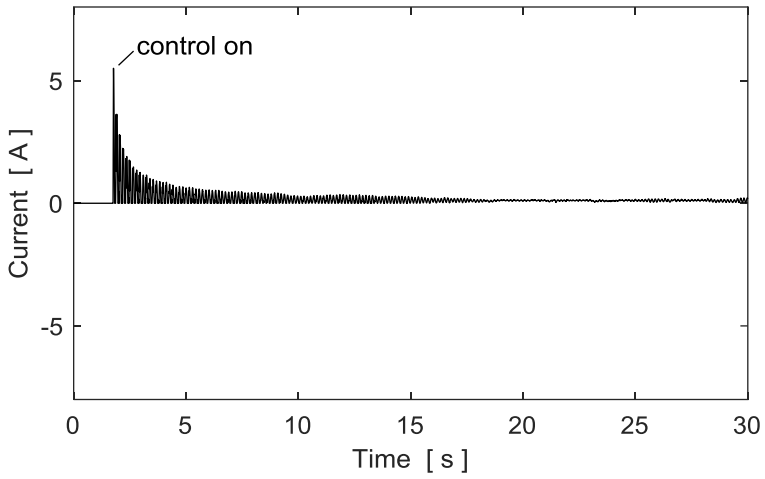

a)

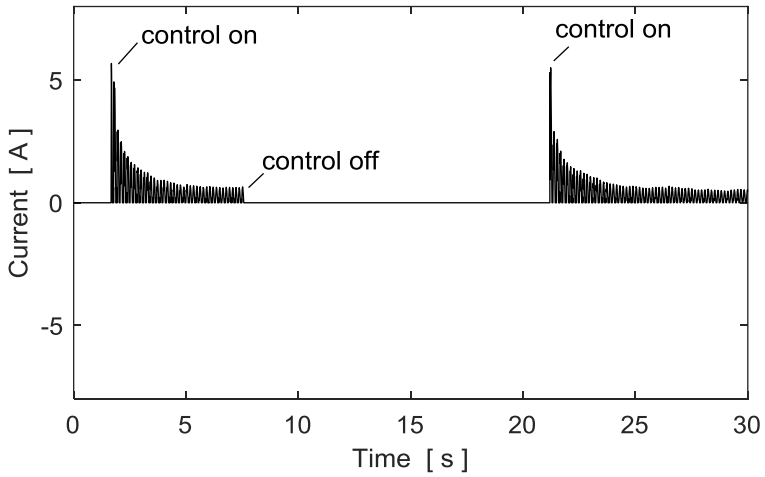

b)

Figure 5.34: Experimental control inputs for 10 m/s, a) continuous controlled, b) repeated controlled.

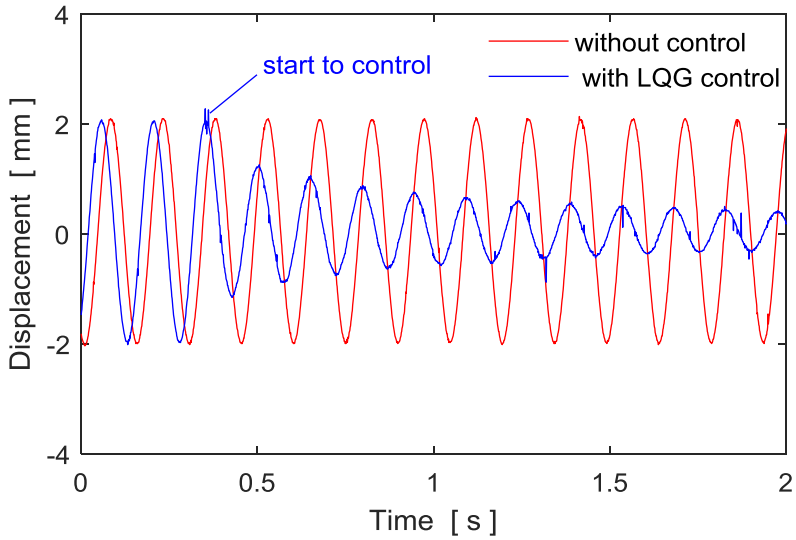

a)

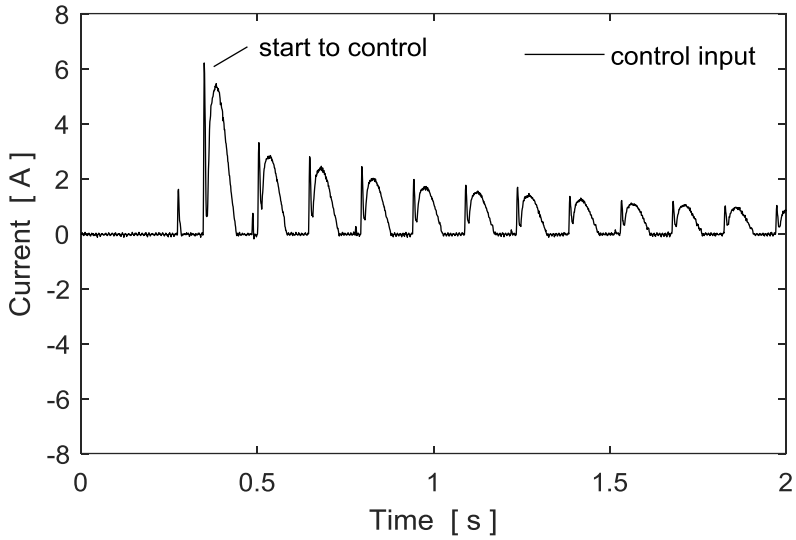

b)

Figure 5.35: Variation in detailed time responses, a) the blade displacement, b) the control input.

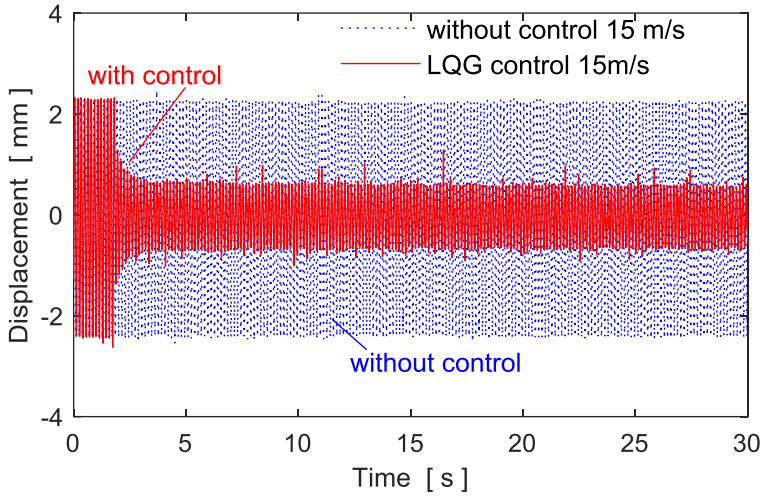

a)

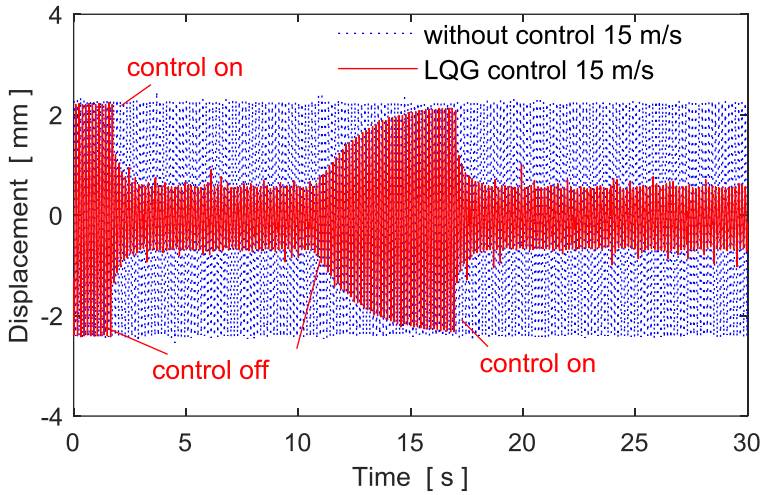

b)

Figure 5.36: Experimental time history responses under the steady state aerodynamic disturbance for 15 m/s, a) continuous controlled, b) repeated controlled.

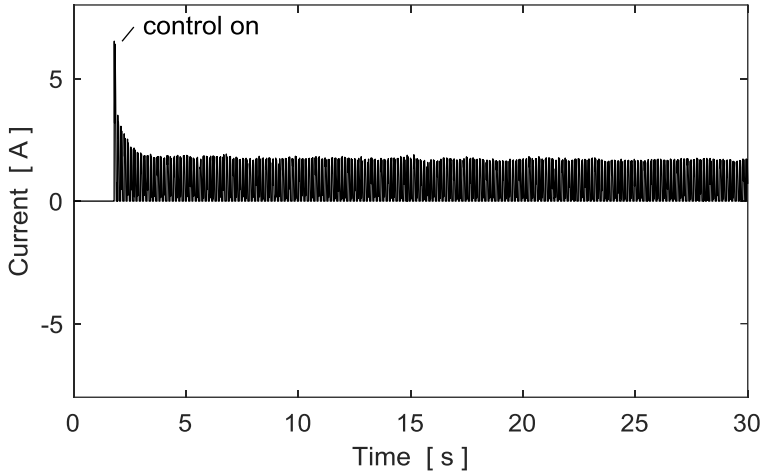

a)

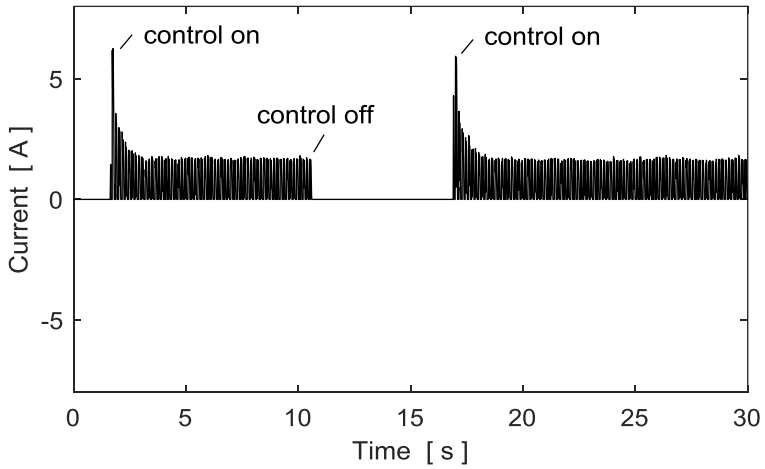

b)

Figure 5.37: Experimental control inputs for 15 m/s, a) continuous control, b) repeated control

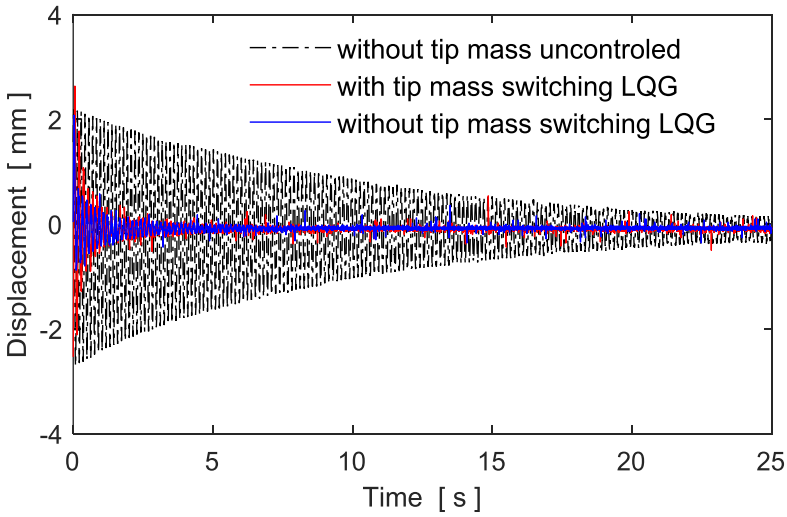

Figure 5.38: Worst-case test results for a tip mass.

6. CONCLUSIONS

In this thesis study, active vibration control of a small-scale wind turbine blade element was presented using different applications of the MR fluid material under the effect of a steady state aerodynamic disturbance. The thesis has the following conclusions:

- A new MR fluid patch was proposed for active vibration control applications of flexible systems. The actuation of the MR patch is realized with an electromagnet.
- The empty blade element was filled with the MR fluid and actuated with an electromagnet. The proposed MR filled blade structure have differences compared to MR sandwich beams. In sandwich structures, the MR layer is formed in a different way and a homogeneous magnetic field is applied to each point. Therefore, it is aimed to increase the rigidity of these sandwich structures. The blade element containing MR fluid is only affected by the fluid mass inside the structure.
- The blade element was modeled using two different approaches. A natural frequency analysis of the blade was performed and compared with the experimental analysis.
- A force-based interaction model between MR fluid and the electromagnet was derived for both situations and some characterization works were presented. It is seen that the characteristics of the force is nonlinear with respect to the displacement and current.
- A multi-objective H_2/H_∞ controller was designed to attenuate the vibration of the blade structure. Three design structures were studied for disturbance rejection, performance improvements and robustness in the control system.
- Some experiments were implemented to show the effectiveness of the proposed MR patch and MR fluid containing blade under steady state aerodynamic disturbance. The experimental frequency and the time history responses of the closed loop system showed the significant vibration reduction in the flexible blade structure. The targeted vibration modes were

suppressed by the proposed controllers in different levels and the results matched with the design objectives.

- A PZT patch-based control was implemented for the same blade element to understand effectiveness of the proposed MR patch actuation. The experimental results showed that MR fluid patch performances was comparable with PZT patch actuator results.
- A switching LQG control structure was proposed and an algorithm for positive control current of the electromagnetic actuator was developed. The proposed algorithm was experimentally verified for the active vibration control of the blade element.
- The application of the proposed MR fluid blade-electromagnetic actuator may be possible for the small and medium size wind turbine blades. The electromagnets should move with the blades during wind turbine operation by using slip rings to conduct power to the electromagnets.

REFERENCES

Bishay P. L., Tawfik M., Negm H. M., (2010), “Experimental and finite element models of an adaptive magnetorheological sandwich beam”, In Proceedings of the 17th International Congress on Sound & Vibration, Cairo, Egypt, 18-22 July 2010

Chen L., Hansen C.H., (2005), “Active vibration control of a magnetorheological sandwich beam”, In Proceedings of the Australian Acoustical Society Conference, Busselton, 93–98, Western Australia, 9–11 November.

Choi S.B., Park Y.K., Jung S.B., (1999), “Modal characteristics of a flexible smart plate filled with electrorheological fluids”, Journal of Aircraft, 36, 458–464.

Cortés F., Sarría I., (2015), “Dynamic analysis of three-layer sandwich beams with thick viscoelastic damping core for finite element applications”, Shock and Vibration. 2015.

Eshaghi M., Rakheja S., Sedaghati, R. (2015), “An accurate technique for pre-yield characterization of MR fluid”, Smart Materials and Structures, 24(6), 065018.

Fonseca H. A., Gonzalez E., Restrepo J., Parra C. A., Ortiz C., (2016, February), “Magnetic effect in viscosity of magnetorheological fluids”, In Journal of Physics: Conference Series (Vol. 687, No. 1, p. 012102). IOP Publishing.

Griffin D., Malkin M., (2011), “Lessons learned from recent blade failures: primary causes and risk-reducing technologies”, In 49th AIAA Aerospace Sciences Meeting Including the New Horizons Forum and Aerospace Exposition (p. 259).

Ghorbanpour Arani A., BabaAkbar Zarei H., Eskandari M., and Pourmousa P., (2017), “Vibration behavior of visco-elastically coupled sandwich beams with magnetorheological core and three-phase carbon nanotubes/fiber/polymer composite facesheets subjected to external magnetic field”, Journal of Sandwich Structure and Material 1099636217743177.

Hagedorn P., DasGupta A., (2007), “Vibrations and waves in continuous mechanical systems”, ISBN: 978-0-470-51738-3, John Wiley & Sons.

Hirunyapruk C., (2009), “Vibration Control Using an Adaptive Tuned Magneto-Rheological Fluid Vibration Absorber”, Doctoral Thesis, University of Southampton.

Hu B., Wang D., Xia P., Shi Q., (2006), “Investigation on the vibration characteristics of a sandwich beam with smart composites-MRF”, World Journal of Modelling and Simulation, 2(3), 201-206.

Irazu L., Elejabarrieta M. J., (2017), “Magneto-dynamic analysis of sandwiches composed of a thin viscoelastic-magnetorheological layer”, Journal of Intelligent Material Systems and Structures, 1045389X17705209.

Kolekar S., Venkatesh K., Oh J. S., Choi S. B., (2017), “The tenability of vibration parameters of a sandwich beam featuring controllable core: Experimental Investigation”, Advances in Acoustics and Vibration.

Korobko E. V., Mikhasev G. I., Novikova Z. A., Zhurauski M. A., (2012), “On damping vibrations of three-layered beam containing magnetorheological elastomer”, Journal of Intelligent Material Systems and Structures, 23(9), 1019-1023.

Le S., (2009), “Active vibration control of a flexible beam. San Jose State University”, 2009, 89 p.

Madoyan A., (2009), “Design and Comparison of Mixed H_2 / H_∞ controller for AMB System”, Master Thesis, Lappeenranta University of Technology, Finland.

Manoharan R., Vasudevan R., Sudhagar P. E., (2016), “Semi-active vibration control of laminated composite sandwich plate–an experimental study”, Archive of Mechanical Engineering, 63(3), 367-377.

Martin L. A., (2011), “A novel material modulus function for modeling viscoelastic materials (Doctoral dissertation, Virginia Tech). Ph.D. Thesis”, Virginia Polytechnic Institute and State University, Blacksburg, VA, USA, 2011. Micromachines 2018, 9, 80 15 of 15

Niu H., Zhang Y., Zhang X., Xie S., (2010), “Active vibration control of plates using electro-magnetic constrained layer damping”, International Journal of Applied Electromagnetics and Mechanics, 33(1, 2), 831-837.

Qian L. J., Xin F. L., Bai X. X., Wereley N. M., (2017), “State observation–based control algorithm for dynamic vibration absorbing systems featuring magnetorheological elastomers: Principle and analysis”, Journal of Intelligent Material Systems and Structures, *28*(18), 2539-2556.

Rajamohan V., Sedaghati R., Rakheja S., (2011), “Optimal vibration control of beams with total and partial MR-fluid treatments”, Smart materials and structures, 20(11), 115016.

Rajamohan V., Rakheja S., Sedaghati R., (2010), “Vibration analysis of a partially treated multi-layer beam with magnetorheological fluid”, Journal of Sound and Vibration, 329(17), 3451-3469.

Rajamohan V., Sundararaman V., Govindarajan B., (2013), “Finite element vibration analysis of a magnetorheological fluid sandwich beam”, Procedia Engineering, 64, 603-612.

Ramamoorthy M., Rajamohan V., AK J., (2016), “Vibration analysis of a partially treated laminated composite magnetorheological fluid sandwich plate”, Journal of Vibration and Control, 22(3), 869-895.

Romaszko M., (2013, May), “Free vibration control of a cantilever MR fluid-based sandwich beam”, In Carpathian Control Conference (ICCC), 2013 14th International (pp. 311-314). IEEE.

Selig M. S., and McGranahan B. D., (2004), “Wind tunnel aerodynamic tests of six airfoils for use on small wind turbines”, Journal of Solar Energy Engineering (Transactions of the ASME), 126(4): 986-1001.

Sivrioglu S., Nonami K., (1997), “Active Vibration Control by Means of LMI-Based Mixed $H_2/H\infty$ State Feedback Control”, JSME International Journal Series C 40(2): 239-244.

Somers D. M., Maughmer M. D., (2003), “Theoretical Aerodynamic Analyses of Six Airfoils for Use on Small Wind Turbines”, National Renewable Energy Laboratory (NREL): (No. NREL/SR-500-33295).

Steven De Lannoy (2013), “Section Modulus and Bending Inertia of Wings”, Available at: http://www.wingbike.nl/Wingbike_Hydrofoil/Background.html.

Sun Q., Zhou J. X., Zhang L., (2003), “An adaptive beam model and dynamic characteristics of magnetorheological materials”, Journal of Sound and Vibration, 261(3), 465-481.

Sun L., Li W., Wu Y., Lan, Q. (2017), “Active vibration control of a conical shell using piezoelectric ceramics”, Journal of Low Frequency Noise, Vibration and Active Control, 36(4), 366-375.

Stanway R., Sproston J. L., El Wahed A. K., (1996), “Applications of electrorheological fluids in vibration control: a survey”, Smart Materials and Structures 5, p. 464-482

Sugiyama S., Sakurai T., & Morishita S., (2013), “Vibration control of a structure using Magneto-Rheological grease damper”, Frontiers of Mechanical Engineering, 8(3), 261-267.

Svendsen M. N., Krenk S., Høgsberg J. B., (2011), “Wind turbine rotors with active vibration control”, Ph. D. thesis; DTU 2011.

Tůma J., Šuránek P., Mahdal M., Wagnerová R., (2016, July), “Linear piezoactuators in systems of the active vibration control”, In Proceedings of the 23rd International Congress on Sound and Vibration (ICSV 23) (pp. 10-14). Athens Greece.

Valevate A.V., (2004), “Semi-Active Vibration Control of a Beam Using Embedded Magneto-Rheological Fluids”, Ph.D. Thesis, Wright State University, Dayton, OH, USA, 2004.

Weiss K. D., Carlson J. D., Nixon, D. A., (1994), “Viscoelastic properties of magneto-and electro-rheological fluids”, Journal of Intelligent Material Systems and Structures 5, p. 772-775.

Wu D., Huang L., Pan B., Wang Y., Wu S., (2014), “Experimental study and numerical simulation of active vibration control of a highly flexible beam using piezoelectric intelligent material”, Aerospace Science and Technology, 37, 10-19.

Xu Y. L., Qu W. L., Ko J. M., (2000), “Seismic response control of frame structures using magnetorheological/electrorheological dampers”, Earthquake Engineering and Structural Dynamics 29, p. 557-575.

Yang G., (2001), “Large-Scale Magnetorheological Fluid Damper for Vibration Mitigation: Modeling, Testing and Control”, Ph.D. Thesis, University of Notre Dame, Notre Dame, IN, USA, 2001.

Yalcintas M., Dai H., (1999), “Magnetorheological and electrorheological materials in adaptive structures and their performance comparison”, Smart Materials and Structures, 8(5), 560.

Yalcintas M., Dai H., (2003), “Vibration suppression capabilities of magnetorheological materials based adaptive structures”, Smart Materials and Structures, 13(1), 1.

Yeh J. Y., (2013), “Vibration analysis of sandwich rectangular plates with magnetorheological elastomer damping treatment”, Smart Materials and Structures, 22(3), 035010.

Zhang K., Scorletti G., Ichchou M., Mieyeville, F., (2015), “Quantitative robust linear parameter varying H∞ vibration control of flexible structures for saving the control energy”, Journal of Intelligent Material Systems and Structures, 26(8), 1006-1027.

Zhou K., Doyle J. C., (1998), “Essentials of robust control (Vol. 104)”, Upper Saddle River, NJ: ISBN-13: 978-0135258330, Prentice hall.

BIOGRAPHY

Fevzi Çakmak BOLAT was born in 1987 in Tokat/Turhal. He received the B.S degree mechanical engineering from the Atatürk University, Erzurum, Turkey in 2009. He worked as a mechanical engineer in Kamer Construction Company for one year between 2009-2010. He graduated from Ataturk University, Institute of Science, Department of Machine Dynamics and Theory, Erzurum, Turkey, in 2011. He started doctoral studies Gebze Technical University Graduate School of Natural and Applied Science Department of Mechanical Engineering in 2012. He has been working as a research assistant in Gebze Technical University since 2012. He is married and has one child.

APPENDICES

Appendix A: Articles Published During the Thesis Study

Bolat F. C., & Sivrioglu S., (2018), “Active Vibration Suppression of Elastic Blade Structure Using a Novel MR Layer Patch”, Journal of Intelligent Material Systems and Strustures.doi: 10.1177/1045389X18799441

Bolat F. C., & Sivrioglu S., (2018), “Active Control of a Small-Scale Wind Turbine Blade Containing Magnetorheological Fluid”, Micromachines, 9(2), 80.

Bolat F. Ç., & Sivrioğlu, S., (2018), “Active Vibration Suppression of a Flexible Blade Element Using Magnetorheological Layer Patch-Electromagnetic Actuator”, Turkish Journal of Electromechanics and Energy, 3(1).

Bolat F. C., & Sivrioğlu S., (2017), “H2, Hinfinity and H2/Hinfinity Control of Elastic Beam Vibrations Using Piezoelectric Actuator”, International Journal of Applied Mathematics, Electronics and Computers, 5(3), 53-61.

Sivrioglu S., & Bolat, F. C., (2018, March), “Active Robust Control of Elastic Blade Element Containing Magnetorheological Fluid”, In IOP Conference Series: Materials Science and Engineering (Vol. 326, No. 1, p. 012017). IOP Publishing.

Bolat F.C., and Sivrioglu S., (2017), “Multi-objective H2/H∞ Control of Blade Vibrations Using Piezoelectric Actuator”, International Conference on Advaced Techologies (ICAT’17). Istanbul**.**